◑ Geothermal Energy

Check for updates

Stress sensitivity of porosity and permeability under varying hydrostatic stress conditions for different carbonate rock types of the geothermal Malm reservoir in Southern Germany

Daniel Bohnsack[1], Martin Potten[2], Simon Freitag[3], Florian Einsiedl[1] and Kai Zosseder[1*] ⬤

*Correspondence:
kai.zosseder@tum.de
[1] Chair of Hydrogeology,
Technical University
of Munich, Arcisstr. 21,
80333 Munich, Germany
Full list of author information
is available at the end of the
article

Abstract

In geothermal reservoir systems, changes in pore pressure due to production (depletion), injection or temperature changes result in a displacement of the effective stresses acting on the rock matrix of the aquifer. To compensate for these intrinsic stress changes, the rock matrix is subjected to poroelastic deformation through changes in rock and pore volume. This in turn may induce changes in the effective pore network and thus in the hydraulic properties of the aquifer. Therefore, for the conception of precise reservoir models and for long-term simulations, stress sensitivity of porosity and permeability is required for parametrization. Stress sensitivity was measured in hydrostatic compression tests on 14 samples of rock cores stemming from two boreholes of the Upper Jurassic Malm aquifer of the Bavarian Molasse Basin. To account for the heterogeneity of this carbonate sequence, typical rock and facies types representing the productive zones within the thermal reservoir were used. Prior to hydrostatic investigations, the hydraulic (effective porosity, permeability) and geomechanical (rock strength, dynamic, and static moduli) parameters as well as the microstructure (pore and pore throat size) of each rock sample were studied for thorough sample characterization. Subsequently, the samples were tested in a triaxial test setup with effective stresses of up to 28 MPa (hydrostatic) to simulate in-situ stress conditions for depths up to 2000 m. It was shown that stress sensitivity of the porosity was comparably low, resulting in a relative reduction of 0.7–2.1% at maximum effective stress. In contrast, relative permeability losses were observed in the range of 17.3–56.7% compared to the initial permeability at low effective stresses. Stress sensitivity coefficients for porosity and permeability were derived for characterization of each sample and the different rock types. For the stress sensitivity of porosity, a negative correlation with rock strength and a positive correlation with initial porosity was observed. The stress sensitivity of permeability is probably controlled by more complex processes than that of porosity, where the latter is mainly controlled by the compressibility of the pore space. It may depend more on the compaction of precedented flow paths and the geometry of pores and pore throats controlling the connectivity within the rock matrix. In

general, limestone samples showed a higher stress sensitivity than dolomitic limestone or dolostones, because dolomitization of the rock matrix may lead to an increasing stiffness of the rock. Furthermore, the stress sensitivity is related to the history of burial diagenesis, during which changes in the pore network (dissolution, precipitation, and replacement of minerals and cements) as well as compaction and microcrack formation may occur. This study, in addition to improving the quality of input parameters for hydraulic–mechanical modeling, shows that hydraulic properties in flow zones largely characterized by less stiff, porous limestones can deteriorate significantly with increasing effective stress.

Keywords: Stress sensitivity, Hydrostatic, Effective stress, Poroelastic, Porosity, Permeability, Malm, Geothermal energy, Molasse Basin, Carbonate

Introduction

In recent years, geothermal energy has become increasingly important as a renewable energy source for the generation of thermal and electrical energy in Southern Germany (Bavaria). The Upper Jurassic Malm aquifer is the main target formation for geothermal (hydrothermal) exploration here, as its temperature (low enthalpy) and hydraulic conditions offer a promising environment for a productive reservoir (Steiner et al. 2014; Schellschmidt et al. 2010). The economic viability of a geothermal project in general rests on two main pillars—an adequate permeability leading to good hydraulic productivity of the reservoir and fluid temperature appropriate to the distinct business case (Weber and Moeck 2017; Agemar et al. 2014; Farquharson et al. 2016). In the Bavarian Molasse Basin, the depth of the Malm aquifer increases towards the south, which is usually associated with increasing fluid temperatures in the reservoir and thus increases the efficiency for geothermal applications (Lüschen et al. 2014; Fritzer 2012). In contrast, the evaluation of pumping tests of various geothermal projects proves a progressive deterioration of hydraulic aquifer properties with increasing depth south of Munich (Konrad et al. 2019). Formation pressure is generally sub-hydrostatic to hydrostatic throughout the entire basin due to drainage into the Danube river at the northern border of the Bavarian Molasse Basin, where the Upper Jurassic carbonate succession emerges above surface (Drews et al. 2018; Lemcke 1976). These pressure conditions indicate well-permeable connectivity within the karst and fracture-dominated reservoir (Lemcke 1976). However, Drews et al. (2020) described an onset of overpressured reservoir conditions south of Munich, indicating a decrease in hydraulic connectivity of the pore network, resulting in low productivity rates of geothermal wells. The decreasing hydraulic productivity towards the south is also reflected in the hydrochemical composition of the reservoir fluid. Heine et al. (2021) found a hydrochemical compartmentalization of the reservoir fluid within the central part of the Molasse Basin and observed increasing fluid–rock interaction between the host rock and groundwater towards the south of Munich, which may indicate a decrease in hydraulic permeability. With increasing vertical depth, internal stresses and diagenetic effects have an increasingly negative impact on hydraulic properties such as the effective porosity and permeability of the rock matrix and thus on the productivity of the geothermal well (Ehrenberg and Nadeau 2005; Ehrenberg et al. 2009).

In combination with fractures and karstified zones, the hydraulic properties of the rock matrix are the controlling factors for the storage and flow of fluids within the Malm

reservoir. Therefore, the distribution, variety, and stress sensitivity of these parameters are required as important input parameters for thermal–hydraulic–mechanical modelling (THM) (Brehme et al. 2016; Cacace and Jacquey 2017; Konrad et al. 2019). However, the high variability of the depositional environment during the Upper Jurassic has resulted in a very heterogeneous distribution within the entire carbonate succession (Koch and Munnecke 2016; Mraz 2018; Niebuhr 2014; Homuth et al. 2014; Böhm 2012). The Upper Jurassic strata comprise alternating sequences of limestones, marls, and dolostones deposited on a shallow marine carbonate platform with locally occurring reefal buildups (Meyer and Schmidt-Kaler 1996; Meyer and Schmidt-Kaler 1990a, b; Koch 1997; Böhm et al. 2013). Consequently, the petrophysical, geomechanical, and hydraulic properties of the aquifer rock also show high local variation (Homuth et al. 2015; Bohnsack et al. 2020, 2019; Homuth 2014; Rioseco et al. 2018; Przybycin et al. 2017). To cope with this heterogeneity, a detailed database for the distribution of parameters for the different rock and facies types is essential. Since most rock properties are studied under laboratory conditions (samples of drill cores and outcrop analogues), knowledge of the rock-type specific relationship between stress and porosity/permeability is crucial for parameterizing models to transfer the data to the in-situ stress conditions of a reservoir. In this study, the influence of variable effective stresses was investigated for ranges up to 28 MPa, which corresponds to a maximum vertical drilling depth of about 2000 m. The simulated drilling depth may be taken as representative for most sites within the Bavarian Molasse Basin (depending on the prevailing pore pressure), and the findings of this study on stress sensitivity can help to better understand fundamental processes affecting the hydraulic properties of the rock matrix at varying stress conditions.

State of the art

The theory of poroelasticity prescribes a deformation and change in shape and volume of a porous solid to relieve the additional applied pressure (drained conditions) or a counteraction of pore pressure (undrained conditions) (Cheng 2016). Theoretically, stress changes within a reservoir can originate from the shift of one of the principle stresses by gravitational loading (vertical), plate tectonic driving forces (horizontal) or pore pressure changes. Under the simplified assumption that the vertical and horizontal stresses are in a local equilibrium, changes in pore pressure are the driving force for disturbances of a balanced stress field. The main reasons for pore pressure changes in a geothermal reservoir are changes in fluid temperature (e.g., reinjection of cold water) (Cacace et al. 2013), pressure increase at the injection well (Hofmann et al. 2014), and pressure drop due to drawdown or depletion of the reservoir (Coelho et al. 2006). While the principal stresses remain constant, the increase/decrease in pore pressure results in a change in the effective stress in the affected regions of the reservoir. A variation of the effective stress field in turn leads to stress-induced changes in the geometry of pores and pore throats, which influence the interconnectivity within the effective pore network and thus the permeability (Hassanzadegan and Zimmermann 2014; Gobran et al. 1987).

 The deformability of a porous solid and the stress sensitivity of the effective porosity (connected pore volume) and permeability have been the subject of numerous studies by several authors in the past. The importance of the stress sensitivity of permeability for the productivity of a reservoir was studied by Fatt and Davis (1952). The authors

investigated the permeability of sandstone samples in a pressure vessel and reported a permeability reduction exceeding 50% with increasing overburden pressure up to 100 MPa. Gobran et al. (1987) described a reduction in absolute permeability of up to 60% for unconsolidated Ottawa sand and samples of Berea sandstone with increasing fluid temperature and effective stress, measured in a triaxial permeability apparatus. Yale (1984) examined the stress dependency of fluid permeability, electrical conductivity, and porosity of several sandstone types in an experimental apparatus. The results showed a distinct decrease in porosity and permeability with increasing overburden pressure and related the underlying processes to the three dimensional interconnection of pores and pore throats within the pore network. Several other authors investigated the importance of pore geometry and connectivity of the pore network in relation to geomechanical behavior or the stress sensitivity for different rock types (Zoback and Byerlee 1975; Bernabe et al. 1982; Bernabe 1986; David et al. 1994; David et al. 2001; Chang et al. 2006; Dong et al. 2010; Pei et al. 2014; Cant et al. 2018; Kushnir et al. 2018; Xu et al. 2018; Wang et al. 2018; Heap et al. 2019a, b; Kennedy et al. 2020; Meng et al. 2020; Kluge et al. 2021). Ghabezloo et al. (2009a) stated that the compaction-induced reduction in permeability and porosity can be determined by a simplified effective stress law as an exponential model based on material-specific constants (sensitivity coefficients) (Cheng 2016; Meng et al. 2019; Dong et al. 2010; David et al. 1994). However, Cheng (2016) stated that permeability represents the ability of a fluid to flow through a pore network and is consequently a function of porosity. He, therefore, suggests that stress-induced permeability depends mainly on changes in porosity (porosity sensitivity).

Recent research on the poroelastic behavior of sandstone in hydrostatic triaxial tests showed a reduction of porosity between 3 and 8% (relative) for effective pressures of up to 70 MPa (Blöcher et al. 2014; Hassanzadegan et al. 2014; Blöcher 2008). Hassanzadegan et al. (2014) and Hassanzadegan and Zimmermann (2014) described a non-linear deformation during hydrostatic compression in relation to the presence of cracks, which also influence the closure of the pathways for the fluid flow and thus permeability. At low effective pressure, the authors found a nonlinear decrease in permeability that becomes progressively linear when a confined state is achieved at high effective pressures. In addition, the study observed a dependence of porosity and permeability variation on the geometry of pores and cracks, in particular the aspect ratio (length to width) of a pore. Narrow cracks are more compliant than round pores and, according to Walsh's (1981) crack closure theory, can close even at low effective pressure.

This is only a brief summary of the available literature, which mainly focuses on the investigation of clastic sedimentary, volcanic, and magmatic rock types. There are considerably fewer studies for the investigation of carbonate rocks, which seem to have been of greater interest only in recent years. Fabre and Gustkiewicz (1997) investigated different limestones and sandstones from Poland and France to evaluate their poroelastic response to different hydrostatic pressure conditions. As a result, the authors found distinct relationships between poroelastic properties and initial porosity of mainly non-fissured rocks, which can be used to predict the geomechanical behavior of a reservoir for the variation of effective stresses by numerical modelling. Ghabezloo et al. (2009b) established an effective stress law in the form of a power law for a sparitic calcite cemented oolitic limestone and developed a microstructural pore-shell model for this type of

Bohnsack *et al. Geotherm Energy*   (2021) 9:15

Page 5 of 59

facies. In this work, constant-head permeability tests were performed in a triaxial cell with varying confining and pore pressure to evaluate the permeability change induced by effective stress changes. Selvadurai and Głowacki (2008) conducted permeability experiments on "Indiana limestone" samples under isotropic compression with partial loading, unloading, and reloading cycles. The authors reported strong hysteretic effects during unloading of the confining pressure and irreversible changes to the pore space in the form of pore reduction. According to the authors, the mechanisms of permeability reduction at different stresses are the reduction of voids, pore closure, pore throat collapse, and clogging of pores. Bakhtiari et al. (2011) and Moosavi et al. (2014) investigated different types of limestone and their dependence on effective stress in terms of pore volume compressibility. The study proposed a direct relationship between changes in pore compressibility (due to effective stress) and changes in porosity and permeability of reservoir rocks. The authors measured the pore compressibility at different confining pressures (effective stress up to 35 MPa) in an automated permeameter that also allows simultaneous measurement of porosity and permeability. In accordance with the results of Hassanzadegan and Zimmermann (2014) for sandstone, a nonlinear porosity–stress and permeability–stress relationship was reported with a stronger reduction during lower effective stress, which smoothened out with the transition to the higher effective stress regime. Depending on the type of limestone and its initial porosity, the increase in effective stress forced a permeability loss of less than 10% (vuggy limestone) to almost complete permeability loss for crystalline limestone and limestone with separated vugs. Baud et al. (2016) and Heap et al. (2018) investigated the influence of stylolites on the geomechanical and hydraulic properties of different limestone samples from the Jurassic of France. They studied samples with different types of stylolites and the influence of their orientation on rock strength and permeability of the rock sample when subjected to hydrostatic stress. As a basic result, Baud et al. (2016) concluded that the presence of sedimentary or tectonic stylolites, especially under saturated conditions, may cause a decrease in rock strength. In terms of permeability, Heap et al. (2018) noted that stylolites oriented perpendicular to the flow direction act as barriers to fluid flow and may be one of the reasons for the discrepancy between laboratory and reservoir data. The most recent research on the stress sensitivity of carbonate rocks was published by Meng et al. (2019). They performed high-pressure compression tests (hydrostatic and triaxial) on a set of undamaged and damaged limestone samples ("Indiana" and "Purbeck" limestones) and observed significant permeability reductions at critical stresses. One of the most important conclusions is that in carbonate formations within the studied porosity range (14–16%), the variations in porosity and permeability are quite small when only mechanical compaction is applied, since porosity cannot be significantly reduced by inelastic compaction alone.

Regarding the investigations of carbonate rocks from the Upper Jurassic Malm reservoir of the Molasse Basin, studies have been rather limited so far. The poroelastic (static) and dynamic moduli of outcrop analogues samples were investigated by Hassanzadegan et al. (2016) by the derivation of stress–strain curves in rock mechanical tests and measurement of acoustic velocities. The authors conducted drained and unjacketed poroelastic experiments at different temperatures and examined the strength of poroelastic coupling (product of Biot and Skempton coefficients), which helps to improve the link

between seismicity and geomechanics in reservoir characterization. Homuth and Sass (2014) as well as Pei et al. (2014) tested rock samples of outcrop analogues and rock cores in a thermo-triaxial cell at elevated pressures (up to 130 MPa) and temperatures (up to 150 °C) to simulate reservoir conditions. The study observed a decrease in permeability by 2–3 orders of magnitude due to thermal expansion, which significantly exceeds the permeability loss due to in-situ stress conditions (one order of magnitude). Pei et al. (2018) intensified the study of the thermal expansion of Upper Jurassic carbonate rocks by conducting experiments at different stress states with temperature cycles between 30 °C and 120 °C. The authors proposed different thermal expansion coefficients depending on distinct states of stresses and demonstrated temperature induced tensile cracks by microstructural analyses of the tested rock samples.

Objective of the study

Previous research has focused more on the theoretical and technical background of the pressure and temperature dependence itself. Experiments have mainly been carried out on a few selected samples as case studies, disregarding the influence of different lithology or facies of a heterogeneous carbonate sequence such as the Upper Jurassic Malm. This study, therefore, focuses particularly on the influence of varying rock parameters and different lithology and facies classes on the stress sensitivity of the elastic and hydraulic behavior of the reservoir rock, allowing to account for this heterogeneity and to provide valid input parameters for reservoir models that have to cope with changes in effective stresses.

To improve this understanding, in this study several samples of the Upper Jurassic carbonates from two cored boreholes (Dingolfing FB, Moosburg SC4) were investigated by various laboratory experiments. Core samples from the Upper Jurassic reservoir are very rare, but the selected samples cover the major rock and facies types occurring in these heterogeneous deposits. Before the evaluation of stress sensitivity in hydrostatic compression tests, the hydraulic (e.g., effective porosity) and mechanical properties (e.g., rock strength) as well as the microstructural composition (e.g., pore throat distribution) were investigated in detail. Subsequently, the rock samples were tested at different effective pressures to investigate stress-induced changes in deformation rate, porosity, and permeability. The aim of this study is, therefore, to link distinct rock types of the aquifer to stress sensitivity based on their lithology, pore type, and microstructure. The information obtained can then be used to provide reservoir models with parameters valid for in-situ reservoir conditions within the specific effective stress ranges.

Theoretical background and methods

Rock samples of rare drill cores from the Upper Jurassic reservoir were analyzed using several different laboratory methods for the study of petrophysical and hydraulic rock parameters and for geomechanical tests.

This section provides a detailed description of the theoretical background and methods for laboratory testing, as well as the selection and initial characteristics of the sample material. Units and explanations to abbreviations are given in the Abbreviations section.

Sample preparation

Prior to testing, accurate preparation of the samples was required to meet all appropriate testing standards for the different methods. The samples were drilled with a diameter of 50 mm from the original rock core parallel to its vertical axis. To achieve a length-to-diameter ratio of 2:1 according to the requirements of the geomechanical testing standards (Mutschler 2004; Ulusay 2015), the specimens were cut to a standard length of 100 mm and ground for smooth end faces to obtain the best possible cylindrical geometry. After preparation, the samples were dried in an oven at 105 °C for 48–72 h until mass constancy was achieved (Teklu et al. 2018).

Hydraulic parameters

Porosity and characterization of the effective pore network

Prior to hydrostatic testing of the rock core samples, the initial effective porosity of the rock matrix was measured using non-destructive and destructive methods. To determine the maximum effective porosity, each sample was measured by injection of gas in a helium pycnometer (helium porosimetry, HEP). The effective porosity $\Phi^{\max}$ (1) can be calculated by directly measuring the helium grain volume V_g^{He} and the initial bulk volume V_b^i of the sample (McPhee et al. 2015):

$$\Phi^{\max} = \left(1 - \frac{V_g^{\mathrm{He}}}{V_b^i}\right) * 100\%. \tag{1}$$

Accordingly, the bulk density ρ_b and particle density ρ_m of the rock samples can be calculated as a ratio of the dry weight and the respective volume of the rock sample. Furthermore, the effective porosity was measured by a saturation and weighing method (water immersion porosimetry, WIP) using a water similar to the reservoir fluid. The initial porosity Φ^i (2) was calculated by the ratio of pore volume to sample volume by measuring the dry mass of the sample W_d and the saturated mass after saturation of the rock samples under vacuum in a desiccator W_s^w (Anovitz and Cole 2015; McPhee et al. 2015):

$$\Phi^i = \frac{(W_s^w - W_d)}{\rho_f V_b^i} * 100\%, \tag{2}$$

where ρ_f is the density of the saturation fluid. A detailed description of both methods and their limitations was recently published by Bohnsack et al. (2020).

For a more detailed characterization of the pore network, the distribution of the pore entry diameter was measured using mercury intrusion porosimetry analysis (MIP), which is based on a pressurized mercury intrusion. The capillary pressure P_c^{Hg} was converted to the corresponding pore throat diameter d (3) based on the Washburn equation (Webb 2001; Washburn 1921):

$$d = -\frac{4\gamma\cos\theta}{P_c^{\mathrm{Hg}}}, \tag{3}$$

where γ is the interfacial tension (480 erg cm^{-1} for a mercury/air system), P_c^{Hg} is the capillary pressure, θ is the mercury contact angle of 140°, and d is the pressure equivalent pore throat diameter.

The total volume of the mercury-filled pore network is equivalent to the cumulative volume of mercury injected into the sample after the last pressure step. It can be expressed as mercury porosity Φ^{MIP} (4) by the ratio of the maximum intruded mercury volume $V_{\mathrm{max}}^{\mathrm{Hg}}$ to the sample volume V_{b}:

$$\Phi_{\mathrm{MIP}} = \left(\frac{V_{\mathrm{max}}^{\mathrm{Hg}}}{V_{\mathrm{b}}^{i}} \right) * 100\%. \tag{4}$$

The distribution of pore throat sizes d can be calculated by the first derivative of the intruded mercury volume δV^{Hg} and the capillary pressure curve δP_c^{Hg} as probability distribution function pdf (5) (Wu et al. 2019; Alyafei et al. 2016):

$$\mathrm{pdf} = \mathrm{d} * \frac{\delta \mathrm{V}^{\mathrm{Hg}}}{\delta \mathrm{d}} = -\mathrm{P}_c^{\mathrm{Hg}} \frac{\delta \mathrm{V}^{\mathrm{Hg}}}{\delta \mathrm{P}_c^{\mathrm{Hg}}} = -\frac{\delta \mathrm{V}^{\mathrm{Hg}}}{\delta \mathrm{ln} \mathrm{P}_c^{\mathrm{Hg}}} \tag{5}$$

Based on the distribution of the pore throat sizes, a porous rock can be categorized according to specific pore types: sub-capillary pore throats when $d < 0.4$ μm (micro-throats), capillary pore throats when $0.4 < d < 8.4$ μm (meso-throats) and $8.4 < d < 60$ μm (macro-throats), and supra-capillary pore throats when $d > 60$ μm (mega-throats) (Kashif et al. 2019; Nabawy et al. 2009).

Permeability

Darcy (1856) defined that the water flow through a column is directly proportional to the hydraulic head and inversely proportional to the column length. Darcy's law (6) can be expressed in an anisotropic form as

$$\vec{q} = -\kappa \cdot \nabla h, \tag{6}$$

where $\bar{q}$ is the specific discharge vector describing a movement of a fluid volume through a unit area of porous medium per unit time, κ is the hydraulic conductivity with the negative sign denoting fluid flow from high pressure to low pressure regions, ∇ is a vector differential operator (gradient), and h is the piezometric head (Darcy 1856; Cheng 2016).

The piezometric head h (7) is defined as

$$h = \frac{P_p}{\rho_{\mathrm{f}} g} + z, \tag{7}$$

where ρ_{f} is the fluid density, g is the gravity acceleration (9.81 m s^{-2}) and z the elevation (in Cheng (2016) based on Bear (1988)).

To describe the intrinsic permeability as a material constant directly related to geometric properties of a porous medium, Darcy's law (6) can also be expressed by integrating a mobility coefficient ($\kappa = \frac{k}{\mu_{\mathrm{f}}}$), resulting in the following (8):

Bohnsack *et al. Geotherm Energy* (2021) 9:15

Page 9 of 59

$$\bar{q} = -\frac{k}{\mu_f} \cdot \nabla h, \tag{8}$$

where k is the intrinsic permeability and μ_f is the dynamic fluid viscosity (Bear 1988; Cheng 2016).

In the integral form, the Darcy law can be written as

$$Q = -k \frac{\gamma_f}{\mu_f} \cdot \frac{dh}{dx} \cdot A, \tag{9}$$

where Q is the flow rate, γ_f is the unit weight of the fluid, $-\frac{dh}{dx}$ is the hydraulic gradient, and A the cross-sectional area of flow.

When constant fluid flow has been established during permeability tests (steady state), the pressure difference between the upstream and downstream pore pressure ports can be used for the permeability measurement and (9) can be rewritten into the following form (10) (Heiland 2003):

$$k = \frac{Q \cdot \mu_f \cdot l}{a \cdot \Delta P_p}, \tag{10}$$

where ΔP_p is the pressure drop across the sample length l and the cross-sectional area a.

Mechanical parameters

Wave velocity and dynamic moduli

Ultrasonic testing was carried out as a non-destructive laboratory test to determine the propagation of sound waves in a porous material. The ultrasonic test was performed on the same specimens that were subsequently used for measurement of the static moduli.

The v_p-velocity of the dry rock sample was determined in an ultrasonic transmission test (compressional or longitudinal wave) at ambient pressure and temperature conditions with a frequency of 20 kHz according to DIN EN 14579 (2005). In a second test, the v_s-velocity (shear or transverse wave) and dilatational wave (v_d) were determined and the elastic moduli could be calculated using the extensional wave method of Rentsch and Krompholz (1961) and in accordance with DIN EN 14146 (2004).

According to Schön (2015), the modulus of elasticity (Young's modulus, E^{dyn}) (11), shear modulus (G^{dyn}) (12), bulk modulus (K^{dyn}) (13), and Poisson's ratio (v) (14) were calculated from the results of the acoustic measurements as follows:

$$E^{dyn} = \rho_b \cdot v_d^2, \tag{11}$$

$$G^{dyn} = \rho_b \cdot v_s^2, \tag{12}$$

$$K^{dyn} = \rho_b \cdot \left(v_p^2 - \frac{4}{3} \cdot v_s^2 \right), \tag{13}$$

$$v^{dyn} = \frac{3 \cdot K^{dyn} - E^{dyn}}{6 \cdot K^{dyn}}, \tag{14}$$

where ρ_b is the bulk density of the sample.

Rock strength

The uniaxial compression tests were carried out at ambient pressure and temperature conditions on dry cylindrical sample cores according to the German recommendation for uniaxial compression tests with free lateral propagation (Mutschler 2004). The test samples were then loaded at a constant deformation rate of 1×10^{-3} mm s^{-1} (strain rate of 1×10^{-5} s^{-1}) until complete failure of the rock, while the load was measured continuously using a load cell. The axial and radial deformations were recorded by linear variable differential transformers (LVDT) to determine strain deformation.

The uniaxial compressive strength σ_s (UCS) (15) is defined from the stress–strain curve as the maximum force F_{max} applied to the initial end face surfaces A of the sample:

$$\sigma_s = \frac{F_{max}}{A},\tag{15}$$

If the length/diameter ratio of the test sample was less than 2, the compressive strength σ_s had be corrected following the recommendations and standards using (16) of Obert and Duvall (1967):

$$\sigma_s^c = \frac{8 \cdot \sigma_s}{7 + 2 \cdot \frac{D}{L}},\tag{16}$$

where σ_s^c is the corrected uniaxial compressive strength and D and L are the diameter and length of the sample.

The sample was pre-loaded, unloaded and re-loaded within the linear-elastic range until the rock sample failed completely. The static Young's modulus E (17) was determined in the reloading curve of the linear section of the stress–strain curve as follows:

$$E = \frac{\Delta\sigma}{\Delta\varepsilon_a{}^{el}},\tag{17}$$

with $\Delta\sigma$ is the differential axial stress and $\Delta\varepsilon_a{}^{el}$ is the differential axial strain during linear elastic deformation (ε_a is positive in a compactive stress regime).

The Poisson's ratio ν (18) was calculated by the ratio of axial and lateral strains:

$$\nu = \frac{\Delta\varepsilon_a}{\Delta\varepsilon_c},\tag{18}$$

where $\Delta\varepsilon_a$ is the differential axial strain and $\Delta\varepsilon_c$ is the differential circumferential strain.

Poroealstic behavior under hydrostatic conditions

To investigate the influence of stress on the hydraulic properties of a porous carbonate rock, the rock samples were tested in a triaxial test cell in a hydrostatic stress regime. In contrast to the UCT, where only vertical stress is applied to the test samples, the samples were also radially pressurized inside a triaxial test vessel by hydraulic oil. To achieve hydrostatic stress conditions, all three principle normal stresses were controlled uniformly by applying a confining pressure P_c (19):

$$P_c = \sigma_1 = \sigma_2 = \sigma_3 > 0 \tag{19}$$

where σ_1 is the vertical stress and σ_2, σ_3 are the radial stresses.

Varying stress conditions have different effects on the rock and pore volume of a porous body, depending on the test conditions. An increase in the hydrostatic pressure results in a change (decrease) of the rock volume. According to Terzaghi (1923), a change in volume directly affects the pore pressure P_p of a saturated porous medium and thus the effective pressure P_e (20):

$$P_e = P_c - P_p. \tag{20}$$

According to the theory of Biot (1941), poroelasticity is governed by the kinematic evolution of the bulk volume of a porous medium and the change in the mass content of the fluid (Hassanzadegan and Zimmermann 2014). According to Detournay and Cheng (1993), the bulk volumetric strain ε_v (21) and the fluid volume V_f can be related in terms of their conjugate dynamic quantities confining pressure P_c and pore pressure P_p by a fundamental equation of poroelasticity (Hassanzadegan and Zimmermann 2014):

$$\varepsilon_v = \frac{P_c - \alpha P_p}{K_d}, \tag{21}$$

where α is the Biot effective stress coefficient and K_d is the drained bulk modulus.

Under isothermal drained conditions, the pore pressure is constant ($\Delta P_p = 0$). The Biot effective stress coefficient α (22) can be determined by the ratio of changes in the expelled fluid volume ΔV_Φ (equivalent to the pore volume) to changes in the drained bulk volume ΔV_b of a porous medium (Blöcher et al. 2014; Hassanzadegan et al. 2012; Fabre and Gustkiewicz 1997):

$$\alpha = \frac{\Delta V_\Phi}{\Delta V_b} = \frac{\Delta V_\Phi}{V_b^i \Delta \varepsilon_v} = 1 - \frac{K_d}{K_s}, \tag{22}$$

where $\Delta \varepsilon_v$ is the change in bulk volumetric strain and K_s is the bulk modulus of the solid phase.

Furthermore, the drained moduli and compressibility of the pores and bulk can be calculated under the described conditions. The pore volume compressibility C_Φ (and the inverse porosity modulus K_Φ) describes the change in pore volume due to the deformation of a porous solid under different stress conditions (Oliveira et al. 2016). It can be determined as the slope of the pore volume V_Φ and the incremental change of the effective stress P_e at a certain pore pressure P_p (23) (Oliveira et al. 2016; Ghabezloo et al. 2009b):

$$C_\Phi = -\frac{1}{V_\Phi}\left(\frac{dV_\Phi}{dP_e}\right)_{P_p} = \frac{1}{K_\Phi}. \tag{23}$$

The initial pore volume was determined using the WIP method, while the changes in pore volume during the drained hydrostatic tests were measured.

The drained bulk modulus of elasticity K_d (24) is a strong function of the confining pressure and can be determined as a tangential slope from the first derivative of the stress–strain curve (Hassanzadegan et al. 2012; Detournay and Cheng 1993):

$$K_d = \frac{dP_e}{d\varepsilon_v} = \frac{V_b^i * dP_e}{d\Delta V_b}. \tag{24}$$

The incremental change in bulk volumetric strain as a function of effective pressure can also be used to find the drained bulk compressibility C_d (25) as (Pei et al. 2018; Zimmerman et al. 1986):

$$C_d = \frac{d\varepsilon_v}{dP_e}, \tag{25}$$

which is also the inverse of the drained bulk modulus K_d (26):

$$K_d = \frac{1}{C_d}. \tag{26}$$

Stress sensitivity of porosity and permeability

During hydrostatic loading, the core samples undergo compressive deformation in response to the changing stress conditions. The sample deformation in turn induces changes in pore volume (porosity) and, therefore, directly affects the effective pore network and thus on the permeability.

Since the pore pressure is constant under drained conditions, compression or expansion of the pore fluid is absent and changes in the bulk volume result in a volumetric mass transfer of the fluid (Hassanzadegan et al. 2014). The expelled fluid volume, therefore, indicates a direct change in the pore volume ΔV_Φ within a porous medium (Blöcher et al. 2014; Cheng 2016).

The evolution of porosity can, therefore, be determined by the change in pore volume ΔV_Φ in relation to the deformed bulk volume V_b. The porosity relative to the total volume of a currently deformed porous medium is defined as Eulerian porosity Φ^E (27) (Blöcher et al. 2009; Nedjar 2013):

$$\Phi^E = \frac{V_\Phi}{V_b} * 100\% = \frac{V_\Phi^i - \Delta V_\Phi}{V_b^i - \Delta V_b} * 100\%, \tag{27}$$

where V_Φ^i is the initial pore volume.

According to Cheng (2016), an induced porosity change of a porous medium is only a function of the Terzaghi effective stress ($P_e = P_c - P_p$) depending on the strength of its pore structure (cementation, pore size, and pore shape). Assuming an ideal porous medium, the porosity change can be described in the form of a constitutive equation (28) as

$$\frac{\Delta\Phi}{1 - \Phi^i} = -C_\Phi \Delta P_e = -\frac{\Delta P_e}{K_\Phi} = -\left\lfloor \frac{1}{K_d} - \frac{1}{\left(1 - \Phi^i\right)K_s} \right\rfloor \Delta P_e, \tag{28}$$

where $\Delta\Phi$ describes the induced porosity change, Φ^i is the initial porosity of the undeformed porous medium and ΔP_e is the change of Terzaghi effective stress.

By adopting the model of Mackenzie (1950) in (28), which shows that the porosity variation is also controlled by the shear modulus of the solid phase of a porous medium, the porosity change (29) can be described as follows:

$$\frac{\Phi^E}{\Phi^i} = e^{-3P_e/4G_s}, \tag{29}$$

where G_s is the shear modulus of the solid constituent and is assumed to be constant (Cheng 2016).

The compaction-induced porosity can also be described in exponential form as function of the effective stress only (30) (Meng et al. 2019):

$$\Phi^E = \Phi^i \cdot e^{-c(P_e-P_i)}, \tag{30}$$

where c is the porosity stress sensitivity coefficient and P_i is the reference effective pressure at which the initial porosity was measured.

As a result of compression, the permeability of a rock can rapidly decrease by orders of magnitude. While changes in porosity are solely a function of effective pressure (Cheng 2016), permeability is controlled either by the varying stress state or in response to changes in the effective pore network (Ghabezloo et al. 2009b). Due to the closure of pore throats, which connect pores and mainly control permeability within a porous network, permeability reacts very sensitive to compressive stresses. Taking into account a time-dependent deformation of the sample (creep), permeability changes can occur even at a constant state of stress which are only related to changes in porosity (Ghabezloo et al. 2009b).

Hence, based on an empirical porosity–permeability power law described by Walder and Nur (1984), the following relationship (31) can be stated (David et al. 1994; Xu et al. 2018):

$$k = k^i \cdot \left(\frac{\Phi^E}{\Phi^i}\right)^{\beta}, \tag{31}$$

where k^i is the initial permeability, $\frac{\Phi^E}{\Phi^i}$ is the relative porosity change, and β functions as the stress sensitivity exponent of this empirical power law based on experimental data.

In contrast, assuming elastic deformation of the sample, permeability can be determined by a simplified effective stress law independent of porosity changes (Ghabezloo et al. 2009a). By substituting (29) into (31), an exponential law (32) can be found for the intrinsic permeability as a function of stress only:

$$k = k^i \cdot e^{-\frac{3\beta P_e}{4G_s}} = k^i \cdot e^{-b(P_e-P_i)}, \tag{32}$$

where b depicts the permeability stress sensitivity coefficient based on an experimentally measured composite constant (Cheng 2016; David et al. 1994).

A further model for evaluating stress sensitivity was proposed by Jones and Owens (1980) in logarithmic form. They found a relationship between the square root of the relative stress-induced porosity/permeability and the logarithm of the relative change in

effective stress. The stress sensitivity can be evaluated with this model as the stress sensitivity coefficient S_s (33) (Xu et al. 2018):

$$S_s^{\Phi} = \frac{1 - \left(\Phi^E / \Phi^i\right)^{1/3}}{\log(P_e/P_i)} \text{ for porosity and,}$$

$$S_s^k = \frac{1 - (k/k^i)^{1/3}}{\log(P_e/P_i)} \text{ for permeability,} \tag{33}$$

where S_s^{Φ} and S_s^k are the stress sensitivity coefficients for porosity and permeability.

Hydrostatic compression tests—experimental setup

Prior to the investigation of stress sensitivity, each sample was tested in a multi-phase preparation cycle following the test procedures of several authors (Pei et al. 2018; Pei et al. 2014; Blöcher 2008; Blöcher et al. 2014; Hart and Wang 1995; Hassanzadegan and Zimmermann 2014).
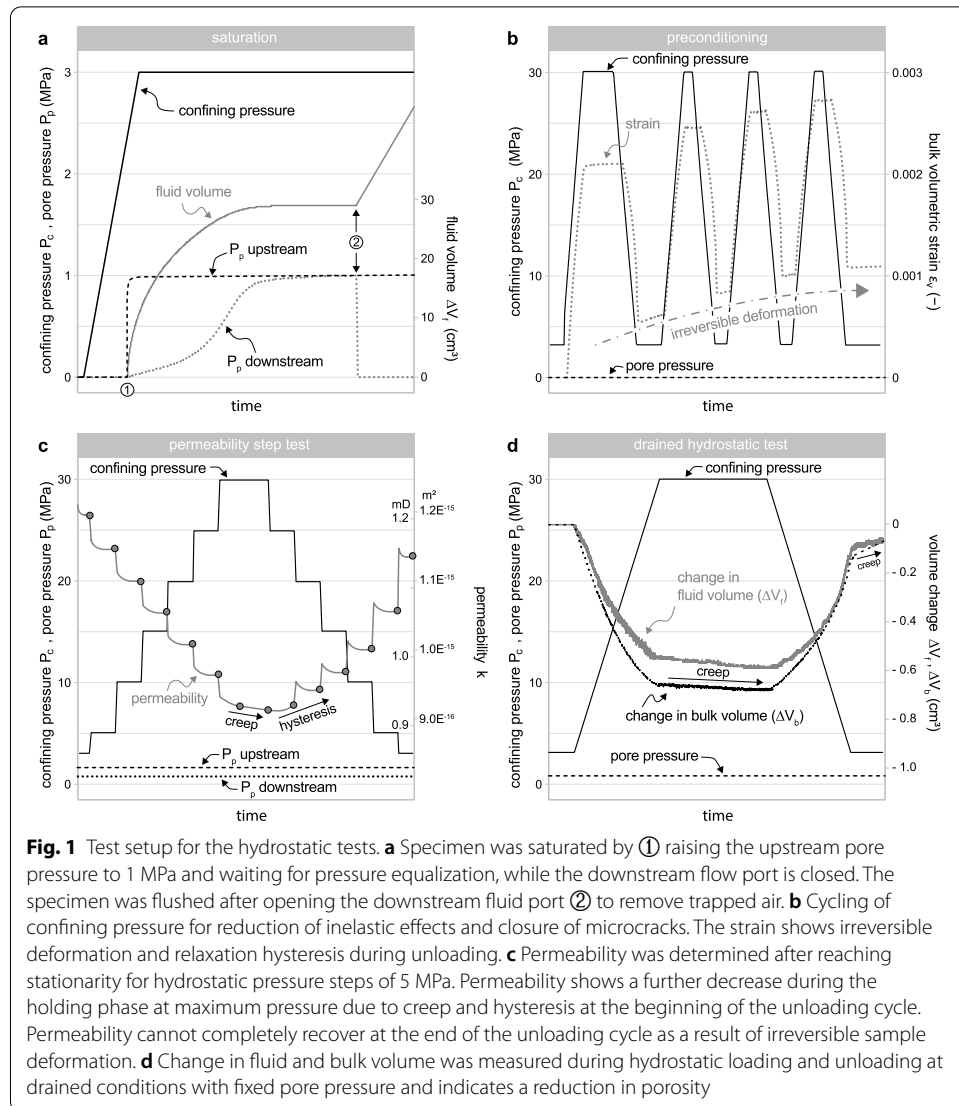
After mounting the rock sample in the triaxial test cell, the sample was saturated and preconditioned in preparation for the hydrostatic compression tests. Following preconditioning, two different drained hydrostatic tests related to changes in confining pressure were performed: a compression stage test with measurement of permeability at different pressure stages and a slow-ramp compression test at constant pore pressure to monitor fluid and bulk volume changes during compression and relaxation. Volumetric deformation, pore pressure, and temperature were monitored during each test by axial/radial extensometers, pressure transducers, and temperature probes located within the pressure vessel directly outside of the sample and on the pore pressure transducers.

Saturation

After drying the core sample at 105 °C for 48–72 h (following Teklu et al. 2018), the test specimen was jacketed with a pressure and temperature resistant silicone sleeve and mounted into the triaxial test cell. The jacketed specimen was equipped with one circumferential and two axial extensometers (high-precision LVDT's) and connected to the pore pressure system at the bottom and top adapter plates. Before saturation, the sample and pore lines were evacuated with a vacuum pump for several hours to check the system for leakage and prepare it for saturation by the pore fluid. The triaxial vessel was then filled by hydraulic oil and pressurized to 3 MPa before de-aired and de-ionized water was injected into the specimen via the upstream port at a back pressure of 1 MPa (downstream port is closed) (Fig. 1a). After the upstream and downstream pore pressures equalized, the upstream port was opened and the specimen was flushed ($P_p^{up} = 1$ MPa, $P_p^{down} = 0$ MPa) for several hours to remove trapped air from the pore network until the outflow from the specimen equaled the inflow.

Preconditioning

For elimination of non-linear effects and reduction of irreversible deformation (microcracks may have formed during relaxation of the rock cores at subsurface conditions), each specimen was preconditioned by cycling of a hydrostatic loading between 3 and

Fig. 1 Test setup for the hydrostatic tests. **a** Specimen was saturated by ① raising the upstream pore pressure to 1 MPa and waiting for pressure equalization, while the downstream flow port is closed. The specimen was flushed after opening the downstream fluid port ② to remove trapped air. **b** Cycling of confining pressure for reduction of inelastic effects and closure of microcracks. The strain shows irreversible deformation and relaxation hysteresis during unloading. **c** Permeability was determined after reaching stationarity for hydrostatic pressure steps of 5 MPa. Permeability shows a further decrease during the holding phase at maximum pressure due to creep and hysteresis at the beginning of the unloading cycle. Permeability cannot completely recover at the end of the unloading cycle as a result of irreversible sample deformation. **d** Change in fluid and bulk volume was measured during hydrostatic loading and unloading at drained conditions with fixed pore pressure and indicates a reduction in porosity

30 MPa (Blöcher 2008; David et al. 2015). The confining pressure was loaded and unloaded at a constant ramp in four cycles at drained conditions with the pore pressure system open to the reservoir (Fig. 1b). Between the loading and unloading cycles, confining pressure was kept constant to allow time-dependent deformation (creep) and to monitor hysteresis effects (Pei et al. 2018). The first cycle was operated with a pressure change rate of 4 MPa min^{-1} and a holding phase of 4 min each, while the remaining cycles were loaded and unloaded at 8 MPa min^{-1} and a holding phase of 2 min each.

Permeability stage test

For the initial permeability measurements, the hydrostatic stress was maintained at initial conditions of $P_c = 3$ MPa ($\sigma_1 = \sigma_2, \sigma_3$) and a constant inflow of de-aired and de-ionized water was applied at a rate of $Q_{up} = 0.15$ ml min^{-1}. The downstream pore pressure was held constant at $P_p^{down} = 1$ MPa, while the upstream pore pressure settled in a range

of $P_p^{up} = 1.0 - 1.5$ MPa. After achieving stationary flow conditions between the up- and downstream pump ($Q_{up} = Q_{down}$) and stabilization of the differential pore pressure, the flow through the sample was measured in time steps of 5 min over a period of at least 4 h to reduce noise. The temperature of the fluid and at the sample were recorded during the test for accurate determination of the fluid properties. The permeability was calculated by Eq. (34) adapting the steady-state method of Darcy (10):

$$k = \frac{Q \cdot \mu_f \cdot l_d}{a_d \cdot \Delta P_p},$$

(34)

where l_d and a_d are the length and cross-sectional area of the sample in the deformed state.

After measuring the permeability at initial conditions, the hydrostatic stress was increased in steps of $P_c = 5$ MPa. The permeability measurement was repeated for each of these steps until stationary flow conditions were reached (Fig. 1c). During the permeability measurements, the boundary conditions were kept constant to ensure the validity of Darcy's law (Heiland 2003). While maintaining a constant pressure at each step, the deformation of the sample continued slightly (creep). Thus, the permeability for the characteristic pressure was only taken at the end of each step after reaching stationarity. After reaching the upper limit of the test device at $P_c = 30$ MPa, the stress was maintained for 8 h and the permeability was measured at the beginning and end of the holding phase to identify the impact of irreversible creep at maximum pressure. Subsequently, the hydrostatic stress was decreased again to measure the permeability during the unloading phase.

The test procedure was performed at isothermal conditions (30 °C) and the temperature of the fluid and at the sample in the pressure vessel was monitored during the test for correction of the fluid viscosity. For determination of L_d and A_d during sample deformation, bulk volumetric strain was monitored throughout the test.

Drained hydrostatic test

Hydrostatic compression tests were conducted under isothermal and drained conditions to determine the poroelastic behavior of the rock samples. The samples were saturated and underwent preconditioning before hydrostatic testing to minimize inelastic effects. The initial stress conditions were set to $P_c = 3$ MPa ($\sigma_1 = \sigma_2, \sigma_3$) and the pore pressure was kept constant throughout the test procedure at the upstream and downstream pressure ports ($P_p^{up} = P_p^{down} = 1$ MPa) to allow a continuous measurement of the pore volume change (ΔV_Φ) (Blöcher et al. 2014). The temperatures in the pressure vessel and the pore fluid were kept constant ($T = 30$ °C) and monitored with several temperature probes to exclude thermal effects. After the initial conditions were set, the confining pressure was continuously increased at a loading rate of 6 MPa h^{-1} to a maximum of 30 MPa and then kept constant for 3 h to check for creep and hysteresis effects (Fig. 1d). After the holding phase, the confining pressure was decreased at the same rate of 6 MPa h^{-1} to initial conditions (unloading), followed by a further holding phase of 3 h.

Axial and circumferential strain measurements were recorded continuously to calculate the sample deformation as bulk volumetric strain ε_v (35):

$$\varepsilon_{\mathrm{v}} = \frac{\Delta V_{\mathrm{b}}}{V_{\mathrm{b}}^{i}} = \varepsilon_{\mathrm{a}} + 2\varepsilon_{\mathrm{c}} \ \text{with} \ \varepsilon_{\mathrm{a}} = \frac{\Delta l}{l}, \varepsilon_{\mathrm{c}} = \frac{\Delta C}{C}, \tag{35}$$

where l and Δl are the length and the length difference of the sample, C and ΔC are the circumference and circumference difference, and $\varepsilon_{\mathrm{v}} > 0$ in a compactive stress regime (Hassanzadegan et al. 2014).

Therefore, the bulk volume of the sample in the deformed state V_{b} can be determined by (36):

$$V_{\mathrm{b}} = V_{\mathrm{b}}^{i} - \Delta V_{\mathrm{b}} \ \text{with} \ \Delta V_{\mathrm{b}} = \varepsilon_{\mathrm{v}} V_{\mathrm{b}}^{i}. \tag{36}$$

Knowing the deformation of the bulk volume V_{b} from (36) and the change in pore volume ΔV_{Φ}, the compaction-induced porosity reduction can be expressed as Eulerian porosity Φ^{E} using (27).
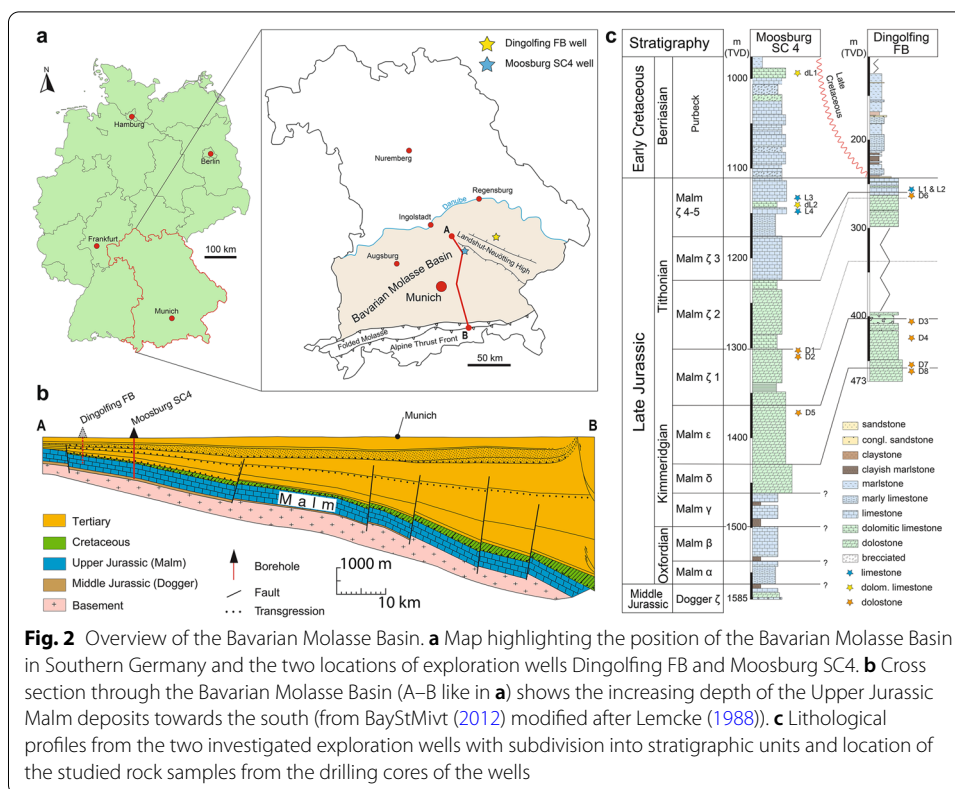
Furthermore, some poroelastic parameters can be derived from the drained hydrostatic test. The drained bulk modulus K_{d} and the drained bulk compressibility C_{d} can be calculated from the stress–strain curves using (24) to (26). The Biot effective stress coefficient α can be determined as the ratio of the changes in pore volume ΔV_{Φ} to the changes in the drained bulk volume ΔV_{b} by (22) (Blöcher et al. 2014; Hassanzadegan et al. 2012), and the pore compressibility C_{Φ} (and the inverse porosity modulus K_{Φ}) by the pore volume change as a function of the effective pressure (23).

Sample material and initial sample characteristics

Sample material from rock cores of the Upper Jurassic aquifer rocks within the Molasse Basin is generally very rare. Consequently, the distribution of rock parameters within the highly heterogeneous carbonate deposits is widely unknown (Bohnsack et al. 2020). However, the deformation and poroelastic response of a porous rock are based on complex mechanisms that may depend on its initial properties such as porosity, permeability, size and shape of pores, rock strength, and the elasticity of a rock. Therefore, a detailed characterization of the differnet rock types as well as the microstructural and hydraulically effective properties of the Malm aquifer rocks was carried out to allow conclusions on the stress sensitivity within the very heterogeneous carbonate types of the Malm reservoir.
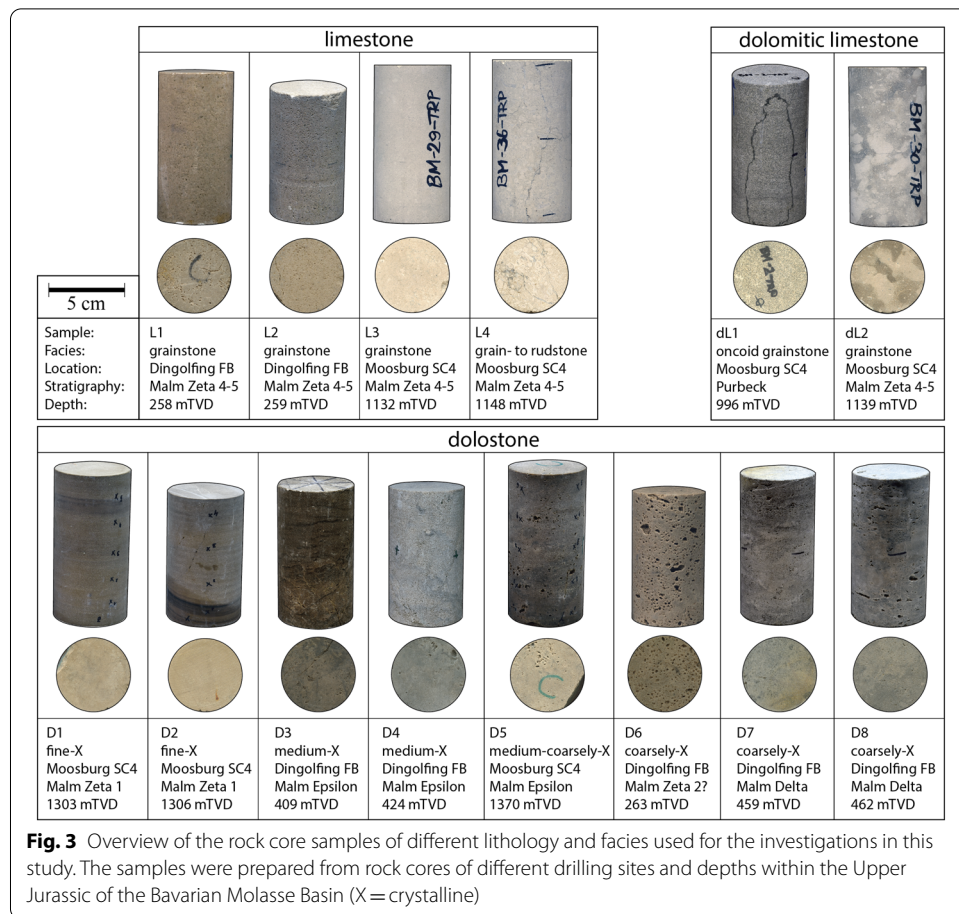
Sample material and general geology

In this study, two drill cores of the wells Moosburg SC4 (MSC-4) and Dingolfing FB (DGF-FB), located in the Bavarian Molasse Basin northeast of Munich, were investigated (Fig. 2a). The Molasse Basin represents a wedge-shaped alpine foreland basin formed by tectonic movements during the alpine orogeny and extends along the northern flank of the Alps as far north as the Franconian Alb (Büchi et al. 1965; Bachmann et al. 1987). The Upper Jurassic strata plunge southwards beneath the fringe of the Alps (Fig. 2b) and can reach a thickness of up to 400 m (Goldbrunner and Vasvári 2016; Mraz et al. 2019). Within the central Bavarian Molasse Basin, it is composed of alternating shallow marine sequences of limestones, marls, and dolostones. The aquifer characteristics of the Upper Jurassic (Malm) aquifer are very heterogeneous throughout the basin due to local variations of the depositional environment, sedimentary, and diagenetic features as well

Fig. 2 Overview of the Bavarian Molasse Basin. **a** Map highlighting the position of the Bavarian Molasse Basin in Southern Germany and the two locations of exploration wells Dingolfing FB and Moosburg SC4. **b** Cross section through the Bavarian Molasse Basin (A–B like in **a**) shows the increasing depth of the Upper Jurassic Malm deposits towards the south (from BayStMivt (2012) modified after Lemcke (1988)). **c** Lithological profiles from the two investigated exploration wells with subdivision into stratigraphic units and location of the studied rock samples from the drilling cores of the wells

as irregular fractures, faults, and locally intense karstification (Koch et al. 1994; Keupp et al. 2007; Koch and Munnecke 2016; Mraz 2018; Niebuhr 2014). Therefore, petrophysical and hydraulic properties of the aquifer rock are presumed to be variable throughout this carbonate platform setting as well.

The cores of the investigated exploration drillings MSC-4 and DGF-FB comprise a complete succession of the Upper Jurassic sediments. The lithology and facies of the stratigraphic intervals were described in detail and used as reference data for correlation towards the center of the basin (Bohnsack et al. 2020; Böhm et al. 2011; Meyer 1994). The carbonate succession is dominated by limestone, dolomitic limestone, and dolostone with a very heterogeneous distribution of facies and petrophysical properties throughout the Upper Jurassic (Malm) section. For detailed analysis of the rock properties, several sample intervals were selected along the rock cores according to rock quality and facies for further laboratory investigations (Fig. 2c).

A total of 14 sample intervals were selected to cover typical lithology and facies classes that occur in the target zones for geothermal exploration in the Bavarian Molasse Basin. The samples were documented by photographs, high-resolution scans, and a detailed thin section analysis to characterize the heterogeneity of the material. Figure 3 shows a brief overview and description of the investigated test specimens.

Fig. 3 Overview of the rock core samples of different lithology and facies used for the investigations in this study. The samples were prepared from rock cores of different drilling sites and depths within the Upper Jurassic of the Bavarian Molasse Basin (X = crystalline)

Lithology, facies, and pore characteristics

To cover the heterogeneity of the Upper Jurassic carbonate sequence as widely as possible, samples of different lithology and facies were selected for the hydrostatic tests. Since sample availability from drilling cores of the reservoir is generally scarce and multiple samples of the same facies and depth were required for testing, the selection had to be limited to a few intervals. Therefore, a set of 14 sample types of different facies intervals could be used for the tests—4 limestone, 2 dolomitic limestone, and 8 dolostone intervals. The sample selection allowed to cover the majority of the stratigraphic spectrum within the geothermal reservoir from the Malm Delta to Malm Zeta 4–5 intervals of the Upper Jurassic. Additionally, a limestone sample from an analogue outcrop of the Franconian Alb north of the Molasse Basin was investigated to complete the lithological variation. For the differentiation and description of the lithology and facies for limestone, the classifications of Dunham (1978) and Folk (1974) were used. The description for dolostone is mainly based on Sibley and Gregg (1987) and other authors (Sibley et al. 1993; Friedman 1965; Randazzo and Zachos 1984). The classification of porosity and pore types in thin sections is based on the fundamentals of Choquette and Pray (1970). The geometry of the pores and the pore throat sizes were classified using the the

Table 1 Pore size characteristics of the rock samples investigated by mercury intrusion porosimetry (MIP)

Sample	Lithology	Facies	Pore classification			Pore throat classification						
			Φ^i	Predominant pore type	Subordinate pore type	d_ϕ^{min}	d_ϕ^{med}	d_ϕ^{max}	Micro	Meso	Macro	Mega
			(%)			(µm)			(in % of total pore throats)			
L1	Limestone	Grainstone	13.0	inter-P 50–200 µm	v <1 mm	0.02	0.1	44.9	**67.9**	10.5	12.0	9.6
L2	Limestone	Grainstone	14.5	inter-P 50–200 µm	v <1 mm	0.02	17.8	64.0	11.3	18.4	**59.4**	10.9
L3	Limestone	Grainstone	18.1	inter-P 50–100 µm	oo-mo >150 µm	0.13	0.7	2.5	18.9	**74.0**	2.1	5.1
L4	Limestone	Rudstone	12.7	inter-P 100–300 µm	Mi <0.4 µm	0.08	0.5	2.0	29.1	**66.6**	2.2	2.1
dL1	Dolomitic limestone	Grainstone	13.0	inter-P 20–150 µm	inter-X <5 µm	0.04	0.8	16.2	16.7	**67.5**	11.8	4.0
dL2	Dolomitic limestone	Grainstone	15.0	inter-X 20–150 µm	intra-P & mo 20–120 µm	0.07	0.4	1.7	**54.7**	40.9	2.0	2.5
D1	Dolostone	Fine-X	14.9	inter-X <25–125 µm	el. inter-X <500 µm	1.09	5.9	12.3	1.4	**83.9**	12.2	2.5
D2	Dolostone	Fine-X	9.8	inter-X <25–125 µm	el. inter-X <500 µm	0.81	2.4	11.3	3.4	**85.7**	7.2	3.7
D3	Dolostone	Medium-X	8.9	inter-X <50 µm	el. inter-X <250 µm	0.05	7.9	101.2	11.5	38.6	**38.9**	11.0
D4	Dolostone	Medium-X	8.2	inter-X <24 µm	el. inter-X <500 µm	0.05	25.4	126.1	8.7	30.9	**36.5**	23.9
D5	Dolostone	Medium-X	2.3	v 250 µm–2 mm	inter-X <<100 µm	0.01	13.6	138.4	11.6	16.8	**43.6**	28.1
D7	Dolostone	Coarsely-X	4.0	mo-v 250 µm–2 mm	inter-X <50 µm	0.01	32.1	198.8	16.6	15.2	27.8	**40.4**
D8	Dolostone	Coarsely-X	3.7	v 250 µm–1 mm	inter-X <50 µm	0.03	13.9	142.0	32.5	11.5	17.3	**38.7**

Bold values indicate predominant magnitude of the pore throats

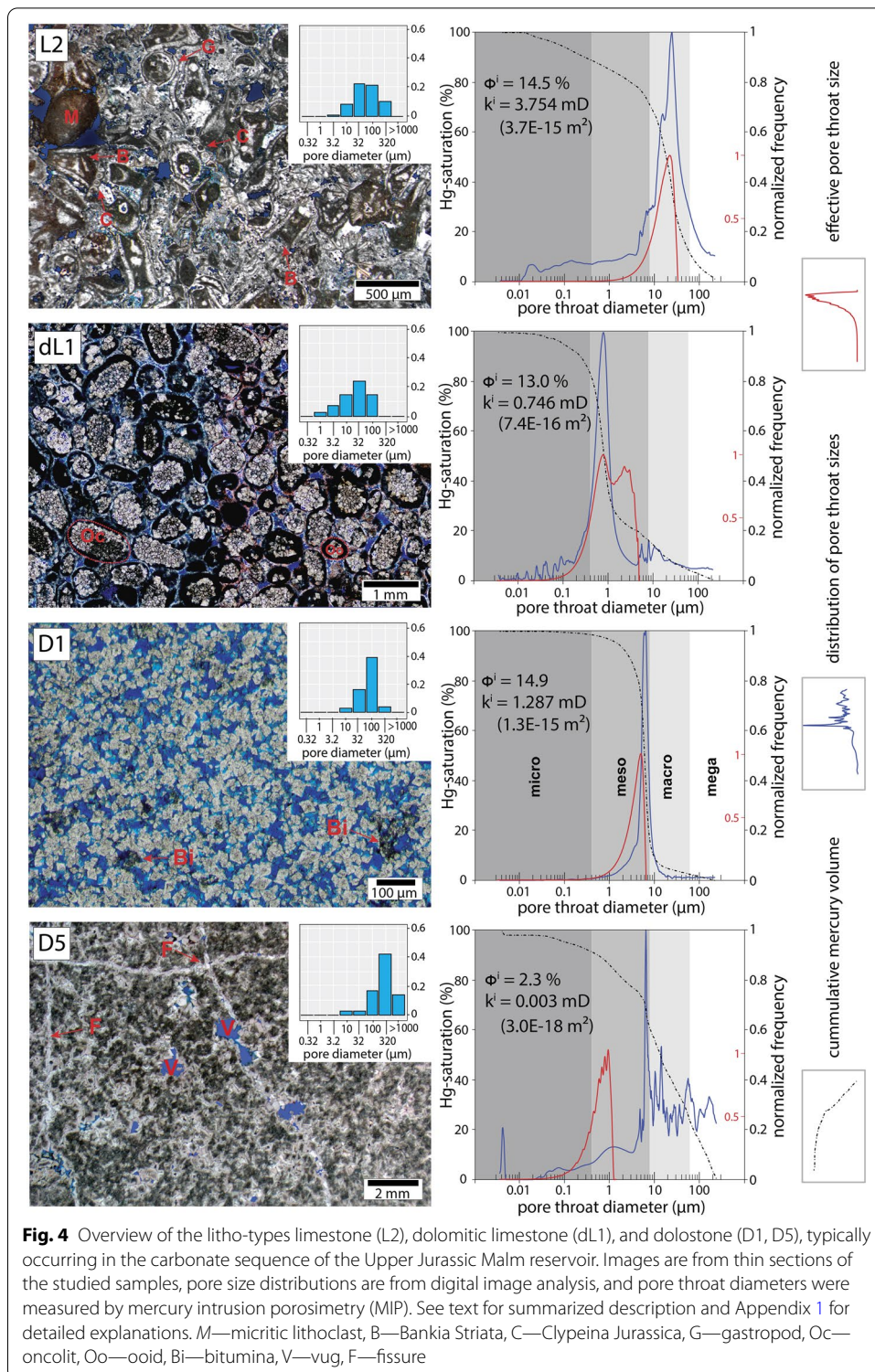*X* crystalline, Φ^i initial porosity, *inter-P* interparticle pores, *intra-P* intraparticle pores, *inter-X* intercrystalline, *el. inter-X* elongate intercrystalline pores, *v* vugs, *mo-v* moldic vugs, *oo-mo* oo-moldic pores, *mo* moldic pores, *mi* micropores, d_ϕ^{min} minimum diameter, d_ϕ^{med} median diameter, d_ϕ^{max} maximum diameter

capillary curves of the MIP tests using the work of Luo and Machel (1995) and Kashif et al. (2019) as a guideline.

A brief description of each lithotype is given in the following section and the key results are summarized in Table 1. A comprehensive description of the components, pore types, and diagenetic overprinting for each facies type according to thin section and capillary pressure curve (MIP) analysis is additionally provided in Appendix 1.

Limestone and dolomitic limestone   The limestone samples are characteristic of the uppermost part of the Malm aquifer, which is progressively dolomitized with increasing depth in the two investigated wells (Bohnsack et al. 2020; Meyer 1994; Böhm et al. 2011). A succession of Upper Malm (Zeta 4–5) grainstones represents the hydraulically more productive facies and is, therefore, sufficiently characteristic for the investigations. The grainstones are mainly bioclastic peloid- and ooid-grainstones with reworked bio- and lithoclasts, typical in the Upper Jurassic of the entire Molasse Basin. In addition, fragments of the green algae *Campbelliella "Bankia" Striata* (Carozzi) and *Clypeina Jurassica* (Favre), commonly with micritic envelopes, are rock-forming in this shallow marine facies (Figs. 4L2, 16L1–4). As organisms, sponge fragments, bivalves and gastropods, as well as benthic foraminifers frequently occur (Figs. 4L2, 16L2–3). The grain structure is seldom completely sparitically cemented and usually shows only initial calcite cement rims between the particles. The pores are mostly irregularly shaped, prolate interparticle pores between fossil fragments or the peloids/ooids of mesoporous size. In some cases, pores of dissolved organisms (molds) also occur (Fig. 16L3). Microporosity is found in the micritic envelopes of the peloids/ooids and in micritic lithoclasts (Fig. 4L2, dL2). Imperfect dolomitization is common in Upper Jurassic aquifer rocks, whereby only some carbonate is transformed to dolomite and the primary facies is still characteristic of the rock. Due to this dolomitization, the effective porosity for some areas of the rock matrix is increased by the formation of intergranular pore space and capillary pore throats between the pores. For example, Fig. 4dL1 shows a partially dolomitized ooid–oncoid grainstone. The nuclei were completely dissolved and transformed into euhedral and subhedral dolomite crystals. The pore space consists mainly of interparticle pores between the ooids/oncoids and small intercrystalline pores between dolomite rhombs.

Dolostone   Many intervals of the Upper Jurassic Malm aquifer in the Bavarian Molasse Basin are completely dolomitized and, therefore, of special interest as targets for geothermal exploration (Mraz 2018; Böhm et al. 2011). Pervasive dolomitization occurred after lithification in a shallow to deep-burial diagenetic environment (Reinhold 1998). According to Machel (2004), the calcite crystals that form a limestone are subsequently replaced by dolomite crystals (replacement dolomite). This can result in a significant increase in intercrystalline and moldic porosity (Machel 1978), unless the pore space is reduced by cementation or clogged by other minerals or aggregates (e.g., bitumina, clay minerals) (Fig. 4D1). The dolostone intervals investigated in this study were almost completely dolomitized, and calcite can only be found as sparse remnants of the dolomitization process or newly formed cement rims. However, dolomitization did not always enhance the hydraulic properties within the Malm aquifer. In deeper intervals of the sampled wells, xenotopic fabrics with subhedral to anhedral dolomite crystals are increasingly devel-

Fig. 4 Overview of the litho-types limestone (L2), dolomitic limestone (dL1), and dolostone (D1, D5), typically occurring in the carbonate sequence of the Upper Jurassic Malm reservoir. Images are from thin sections of the studied samples, pore size distributions are from digital image analysis, and pore throat diameters were measured by mercury intrusion porosimetry (MIP). See text for summarized description and Appendix 1 for detailed explanations. *M*—micritic lithoclast, *B*—Bankia Striata, *C*—Clypeina Jurassica, *G*—gastropod, *Oc*—oncolit, *Oo*—ooid, *Bi*—bitumina, *V*—vug, *F*—fissure

oped, which in fact significantly reduced the effective porosity and permeability. Those types of dolostones often exhibit a moldic and vuggy porosity, caused by dissolution of larger allochems during or after the pervasive dolomitization (Fig. 4D5). However, these

moldic pores and vugs may not be connected to the effective pore network due to the lack of intergranular pores between the dolomite crystals. The development of the primary facies (grain and particle size, porosity, clay content) as well as the duration of the dolomitization process and the further compaction during and after the dolomitization process (type of diagenesis) are of decisive importance for the improvement or deterioration of the hydraulic properties (Lucia 2007).
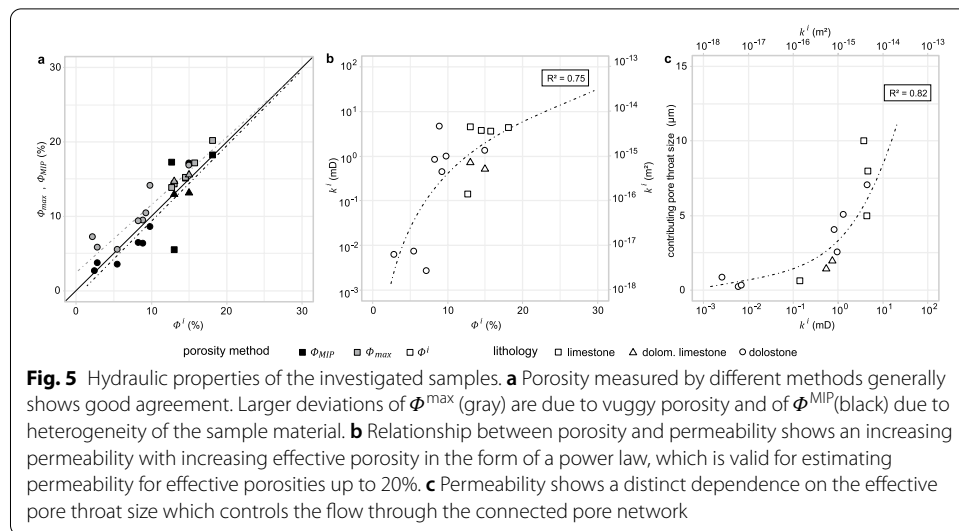
Hydraulic characterization

Each rock sample was tested for its effective porosity and permeability under initial conditions to characterize the hydraulic properties. The effective porosity was tested by water saturation (WIP), helium porosimetry (HEP), and mercury intrusion porosimetry (MIP), to gather information about the pore network. The initial permeability was measured at low confining pressure ($P_c = 3$ MPa) in the triaxial test cell using water as pore fluid. The bulk density and particle density were measured by the HEP method. All basic hydraulic rock parameters for the tested samples are summarized in Table 2.

In general, the results for the tested samples show a higher water effective porosity Φ^i for limestone (12.7–18.1%) and dolomitic limestone (13.0–15.0%) than for dolostone (2.3–14.9%) (Fig. 5a). However, the maximum effective porosity Φ^{max} measured with helium is generally higher by 1–2% p.u. (porosity units), indicating sub-capillary pore throats that cannot be penetrated by water (microporosity). In some dolostone samples the difference is up to 5% p.u. as a result of vuggy pores that are not interconnected within the effective pore network and could not be detected by the WIP method due to technical reasons (see Bohnsack et al. (2020) for details). The effective porosity determined by mercury intrusion (Φ_{MIP}) is generally consistent with the WIP method, except

Table 2 Rock specific characteristics and petrophysical description of investigated rock samples

ID	Lithology	Facies	Depth	Φ^i	Φ^{max}	Φ^{MIP}	k_i		ρ_b	ρ_m	d_{eff}
			mTVD	%			mD	m^2	g cm^{-1}		μm
L1	Limestone	Grainstone	258	13.0	14.3	5.5	4.574	4.5E^{-15}	2.32	2.71	8.1
L2	Limestone	Grainstone	259	14.5	15.2	15.2	3.754	3.7E^{-15}	2.29	2.71	10.0
L3	Limestone	Grainstone	1132	18.1	20.2	18.2	4.423	4.4E^{-15}	2.17	2.72	5.2
L4	Limestone	Rudstone	1148	12.7	13.9	17.3	0.161	1.6E^{-16}	2.34	2.71	0.6
L5	Limestone	Grainstone	0	15.8	17.2	–	0.105	1.0E^{-16}	2.24	2.71	–
dL1	Dolomitic limestone	Grainstone	996	13.0	14.9	13.1	0.746	7.4E^{-16}	2.36	2.77	2.2
dL2	Dolomitic limestone	Grainstone	1139	15.0	15.8	13.3	0.540	5.3E^{-16}	2.34	2.77	1.5
D1	Dolostone	Fine-X	1303	14.9	16.7	16.9	1.287	1.3E^{-15}	2.36	2.83	5.0
D2	Dolostone	Fine-X	1306	9.8	14.1	8.5	0.962	9.5E^{-16}	2.42	2.82	2.5
D3	Dolostone	Medium-X	409	8.9	9.4	6.3	4.454	4.4E^{-15}	2.55	2.81	7.2
D4	Dolostone	Medium-X	424	8.2	9.3	6.4	0.815	8.0E^{-16}	2.54	2.80	4.1
D5	Dolostone	Medium-X	1370	2.3	7.2	2.5	0.003	3.0E^{-18}	2.62	2.82	0.8
D6	Dolostone	Coarsely-X	263	9.2	10.4	–	0.433	4.3E^{-16}	2.39	2.67	–
D7	Dolostone	Coarsely-X	459	4.0	5.7	3.7	0.006	5.9E^{-18}	2.64	2.80	0.15
D8	Dolostone	Coarsely-X	462	3.7	5.4	3.4	0.007	6.9E^{-18}	2.65	2.81	0.25

Φ^i effective porosity for water, Φ^{max} maximum effective porosity for helium, Φ^{MIP} effective porosity by mercury injection, k_i initial permeability, ρ_b bulk density, ρ_m particle density, d_{eff} effective pore throat diameter, *X* crystalline

Fig. 5 Hydraulic properties of the investigated samples. **a** Porosity measured by different methods generally shows good agreement. Larger deviations of Φ^{max} (gray) are due to vuggy porosity and of Φ^{MIP}(black) due to heterogeneity of the sample material. **b** Relationship between porosity and permeability shows an increasing permeability with increasing effective porosity in the form of a power law, which is valid for estimating permeability for effective porosities up to 20%. **c** Permeability shows a distinct dependence on the effective pore throat size which controls the flow through the connected pore network

for two limestone samples showing larger deviations. The MIP tests analyzed much smaller sample volumes compared to the test plugs used for the WIP and HEP methods, implying that heterogeneities of the larger test plugs may not be represented in the MIP results.

The initial permeability is generally low and ranges from 0.105 to 4.574 mD $(1.0 \times 10^{-16} - 4.5 \times 10^{-15}$ m^2) for the tested limestone samples, from 0.540 to 0.746 mD $(5.3 \times 10^{-16} - 7.4 \times 10^{-16}$ m^2) for dolomitic limestone, and from 0.003 to 4.454 mD $(3.0 \times 10^{-18} - 4.4 \times 10^{-15}$ m^2) for the dolostone samples. Bohnsack et al. (2020) described a relationship between porosity and permeability that can be observed for the investigated samples in the form of power laws for different litho-classes. The permeability measured on rock samples in this study shows similar behavior for effective porosity below 20% and increases significantly with increasing effective porosity (Fig. 5b). In addition to the effective pore volume, the connectivity and size of the pores also control the permeability of a porous rock (Lucia 2007; Siratovich et al. 2014; Regnet et al. 2019). By evaluating data from MIP measurements, the sizes of effective pore throats connecting the pores in a pore network were determined and show a clear positive correlation with permeability (Fig. 5c).

Geomechanical characterization

For geomechanical characterization, each rock sample was tested by a non-destructive (ultrasonic test) and a destructive method (uniaxial compression test). As the rock samples were destroyed during the uniaxial test, the test was performed using adjacent core samples of similar depth, petrophysical properties, and lithofacies. The ultrasonic test was performed on the same samples used for hydrostatic testing. The results of the geomechanical tests are given in Table 3 and are described in more detail in Potten (2020).

The compression and shear wave velocities both show a strong negative correlation with the effective porosity (Heap et al. 2017) and an apparent dependency on the

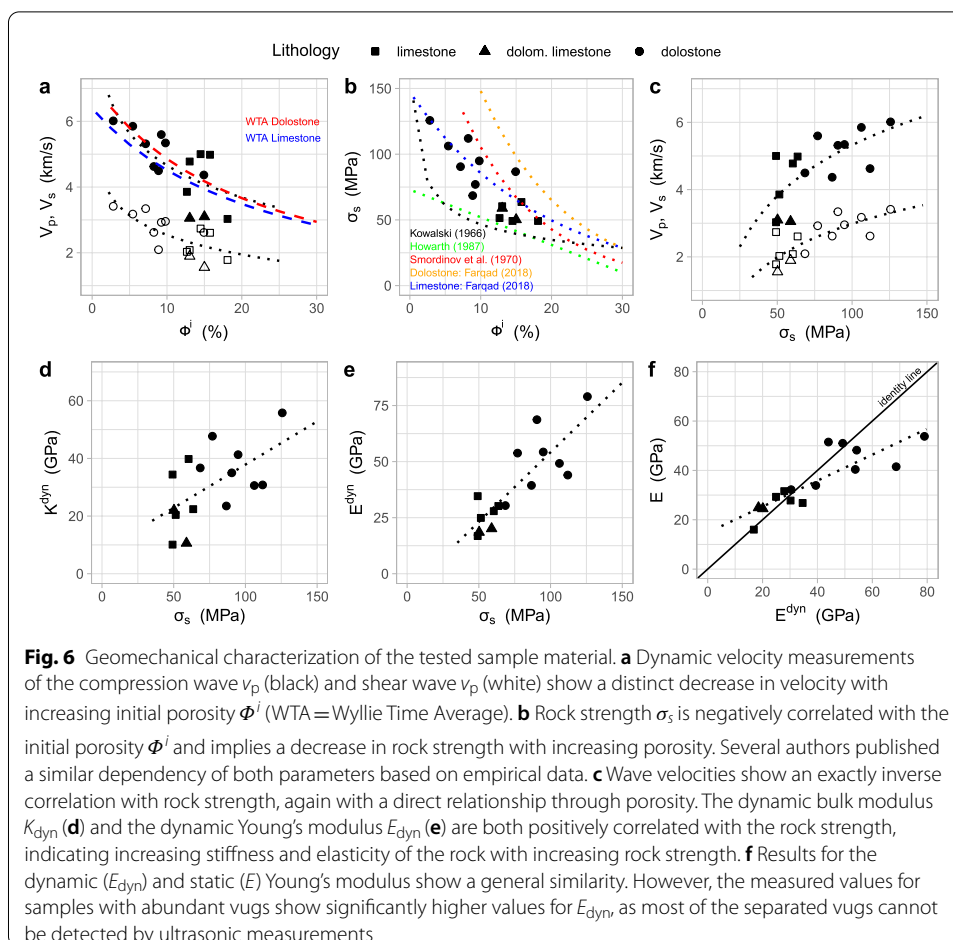**Table 3** Geomechanical characteristics of the investigated rock samples from dynamic and static tests

Sample	Lithology	Φ^{i}	v_p	v_s	σ_s	E	E^{dyn}	K^{dyn}	G^{dyn}	v^{dyn}
		%	m s^{-1}		MPa	GPa				–
L1	Limestone	13.0	4777	2083	60.4	31.6	27.9	39.8	10.1	0.38
L2	Limestone	14.5	5001	2737	49.2	26.8	34.6	34.4	17.2	0.29
L3	Limestone	18.1	3030	1780	49.4	16.0	16.8	10.1	6.9	0.22
L4	Limestone	12.7	3855	2028	51.4	29.3	24.9	20.4	20.4	0.30
L5	Limestone	15.8	4983	2608	63.6	27.8	30.2	22.4	11.8	0.28
dL1	Dol. limestone	13.0	3052	1897	58.9	24.5	20.1	10.6	8.5	0.18
dL2	Dol. limestone	15.0	3098	1556	50.2	24.9	18.5	22.0	6.8	0.36
D1	Dolostone	14.9	4367	2618	86.7	33.9	39.4	23.5	16.2	0.22
D2	Dolostone	9.8	5342	2955	94.9	48.2	54.3	41.3	21.2	0.28
D3	Dolostone	8.9	4496	2093	68.5	32.2	30.4	36.7	11.2	0.36
D4	Dolostone	8.2	4625	2620	112.0	51.5	44.0	30.8	17.4	0.26
D5	Dolostone	2.3	5317	3343	90.5	41.5	68.7	35.1	29.3	0.17
D6	Dolostone	9.2	5597	2926	77.0	40.4	53.8	47.7	20.5	0.31
D7	Dolostone	4.0	6014	3414	125.7	53.8	79.0	55.8	31.2	0.26
D8	Dolostone	3.7	5850	3177	106.2	51.0	49.2	30.6	20.0	0.23

Data for geomechanical parameters were taken from Potten (2020). Φ^{i} initial porosity, v_p compression wave, v_p shear wave, σ_s rock strength, E and E^{dyn} static and dynamic Young's modulus, K^{dyn} dynamic bulk modulus, G^{dyn} dynamic shear modulus, v^{dyn} dynamic Poisson's ratio

lithology of the tested rock samples. The compression velocities range from 3030 to 5001 m s^{-1} ($v_s = 1780–2737$ m s^{-1}) for limestone, from 3052 to 3098 m s^{-1} ($v_s = 1556–1897$ m s^{-1}) for dolomitic limestone, and from 4367 to 6014 m s^{-1} ($v_s = 2618–3414$ m s^{-1}) for dolostone. However, because of the strong coupling of velocities to the porosity of a porous material, the sonic velocity might mainly be dependent on porosity, as it generally decreases with increasing porosity (Fig. 6a) (Wyllie et al. 1965).

The uniaxial compressive strength σ_s measured in the static uniaxial compression test also confirms a direct relationship between other rock physical parameters and rock strength (Fig. 6c, d). For samples with high porosity, σ_s is significantly lower than for samples with lower porosity. The limestone samples possess a rock strength in the range of 49.2–63.6 MPa, whereas for dolomitic limestone a range of 50.2–58.9 MPa was measured and for dolostone σ_s ranges between 68.5 and 125.7 MPa (Fig. 6c). Several authors described similar relationships of decreasing rock strength with increasing porosity using empirical models fitted with distinct material constants as linear regression (Howarth 1987), exponential function (Atapour and Mortazavi 2018; Smordinov et al. 1970; Farqad 2018; Siratovich et al. 2014), as power law (Kowalski 1966) or analytical solutions to the pore-crack model of Sammis and Ashby (1986) (Zhu et al. 2010; Baud et al. 2016; Kushnir et al. 2018; Heap et al. 2019a, b). Accordingly, rock strength also shows a strong relationship to compression and shear wave velocities (e.g., Heap et al. 2014), which is due to its dependence on porosity (Fig. 6c).

The dynamic elastic parameters bulk modulus (K^{dyn}) and Young's modulus (E^{dyn}), which also decrease with increasing effective porosity (e.g., Chang et al. 2006; Heap et al. 2019a, b), show a positive correlation with σ_s (Fig. 6d, e) (Chang et al. 2006). Therefore,
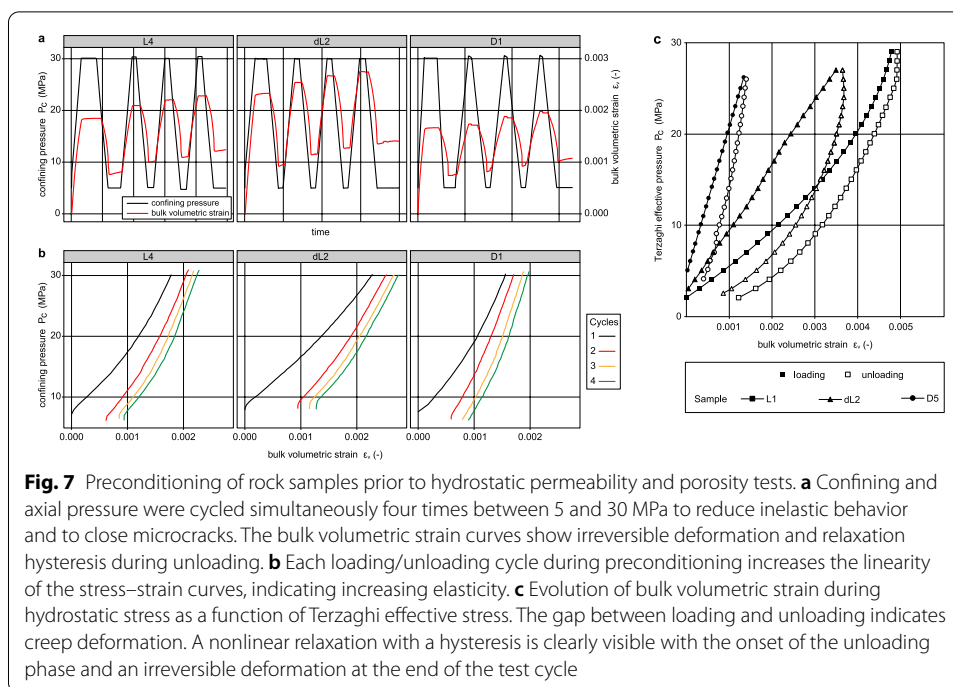
Fig. 6 Geomechanical characterization of the tested sample material. **a** Dynamic velocity measurements of the compression wave v_p (black) and shear wave v_p (white) show a distinct decrease in velocity with increasing initial porosity Φ^i (WTA = Wyllie Time Average). **b** Rock strength σ_s is negatively correlated with the initial porosity Φ^i and implies a decrease in rock strength with increasing porosity. Several authors published a similar dependency of both parameters based on empirical data. **c** Wave velocities show an exactly inverse correlation with rock strength, again with a direct relationship through porosity. The dynamic bulk modulus K_{dyn} (**d**) and the dynamic Young's modulus E_{dyn} (**e**) are both positively correlated with the rock strength, indicating increasing stiffness and elasticity of the rock with increasing rock strength. **f** Results for the dynamic (E_{dyn}) and static (E) Young's modulus show a general similarity. However, the measured values for samples with abundant vugs show significantly higher values for E_{dyn}, as most of the separated vugs cannot be detected by ultrasonic measurements

the limestone samples with higher porosity are likely to have lower stiffness and are more susceptible to deformation than the dolostone samples with lower porosity.

The static modulus of elasticity (E) was measured in a similar range as E^{dyn}, although some dolostone samples show significantly higher values for the dynamic modulus (Fig. 6f). These samples (D5, D6, D7) contain abundant separated vugs interconnected only by few interparticle pores (Lucia 2007). Since the dissolution vugs are irregularly distributed, they may not entirely be detected by the ultrasonic waves, but weaken the overall rock structure when the elasticity is tested over the whole sample volume.

Results of hydrostatic compression tests

Volumetric deformation

The application of a compressive stress to a porous solid always leads to a change in the volume of the sample to reduce the applied pressure (Jaeger et al. 2011). During a hydrostatic compression test, the sample undergoes an isotropic stress that elastically compresses the bulk volume mainly by compacting the pore space. However, due to the relaxation of the rock matrix after the rock core has been drilled out of the
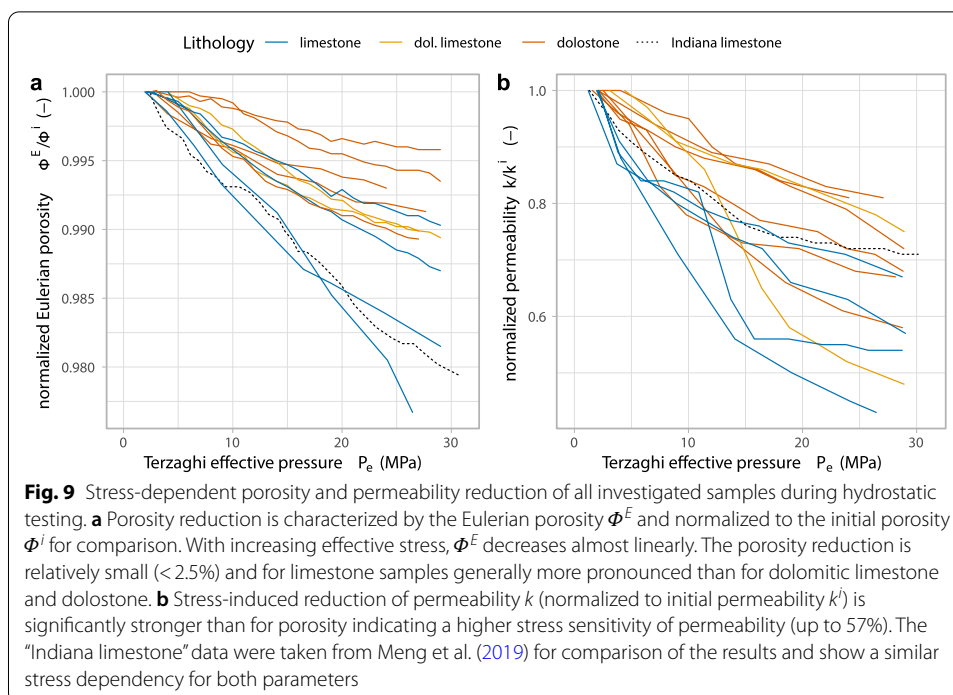
Fig. 7 Preconditioning of rock samples prior to hydrostatic permeability and porosity tests. **a** Confining and axial pressure were cycled simultaneously four times between 5 and 30 MPa to reduce inelastic behavior and to close microcracks. The bulk volumetric strain curves show irreversible deformation and relaxation hysteresis during unloading. **b** Each loading/unloading cycle during preconditioning increases the linearity of the stress–strain curves, indicating increasing elasticity. **c** Evolution of bulk volumetric strain during hydrostatic stress as a function of Terzaghi effective stress. The gap between loading and unloading indicates creep deformation. A nonlinear relaxation with a hysteresis is clearly visible with the onset of the unloading phase and an irreversible deformation at the end of the test cycle

formation, fine microcracks may have formed within the rock structure when the in-situ reservoir stress state is relieved (Holt et al. 1998). This can lead to inelastic deformation of the sample when stress is reapplied, resulting in erroneously high strains during the hydrostatic test. Each rock sample was, therefore, subjected to preconditioning to close microcracks and minimize inelastic behavior (see Sect. 3.5).

The results of this preconditioning are shown in Fig. 7 exemplarily for three samples of different lithology. Already after the first test cycle (Fig. 7a) an irreversible deformation is visible, because the sample cannot return to its initial volume after the pressure relief. Furthermore, a delay in the relaxation of the sample volume (hysteresis) after the onset of pressure relief (unloading) can be detected and a creeping deformation occurs in phases of constant pressure. Creep effects and hysteresis remain consistently noticeable even after several cycles of preconditioning. Considering the stress–strain curves of the preconditioning (Fig. 7b), a decrease in irreversible deformation with each test cycle is clearly visible, indicating an improvement of linear elasticity. However, the bulk volumetric strain monitored during all hydrostatic tests still shows hysteresis and irreversible deformation after each test cycle (Fig. 7c). Pei et al. (2018) observed an inelastic deformation during preconditioning even after 12 loading/unloading cycles before this effect disappears completely. Hassanzadegan et al. (2016) made similar observations of time-dependent deformation and interpreted this behavior as creep, inelasticity or plasticity. The growth of subcritical cracks might be responsible for this time-dependent deformation under constant stress in a brittle regime (Nicolas et al. 2017) that can be explained by a combination of enhanced plastic flow and pressure solution in carbonate

Fig. 8 Stress–strain relationships in hydrostatic compression tests. **a** Bulk volumetric strain is the response of the tested volume to compressive stress during loading. Limestones generally show higher deformation than dolomitic limestones and dolostones. **b** Drained bulk modulus K_d, calculated as the slope of the stress–strain curve at an effective pressure of 25 MPa, shows a distinct positive correlation with uniaxial rock strength. **c** With increasing porosity more pore volume can be compressed and the drained bulk modulus K_d decreases significantly due to the weakening of the rock structure

rocks (Brantut et al. 2014). Thus, to a certain extent, irreversible deformation still takes place during hydrostatic testing.

The stress–strain curves of the drained hydrostatic compression tests for all investigated samples are shown in Fig. 8a. The results show the deformation during the loading path of the tests and indicate a dependency of the degree of deformation on the lithology of the tested rock. The limestone samples show a stronger response of the bulk volume to increasing stresses than dolomitic limestones or dolostones. Based on this observation, a direct correlation between the deformation and the degree of dolomitization could be obvious. However, since compression most likely depends on the stiffness of the rock matrix and the compressible pore volume of a porous body, the deformation rate must be first correlated with the rock strength σ_s and the initial porosity Φ^i. This correlation can be shown most clearly by the drained bulk modulus K_d, which can be derived from the slope of the stress–strain curve and indicates the deformation rate of the bulk volume with increasing stress. K_d shows a strong positive correlation with σ_s, indicating a decreasing compressibility of the rock volume with increasing strength (Fig. 8b). Hence, stiffness (resistance to deformation) increases with increasing rock strength. In contrast,

Fig. 9 Stress-dependent porosity and permeability reduction of all investigated samples during hydrostatic testing. **a** Porosity reduction is characterized by the Eulerian porosity Φ^E and normalized to the initial porosity Φ^i for comparison. With increasing effective stress, Φ^E decreases almost linearly. The porosity reduction is relatively small (< 2.5%) and for limestone samples generally more pronounced than for dolomitic limestone and dolostone. **b** Stress-induced reduction of permeability k (normalized to initial permeability k^i) is significantly stronger than for porosity indicating a higher stress sensitivity of permeability (up to 57%). The "Indiana limestone" data were taken from Meng et al. (2019) for comparison of the results and show a similar stress dependency for both parameters

the deformability of a porous body correlates inversely with increasing initial porosity and the drained bulk modulus consequently decreases (Fig. 8c).

Stress-induced porosity change

To investigate the stress dependency of porosity, several rock samples of different lithofacies were tested using a drained hydrostatic test setup (see Sect. 3.5). The effective pore volume at maximum effective pressure was reduced between 0.7% for dolostone to 2.1% for limestone. To compare the evolution of Eulerian porosity Φ^E with increasing effective stress for all tested samples, Φ^E was normalized by $\frac{\Phi^E}{\Phi^i}$ to the initial porosity Φ^i. Figure 9a shows a more or less linear decrease in pore volume with increasing effective pressure for each investigated sample. However, the slope of this relationship

seems to depend on the type of lithology or the primary petrophysical rock parameters. The limestone samples investigated in this study show a more distinct reduction in porosity than samples of dolomitic limestone or dolostone. These samples show a decrease in effective porosity between 1.0 and 2.1% (relative, $\Delta\Phi_{rel}$), which corresponds to an absolute decrease of 0.16–0.31% p.u. (porosity units, $\Delta\Phi_{abs}$) depending on the initial porosity. The effect of porosity reduction seems to decrease with increasing dolomitization of the carbonate samples. Dolomitic limestone samples show a $\Delta\Phi_{rel}$ of ~ 1% and $\Delta\Phi_{abs}$ of 0.13–0.15% p.u., while the least reduction was observed in dolostone samples with $\Delta\Phi_{rel}$ of 0.7–0.95% and $\Delta\Phi_{abs}$ of 0.02–0.1% p.u. To compare the experimental results of this study with the observations of other authors, the data from hydrostatic tests on an "Indiana limestone" sample published by Meng et al. (2019) are integrated in Fig. 9a. The "Indiana limestone" is a bioclastic oolitic grainstone with a similar pore structure to the samples L1/L2 investigated in this study and also shows a relatively

Bohnsack *et al. Geotherm Energy* (2021) 9:15

Page 30 of 59

Table 4 Poroelastic parameters resulting from drained hydrostatic tests at an effective pressure of 25 MPa

Sample	Lithology	$\Delta\Phi_{rel}$	$\Delta\Phi_{abs}$	Δk_{rel}	Δk_{abs}		k_{rec}
		%	% p.u	%	mD	m²	%
L1	Limestone	1.41	0.18	43.2	1.975	1.9E^{-15}	94.27
L2	Limestone	2.13	0.31	56.7	2.128	2.1E^{-15}	–
L3	Limestone	1.15	0.21	46.4	2.054	2.0E^{-15}	–
L4	Limestone	1.24	0.16	33.0	0.053	5.2E^{-17}	79.08
L5	Limestone	1.00	0.16	Test failed			–
dL1	Dol. limestone	0.96	0.13	27.7	0.207	2.0E^{-16}	86.26
dL2	Dol. limestone	0.98	0.15	52.3	0.282	2.8E^{-16}	84.90
D1	Dolostone	0.70	0.10	28.3	0.365	3.6E^{-16}	90.89
D2	Dolostone	0.95	0.09	24.2	0.233	2.3E^{-16}	77.83
D3	Dolostone	0.72	0.06	17.3	0.771	7.6E^{-16}	83.19
D4	Dolostone	Test failed		19.3	0.157	1.5E^{-16}	
D5	Dolostone	0.87	0.02	38.8	0.001	9.9E^{-19}	–
D6	Dolostone	0.72	0.07	32.5	0.141	1.4E^{-16}	–

$\Delta\Phi_{rel}$ relative porosity reduction, $\Delta\Phi_{abs}$ absolute porosity reduction, Δk_{rel} relative permeability reduction, Δk_{abs} absolute permeability reduction, k_{rec} permeability recovery

similar stress–porosity ratio ($\Delta\Phi_{rel} \sim 2\%$, $\Delta\Phi_{abs} = 0.32\%$ p.u.). The data for each sample examined are listed in Table 4.

The individual stress–porosity paths are illustrated in Fig. 10a and show the evolution of the absolute porosity variation for each tested sample. The decrease in porosity during the loading phase is best described by an exponential relationship with increasing Terzaghi effective pressure ($R^2 = 0.94–0.99$). This exponential relationship was described earlier by David et al. (1994) and relates the compaction-induced porosity to the effective stress in dependence on the stress sensitivity coefficient of the porosity c (30). The porosity coefficient c was calculated individually for every sample and range from 1.82 to 9.71 (10^{-4} MPa^{-1}), with higher values indicating a stronger reduction in porosity with increasing effective stress. The coefficient is dependent on specific rock characteristics and decreases with increasing dolomitization from limestone to dolomitic limestone and dolostone. The dependency of the stress coefficient on various rock parameters will be discussed in Sect. 5.1.

The unloading path of the increasing/decreasing pressure cycle is also illustrated in Fig. 10a. Before the effective pressure was reduced, the pressure was kept constant to investigate the deformation of the sample and its effect on porosity due to creep. The effect of deformation at constant pressure is represented by a gap between the loading and unloading path and describes a progressive reduction of the effective porosity during this holding phase. With the onset of the unloading phase, the reduction of the effective pressure results in a dilatation of the pore volume and an increase of the effective porosity. However, the stress–porosity dilatation path appears to be time-dependent and lags behind the deformation during the loading path (hysteresis). A logarithmic model shows the best fit for the unloading path ($R^2 = 0.98–0.99$). At the end of the test cycle, after the effective pressure has been reduced to the initial pressure conditions, the effective porosity of some of the
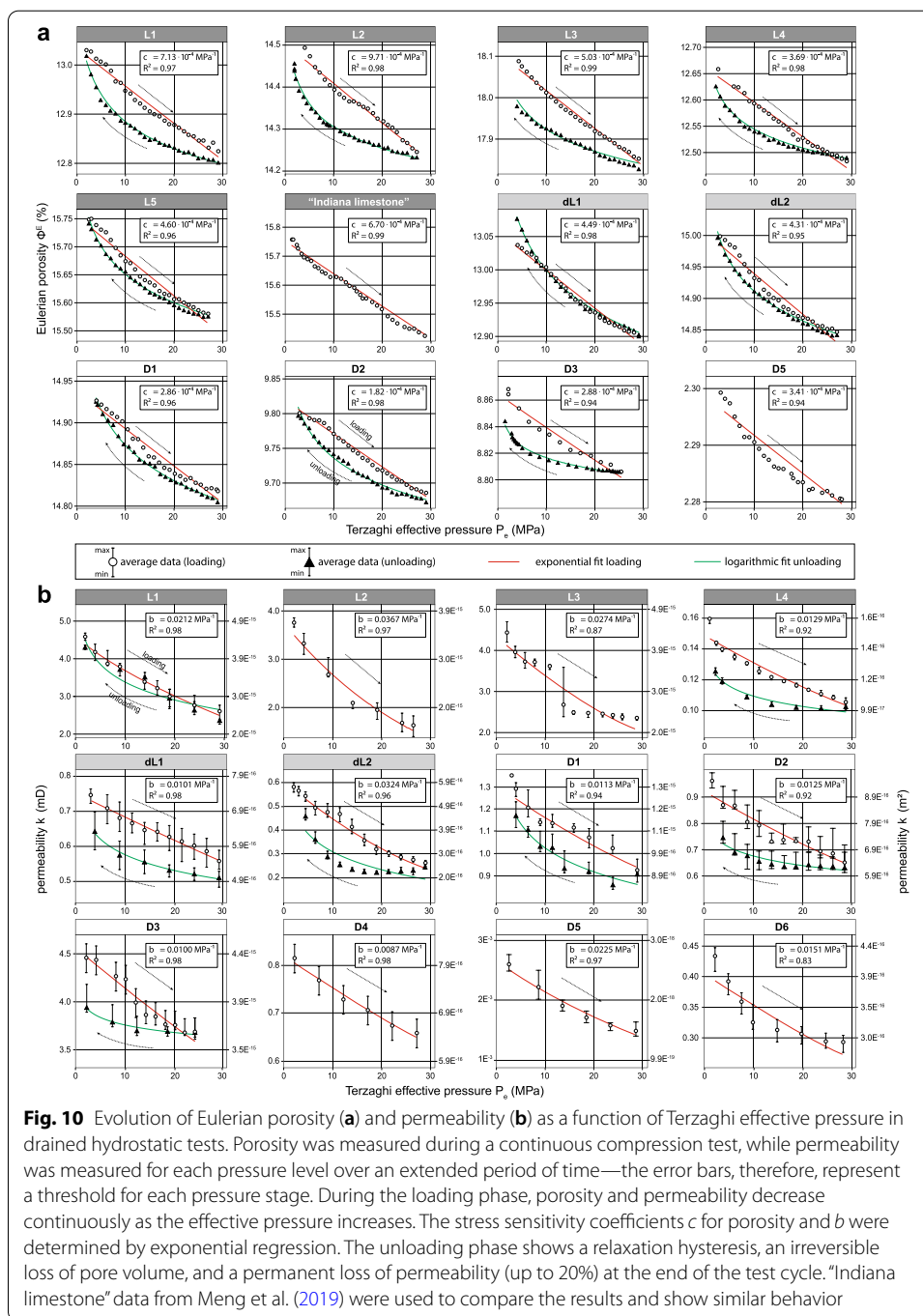
Fig. 10 Evolution of Eulerian porosity (**a**) and permeability (**b**) as a function of Terzaghi effective pressure in drained hydrostatic tests. Porosity was measured during a continuous compression test, while permeability was measured for each pressure level over an extended period of time—the error bars, therefore, represent a threshold for each pressure stage. During the loading phase, porosity and permeability decrease continuously as the effective pressure increases. The stress sensitivity coefficients *c* for porosity and *b* were determined by exponential regression. The unloading phase shows a relaxation hysteresis, an irreversible loss of pore volume, and a permanent loss of permeability (up to 20%) at the end of the test cycle. "Indiana limestone" data from Meng et al. (2019) were used to compare the results and show similar behavior

tested samples shows a distinct irreversible reduction (L2–L4, D3). This irreversible reduction indicates a permanent loss of pore volume, possibly due to the collapse of pore structures or the constriction of pore throats that control parts of the effective pore network. The tested limestone samples showed a higher affinity to permanent pore volume loss than dolomitic limestone and dolostones, which usually fully recovered their initial pore volume. Moreover, hysteresis during the recovery phase

is less pronounced in dolostones compared to (dolomitic) limestones due to the higher elasticity of these rocks. On the contrary, the effective porosity of sample dL1 after the test cycle exceeds the initial porosity. The effective pore network was possibly improved by coupling with new pathways, which could be connected, e.g., by the enlargement of narrow pore throats or the formation of pervious microcracks.

Stress-induced permeability change

The dependence of permeability on effective stress was measured in drained hydrostatic tests with stepwise variation of pressure conditions at constant flow rate and fixed hydraulic head (see Sect. 3.5). Permeability was calculated relative to the deformed sample after achieving stationary flow for each pressure step over a period of 4 h in time steps of 5 min. To compare the permeability data for each sample, the permeability k was normalized by $\frac{k}{k^i}$ to the initial permeability k^i. Figure 9b shows the stress dependent permeability reduction in the form of stress–permeability paths. The permeability shows a significant decrease with increasing effective pressure for each of the samples. The decrease is more pronounced in the first pressure steps at relatively low effective pressure and diminishes with increasing pressure. In contrast to porosity, pressure-dependent permeability does not show such a clear correlation with the lithology of the rock sample. The permeability of limestone samples tends to be more sensitive to stress than that of some dolostone samples. However, other processes may be of importance in controlling the degree of permeability reduction and are not purely related to the lithological character. The relative permeability reduction Δk_{rel} at maximum effective stress for limestone ranges from 33.0 to 56.7%, corresponding to an absolute permeability reduction Δk_{abs} between 0.053 and 2.128 mD ($5.2 \times 10^{-17} - 2.1 \times 10^{-15}$ m^2). For dolomitic limestone Δk_{rel} was measured between 27.7 and 52.3% ($\Delta k_{abs} = 0.207-0.282$ mD, $2.0 \times 10^{-16} - 2.8 \times 10^{-16}$ m^2) and for dolostone Δk_{rel} varied between 17.3 and 38.8% ($\Delta k_{abs} = 0.771-0.001$ mD, $7.6 \times 10^{-16} - 9.9 \times 10^{-19}$ m^2). The individual data for the tested samples are shown in Table 4, and the dependence of the stress coefficient on distinct rock parameters will be discussed in Sect. 5.1.

Figure 10b shows the individual measurements of the absolute permeability reduction for each tested sample as a function of the loading and unloading of the effective pressure. The unloading phase is missing for some of the samples due to technical issues with the hydraulic pumps or due to the failure of the sample sleeve during the holding phase at maximum effective pressure. The error bars indicate the permeability range measured over the entire interval of the corresponding pressure level after a stationary flow has been reached. As with effective porosity, the stress–permeability relationship can best be described by an exponential model, although some data points are more scattered within the measured permeability range ($R^2 = 0.83-0.98$). This observation is consistent with Cheng (2016) and David et al. (1994), who reported an exponential relationship between effective stress and compaction-induced permeability, based on the stress sensitivity coefficient for permeability b (32). The coefficient was determined for each sample and can be used for the characterization of stress sensitivity for different rock types, indicating a stronger stress dependence with an increase of the coefficient. The stress–permeability curves for limestone samples yielded a coefficient b of 0.0129–0.0367 MPa^{-1},

while b for dolomitic limestone ranges from 0.0101 to 0.0324 MPa^{-1} and from 0.0087 to 0.0225 MPa^{-1} for dolostone.

While the exponential trend fits well for most samples, samples L3 and D6 do not entirely coincide with this trend over the entire pressure range. Both samples show a strong decrease in permeability in the low effective pressure range and a sudden change to a more linear trend continuing with a slow decrease towards the higher effective pressure ranges. This abrupt trend change most likely indicates isolation of parts of the preferential flow network by occlusion of the controlling pore throats (e.g., by irregular compaction or collapse of the pore structure) (Xu et al. 2018; Teklu et al. 2018; Dautriat et al. 2011).

The unloading path of the effective stress shows a delayed (hysteresis) recovery of permeability. The best fit for the recovery was found to be in the form of a logarithmic function. At the end of the entire test cycle, permeability has mostly not fully recovered and shows an irreversible permeability loss (10–20%). Some pore throats or cracks that were effective for the flow through the porous network seem to have been irreversibly deformed or closed during compression and are no longer accessible for percolation through the rock sample (Dautriat et al. 2011; Teklu et al. 2018).

Discussion

Dependency of stress sensitivity on different rock properties

The results of the hydrostatic tests show a significant relationship between the effective stress and the change in bulk volume, porosity, and permeability of a porous body. However, this dependency varies for each parameter and sample and is dependent on different rock characteristics. Essentially, the stress sensitivity coefficients of permeability (b, S_s^k) and effective porosity (c, S_s^{Φ}) represent material constants that can be used to describe the stress dependency of different rock types as a function

Table 5 Effective stress sensitivity coefficients of the tested rock samples at an effective pressure of 28 MPa

Sample	Lithology	S_s^{Φ} 10^{-2} MPa^{-1}	S_s^k MPa^{-1}	$c(C_{\Phi})$ 10^{-4} MPa^{-1}	b 10^{-2} MPa^{-1}	β –
L1	Limestone	0.43	0.16	7.13	2.12	28.3
L2	Limestone	0.66	0.23	9.71	3.67	34.0
L3	Limestone	0.51	0.18	5.03	2.74	46.3
L4	Limestone	0.42	0.13	3.69	1.29	34.2
L5	Limestone	0.34	–	4.60	–	–
dL1	Dol. limestone	0.41	0.11	4.49	1.01	22.6
dL2	Dol. limestone	0.36	0.29	4.31	3.24	74.7
D1	Dolostone	0.30	0.13	2.86	1.13	36.1
D2	Dolostone	0.35	0.07	1.82	1.25	56.7
D3	Dolostone	0.22	0.06	2.88	1.00	32.8
D4	Dolostone	–	0.06	–	0.87	–
D5	Dolostone	0.32	0.24	3.41	2.25	63.0
D6	Dolostone	–	0.11	–	1.51	–

S_s^{Φ} stress sensitivity coefficient for porosity, S_s^k stress sensitivity coefficient for permeability, c porosity stress coefficient (equals pore compressibility C_{Φ}), b permeability stress coefficient, β porosity sensitivity exponent

Fig. 11 Correlation of stress sensitivity coefficients with characteristic rock parameters. **a** Stress sensitivity coefficient for porosity *c* decreases with increasing rock strength σ_s. Samples with higher initial porosity Φ^i are mostly more stress sensitive than those with lower Φ^i. **b** Correlation between the stress sensitivity coefficient for permeability *b* also indicates a decreasing sensitivity with increasing σ_s, but is fuzzier than for porosity. Most samples with low initial porosity Φ^i also shows a low stress sensitivity of permeability. **c** Relationship of *c* with the drained bulk modulus K_d indicates a decreasing stress sensitivity with decreasing compressibility of the porous medium. **d** Stress sensitivity of permeability increases with increasing stress sensitivity of porosity. High values for *b* compared to *c* indicate a decoupling of the permeability dependence from the porosity and an increasing contribution of cracks or fractures to the flow network

of effective pressure. Higher coefficients indicate a stronger sensitivity of porosity/permeability to effective stress than lower coefficients. The coefficients resulting from the data of this study (Fig. 10) are in agreement with this concept and are listed in Table 5. In principle, both the exponential effective stress law (30)–(32) and the logarithmic method (33) of Jones and Owens (1980) can be used to establish a reliable relationship between effective pressure and porosity/permeability, with the former method being more straightforward.

To evaluate the stress sensitivity in relation to distinct rock parameters, the sensitivity of porosity and permeability was correlated with specific rock characteristics such as rock strength, initial porosity, and the drained bulk modulus. Both the sensitivity coefficients of porosity *c* and of permeability *b* show a negative correlation with the peak rock strength σ_s (Fig. 11a, b) indicating a strong dependency on the rigidity or deformability of the rock volume. A negative correlation between the stress sensitivity of porosity with the drained bulk modulus emphasizes the correlation of stress sensitivity with the volumetric deformation of the sample (Fig. 11c), which can mainly be explained

by a superimposed relationship between pore volume and compressibility of a porous medium (Figs. 6, 8). Thus, the stress sensitivity of porosity is directly related to the amount of accessible pore volume itself and is more pronounced for samples with higher initial porosity (samples L1–L3, dL1, and dL2). For permeability, the dependency on initial pore volume is of secondary importance, since the development of the pore geometry and the interconnection through pore throats have a greater influence on the flow behavior (Lucia 2007). Penny-shaped pores with a low aspect ratio and crack-like pores can significantly reduce permeability if preferred flow paths are closed by compression, which might be independent of the total pore volume (Hassanzadegan et al. 2016). These pore types were observed in the samples dL2 and D5 as channel pores along microfractures, both showing a relatively high stress sensitivity of permeability (Figs. 16, 18).

Sensitivity of permeability to stress-induced changes of the pore space

The stress sensitivity of permeability is mainly dependent on the type and size of pores and pore throats as well as the presence of fracture like pores or cracks (low aspect ratio pores). The proportion of permeability reduction independent of stress-induced porosity changes can be expressed by the porosity sensitivity exponent β of the power law (31) described by David et al. (1994). The exponent reflects the impact of the induced porosity reduction on permeability and depends only on the connectivity and type of pore network. The same relationship can be estimated by the ratio of the two stress sensitivity coefficients for permeability and porosity $\beta \cong \frac{b}{c}$ (Fig. 11d). High values for b compared to c indicate a decoupling of permeability dependence from porosity and an increasing contribution of cracks or fractures to the flow network.

Compared to β values reported by other authors, 4.6–25.4 (David et al. 1994) and 0.9–105 (Xu et al. 2018) for some sandstone, 1.2–1.8 for silty shale (Dong et al. 2010), and < 8 for Purbeck limestone and ~ 15 for "Indiana limestone" (Meng et al. 2019), the values found in this study are relatively high, ranging between 22.6 and 74.7 (Table 5). With increasing β, permeability becomes progressively independent of the contribution of "regular" pores to the effective flow network and is increasingly controlled by fracture pores or cracks and fissures. Well-sorted sandstones contain a well-connected and permeable network of circular pores in which connectivity is controlled by several pore throats that are resilient to effective stress. The reduction in permeability will, therefore, depend on the effective pore volume rather than on a few individual elongated or penny-shaped pores or cracks, and β will, therefore, tend to be low compared to the carbonate rocks investigated in this study.

Fracture like pores were observed in the thin sections of samples dL2 and D5 (Figs. 16, 18) and both samples show the highest values of $\beta = 74.7$ and $\beta = 63.0$. Both samples also show one of the highest stress sensitivities of permeability due to an increasing compression of the preferred flow paths along the fracture structures. In contrast, samples L1, L2, L4, dL1, D1, and D3 show relatively moderate values for porosity sensitivity ($\beta < 40$) and among the lowest stress sensitivity for permeability. The pore network of these samples is predominantly composed of interparticle or intercrystalline pores with a relatively high aspect ratio pores (Figs. 16, 18), which are more resistant to stress. The remaining samples L3, D2, and D7 have moderate to high values for β with a moderate to relatively low stress sensitivity of permeability. No direct evidence of the contribution

Fig. 12 a Relationship between stress sensitivity coefficients and the porosity sensitivity coefficient β. The stress sensitivity coefficients S_s^Φ for porosity and S_s^k for permeability are compared with a set of data from different authors. While S_s^Φ shows no significant correlation with β, S_s^k is clearly increasing with increasing β. Higher values of β indicate a progressively increasing contribution of fracture pores and micro-fractures to the effective permeability network and result in higher S_s^k values. Data for sandstone are taken from Xu et al. (2018) and for limestone compiled from Meng et al. (2019), Teklu et al. (2018), and Dautriat et al. (2011). **b** Porosity sensitivity is related to the effective pore throat size controlling the flow through the pore network. The exponent β increases with decreasing pore throat size, which indicates a decoupling of the stress sensitivity from porosity and permeability

of micro-fractures could be observed in the thin sections (Figs. 16, 18). However, all three samples show a kind of clogging of the pore throats by sparry calcite cement (L3), bituminous remnants (D2) or growth of burial dolomite (D7), which causes a narrowing of the pore throats and can lead to a loss of permeability if particular flow paths are clogged.

Xu et al. (2018) describe a clear relationship between β and the initial porosity and permeability for sandstone. Samples with lower porosity and permeability show higher β values, indicating that the flow network is dominated by micro-fractures and fracture pores. This assumption could not entirely be validated for the carbonate samples tested in this study, as the distribution and types of pores as well as the geometry of flow paths are more complex in these heterogeneous deposits. However, a general trend towards higher β values with decreasing initial porosity and permeability was observed for some of the carbonate samples. Furthermore, Xu et al. (2018) found a proportional relationship between β and the stress sensitivity of permeability. A similar relationship was observed for the carbonate samples in this study, indicating a linear increase in stress sensitivity with increasing contribution of fracture-like patterns to the flow network. Figure 12a shows the increase in the stress sensitivity of permeability S_s^k with increasing β, while the stress sensitivity of porosity S_s^Φ remains more or less constant. In addition, β is dependent on the effective pore throat size measured by the MIP tests, as it increases

significantly with decreasing throat diameter, Fig. 12b. The main cause of permeability loss is thus considered here to be the closure of penny-shaped and fracture pores with a low aspect ratio, micro-fractures, and small sized effective pore throats (Benson et al. 2006; Xu et al. 2018; Hassanzadegan et al. 2016; Cant et al. 2018).

Consequently, the relative high values of β for the tested Malm carbonates may most likely indicate that the effective pore network is mainly connected by narrow pore throats and/or crack-like structures. Compaction of these flow paths can lead to a rather strong loss of permeability, while compression of the pore space is only slight to moderate.

Dependencies of different rock types of the Malm aquifer

To estimate the effects of changes in effective stress on an entire reservoir, the basic principles of stress sensitivity must be simplified to require as little information as possible about the aquifer rocks. Often knowledge of the petrophysical or geomechanical parameters within the local reservoir is limited to a lithological subdivision of the reservoir and data from geophysical logs are lacking or very scarce.

Fig. 13 Normalized stress sensitivity for different lithology and facies types. **a** Average permeability reduction of the tested Malm samples fits well within the range of reference data reported by various authors. The lower limit is defined by rock types with a well-connected flow network, while the upper limit is represented by rock types with a poorly developed flow-network dominated by compliant micro-cracks and elongated pores. **b** Results for the stress-induced porosity reduction show a discrepancy with most data from the literature and are relatively low for the Malm carbonates. Differences in the test procedure can have a significant impact on the results. See text and Fig. 14 for more details

Fig. 14 Normalized porosity (**a**) and permeability (**b**) as a function of Terzaghi effective pressure for different lithologies. The compaction-induced stress sensitivity decreases with increasing dolomitization. The stress sensitivity coefficients *c* and *b* were found by best exponential fitting for each group and used as input for the effective stress models. The error bars represent the minimum and maximum values of the measured samples within the specific group—the data points are average values

Therefore, it seems reasonable to estimate stress sensitivity based on the different lithological units distributed within the Malm aquifer, which can be distinguished with a group-specific stress sensitivity coefficient, determined in this study.

In Fig. 13a, the results of the Malm carbonates, averaged for each rock type, show a good agreement between the maxima and minima of the range observed by different authors (Bakhtiari et al. 2011; Dautriat et al. 2011; Hassanzadegan 2013; Moosavi et al. 2014; Teklu et al. 2018; Meng et al. 2019; Shi et al. 2019). Some of the (dolomitic) limestone samples tend to have a high stress sensitivity of permeability and might be controlled by crack-like pores and microcracks (double-porous medium), while others exhibit a well-connected flow network that is more persistent to compressive stress (see Fig. 14 for detailed ranges). The permeability of dolostone is on average less sensitive to stress. Idiotopic dolostone with well-developed intercrystalline pores contains plenty of well-connected pores and is similar to porous sandstone, which is less affected by permeability reduction. On the contrary, the lower limit of the tested dolostones show a rather hypidio- to xenotopic fabric with mostly separated vugs or tiny intercrystalline pores, which are only sparsely connected by narrow pore throats and are, therefore, more sensitive to stress.

The stress sensitivity of porosity, in contrast, appears to be rather low for the Malm carbonate samples compared to reference data from the literature (Fig. 13b). This

discrepancy may very well originate from differences in the test setup and measurement procedures. To assure the elastic behavior of the tested porous medium and to close artificially formed cracks and fissures, a preconditioning of the sample has to be carried out before advancing with further tests (see Sect. 3.5). This preconditioning was reportedly only performed by Hassanzadegan (2013) and Blöcher et al. (2014) prior to the porosity stress sensitivity test. Furthermore, it is relevant whether the stress-induced change in porosity is related to Eulerian or Lagrangian porosity. Nevertheless, the results of Meng et al. (2019) of the oolitic "Indiana limestone" are within the range of the limestone samples from this study (see Fig. 14 for detailed ranges).

Several authors observed a high variance of the stress sensitivity for different rock types (Fig. 13), even for rocks of similar lithology (Moosavi et al. 2014; Blöcher et al. 2014; Pei et al. 2014; Meng et al. 2019; Bakhtiari et al. 2011; Hassanzadegan 2013; Shi et al. 2019; Ghabezloo et al. 2009a; Teklu et al. 2018; Dautriat et al. 2011). Considering the facies of the individual rock types, a general decrease in sensitivity to well-connected pore networks becomes apparent. Rock types with poor connectivity (separated vugs), very narrow pores (mudstone and xenotopic dolostone), and pores closed by recrystallization (crystalline) show a significantly higher sensitivity (Fig. 13a). Here, flow is presumably controlled by micro-fractures or elongated pores, which are very compliant and, therefore, prone to high permeability losses even at relatively low effective pressures. In contrast, rock types that form a well-connected porous flow network, such as sandstone, porous oolitic limestone, idiotopic dolostone, and touching-vug limestone, are less affected by permeability reduction.

Volumetric deformation

The framework built by dolomite minerals in the dolostone is more rigid and less deformable than that of the (dolomitic) limestone, which is dominated by particles of different sizes and is more compliant under compressive stress. Kushnir et al. (2015) investigated the deformation mechanisms for synthetic samples with varying calcite and dolomite content and found a significant increase in rock strength with increasing dolomite content, which supports the observations of this study. The geomechanical parameters show a distinct negative correlation with the porosity of the rock sample, which in turn is rather low for the tested dolostone samples. This geomechanical behavior is also reflected in the stress sensitivity of the different lithologies during the hydrostatic compression tests. From dolostone to limestone, the deformability increases with increasing effective stress, which results in a higher volumetric strain of the tested rock volume (Fig. 8a). The higher elasticity of dolostone also reduces the irreversible deformation of the rock volume compared to limestone with lower elasticity (Fig. 7c). Thin compliant micro-cracks are easily affected by an increase in effective stress and enhance the permanent deformation of the rock volume. The pressure sensitivity of the bulk volume also correlates negatively with the rock strength and initial porosity of the investigated samples, whereby the drained bulk modulus K_d increases or decreases with increasing rock strength or decreasing initial porosity, respectively (Fig. 8b, c).

Stress sensitivity coefficients

Based on the results of the hydrostatic tests, the loss of pore volume is higher in limestone than in dolomitic limestone or dolostones due to the higher compressibility of the rock volume (Fig. 9a). The stress sensitivity of the porosity, therefore, decreases from limestone to dolostone, as indicated by a decreasing sensitivity coefficient c (Figs. 10a, 11). This becomes clearer by comparing the normalized porosity reduction for all samples relative to their lithotype. Figure 14 shows the range of the normalized Eulerian porosity for each lithotype and a lithology specific sensitivity coefficient. The coefficient c decreases with increasing dolomitization from 5.73×10^{-4} MPa^{-1} (limestone) to 4.29×10^{-4} MPa^{-1} for dolomitic limestone and to 3.45×10^{-4} MPa^{-1} for dolostone. These coefficients can, therefore, be used as input for estimating porosity at varying effective stress for the specific lithotype of the Malm aquifer using the exponential model of Meng et al. (2019) (30). The model is corrected for the pressure conditions at initial conditions and shows good agreement with the measured data (Fig. 14).

Similar to porosity, the stress sensitivity of permeability mainly shows a tendency to be stronger for limestone than for dolostone (Fig. 14b). On average, the stress sensitivity coefficient b decreases from limestone with $b = 0.022$ MPa^{-1} to dolomitic limestone (0.018 MPa^{-1}) and dolostone (0.012 MPa^{-1}). Comparing the stress sensitivity coefficient b for all samples investigated in this study, b usually decreases from limestone to dolostone, indicating an overall stronger compliance of the porous network and its flow paths to increasing stress (Fig. 10b). The results of this study show that the sensitivity coefficient b is negatively correlated with the rock strength, similar to the coefficient for

Fig. 15 Evolution of the hydraulic, geomechanical, and poroelastic properties of the Malm aquifer rock as a result of diagenetic processes. The porosity and geometry of the pores and pore throats are altered and rearranged in the different stages of diagenesis. From early to late burial diagenesis the porosity of the investigated samples mainly decreases. The distribution of pore throat diameters (blue lines) and the connectivity of the pore network (red lines) vary throughout the different stages and control the permeability of the rock. Rock strength increases with increasing dolomitization and decreasing porosity, while the stress sensitivity of porosity is decreasing simultaneously. The stress sensitivity of permeability depends on the connectivity of the pore network and the occurrence of micro-fractures and does not show a clear trend. See text for more details. Sketches are modified after Wang et al. (2015). k^i—initial permeability, Φ^i—initial effective porosity, K_d—drained bulk modulus, σ_d—rock strength, b—stress sensitivity coefficient of permeability, c—stress sensitivity coefficient of porosity

porosity, but more scattered and less dependent on rock type (Fig. 11b). Thus, weaker rocks do not necessarily appear to be more susceptible to loss of permeability if the preferred flow paths remain unaffected by compression, as observed in sample dL1. However, rigid rocks with few restricted flow paths can also have a relatively high stress sensitivity of permeability if permeability is dependent on a few single flow paths (e.g., sample D5).

Impact of diagenesis and dolomitization on the stress sensitivity

The results of this study show a distinct dependency of the hydraulic, geomechanical, and poroelastic behavior on the porous structure of a carbonate sample. Therefore, a possible link of stress sensitivity with the diagenetic history of the carbonate rock from the Malm reservoir seems logical. The samples tested in this study were also selected with regard to the different degrees of dolomitization and diagenetic overprinting to correlate them with the stress sensitivity of the rock. The different stages of early and late diagenesis that affected the tested rock samples and their properties are summarized in Fig. 15 and discussed in the following. A detailed description of the influence of diagenesis on stress sensitivity and rock parameters for each sample can be found in Appendix 2.

The pore space is progressively altered, completely rearranged or partly reduced to a minimum by diagenetic processes (Lucia 2007). Carbonates of a primarily well-porous limestone facies might be affected even in early burial stages by selective dolomitization due to enhanced percolation of fluids. If the primary pore network is preserved, porosity remains relatively constant and might be enhanced by intercrystalline pores between the dolomite rhombs. The dissolution of rather unstable particles (e.g., aragonitic shells and cortices) results in a further enhancement of porosity (molds). However, cementation, that may already occur during early diagenesis is likely reducing the porosity and connectivity of the pore network to a certain extent. In deeper burial, the remnant calcite of the precursor limestone is completely dissolved, and a porous framework of dolomite rhombs remains. The intercrystalline pores are well connected and the porosity is usually high, but depends on the size of the dolomite rhombs. As observed in this study and already pointed out in the experimental studies by Delle Piane et al. (2009) and Kushnir et al. (2015), the strength and rigidity of a rock increases with increasing dolomite content. Thus, the increased rigidity of the mineral framework within dolostones results in a higher chance of resisting compaction by increasing effective stress and consequently preserving porosity (Lucia 2004). However, further dolomitization with pore-filling dolomite cements and overdolomitization again have a negative effect on the porosity and connectivity of the pore network (Lucia 2004). Due to the reduced compliance of the mineral framework, the porosity might be preserved, but the remaining vugs and molds are scarcely connected and the permeability is, therefore, rather low (Lucia 2007).

The deformability of the investigated Malm carbonates decreases with increasing burial diagenesis, resulting in a more rigid pore network with increasingly lower stress sensitivity. The stress sensitivity of permeability, to the contrary, depends on the connectivity of the pore network, which shows a more complex relationship to diagenesis. The sensitivity is lower if the porous network has good connectivity and stronger during the stages of cementation, that narrow or seal pores and pore throats. Additionally, structural deterioration of the rocks framework by cracks or

micro-fractures further increases the stress dependency, as they are very compliant to compressive stresses.

Implications and limitations for exploration of the geothermal Malm reservoir in the Bavarian Molasse Basin

The geomechanical and hydraulic properties of the rock mass forming the Upper Jurassic aquifer were investigated on a microscopic and macroscopic scale in this study. Due to the heterogeneity of carbonate deposits even at small scales (e.g., facies variations, varying pore types and sizes, irregular dolomitization), the intrinsic properties of carbonate rocks may be subject to some variability (e.g., Regnet et al. 2019). At the laboratory scale, this heterogeneity can be controlled by a thorough examination of the rock matrix composition and pore types, and by conducting tests on several samples of a similar rock type. However, laboratory results are representative only of the rock matrix of the intact rock mass, which describes a continuum with averaged properties that defines a representative elementary volume (REV) (Bear 1988; Konrad et al. 2019). Thus, porosity, permeability, and geomechanical data refer to the properties of the rock matrix, including all heterogeneities below the reservoir scale, such as changes in facies, particle sizes, vugs, stylobedding, and fissures in the rock samples.

The data measured in this study for the hydraulic parameters of the rock matrix show that the effective matrix porosity and permeability are rather low to represent the main source of fluid flow in the reservoir: $\Phi^i < 20\%$, $k^i < 5$ mD (5.0×10^{-15} m^2) (Table 2). This suggests that geothermal well production rates and hydraulic parameters determined from pumping tests could benefit from both the pore volume and permeability of the rock matrix and permeable karstified zones and fractures/faults that provide high hydraulic conductivity. By evaluating pumping tests, the matrix permeability of the Malm aquifer was determined to range between 1.0×10^{-17} and 1.0×10^{-12} m^2, whereas wells showing a linear flow regime benefit from fracture/fault zones with a permeability range of 1.0×10^{-14}–1.0×10^{-9} m^2 (Birner 2013; Konrad et al. 2019).

The Upper Jurassic in the Bavarian Molasse Basin represents a complex geological structure that exhibits fractures, faults, karstification, and diagenesis to a variable extent (e.g., Bachmann et al. 1987; Mraz et al. 2018; Mraz et al. 2019; Seithel et al. 2019). Baud et al. (2016) and Heap et al. (2018) studied the geomechanical and hydraulic properties of stylolite-bearing limestone and concluded that the presence of stylolites, whether of tectonic or sedimentary origin, can significantly reduce the strength and permeability of the investigated rock. Local clusters of stylolites are common throughout the Malm aquifer and, depending on their orientation, rock strength and permeability must be assumed to be negatively affected on laboratory scale. Thus, the stress sensitivity coefficients determined in this study are probably not representative for these areas of the aquifer, as the effect of stylolites has to be investigated and implemented first.

Hence, depending on the scale of observation, large uncertainties in the prediction of the mechanical and hydraulic behavior of the reservoir are to be expected. Without considering these superordinate properties of a carbonate reservoir, the defined REV cannot be assumed to be representative at the reservoir and basin scale and must be up-scaled accordingly. Up-scaling of hydraulic parameters (porosity and permeability) and geomechanical behavior (rock strength, compressibility, stress sensitivity) can be

very challenging in carbonate reservoirs due to depositional and diagenetic heterogeneity (Menke et al. 2021). While large-scale karst and fault structures can be spatially interpreted from geophysical data (seismic surveys, downhole logging), small-scale heterogeneities are almost unresolvable (Egert et al. 2018). However, by defining common parameter ranges for different rock and facies types of the Malm carbonates by laboratory tests, as done in this study and in the studies of Bohnsack et al. (2020) and Potten (2020), heterogeneity can be controlled even in a coarser modeling grid of numerical simulations (e.g., THM models) by up-scaling these value ranges for different lithologies (Settari et al. 2013). The acquisition of various rock parameters at laboratory scale can, therefore, help to predict the thermal–hydraulic–mechanical behavior of the reservoir and reduce the exploratory and economic risk of new geothermal projects in the Bavarian Molasse Basin by closing the gap between rock core data and reservoir scale.

Conclusion

During changes in the effective stress within a reservoir the aquifer rock exhibits a characteristic poroelastic response due to changes in pore pressure (drawdown, injection, temperature change). The results of the hydrostatic compression tests performed in this study show a strong dependence of the stress sensitivity of the bulk volume, porosity, and permeability on distinct rock properties.

In relation to the rock types occurring throughout the Malm reservoir, the stress sensitivity of both porosity and permeability decreases with increasing dolomitization. The rigidity of the matrix framework increases with increasing dolomite content, which strengthens the rock structure and reduces the compaction of pores and pore throats. However, the mechanisms of stress sensitivity are more complex and are not simply controlled by the lithology of a rock, but rather by the connectivity and geometry of the pores and pore throats. Moreover, the structure of the pore network and the shape of the individual pores and pore throats is controlled by more than just the primary deposited rock type and facies. During diagenesis, the pore space can be drastically altered or reshaped. With increasing burial, the pores and pore throats can enlarge by dissolution or be reduced or even closed by cementation or overdolomitization.

A general trend of decreasing rock compressibility with increasing rock strength was observed for the carbonate samples stemming from the Malm aquifer. The stress sensitivity of porosity decreases from early to late diagenetic overprinting, while the sensitivity of permeability varies as a function of the evolution of pore network connectivity. A well connected porous network is less affected by compressive stress than a poorly connected network with rather limited flow paths. Narrow pore throats with a low aspect ratio, cracks, and micro-fractures are very compliant and can be easily closed even at low effective stress. Therefore, disconnecting important flow paths from the effective flow network can lead to a drastic reduction in permeability. The pore volume is, therefore, of secondary importance for the stress sensitivity of the permeability. It rather depends on the connectivity through micro-fractures and fracture pores, which are closed first in response to increasing effective stress, followed by the pore throats and finally the pores themselves. However, permeability shows a strong sensitivity to porosity when the porous network is well connected and the reduction in pore volume exceeds the constriction of flow paths.

The average sensitivity coefficients for limestone, dolomitic limestone, and dolostone established in this study for the Malm reservoir can be used for the estimation of the stress sensitivity of reservoir rocks. In general, zones of higher rock strength in the Malm reservoir are less susceptible to stress-induced changes in hydraulic properties, unless controlled by, for example, penny-shaped pores or cracks. These zones (Malm Zeta 1–2, Malm Delta and Epsilon) mainly consist of low-porosity and dense limestones or well-cemented dolostones with poor hydraulic properties, which may contribute only marginally to the productivity of a well. In contrast, the well-known flow zones in the upper part of the Malm reservoir (within Malm Zeta 4–5 and Malm Zeta 3) are largely characterized by less rigid, porous limestones that are likely to be more sensitive to stress changes and whose hydraulic properties could deteriorate significantly.

Appendix 1

Detailed description of rock type and facies
Limestone
Samples L1/L2
Fossiliferous grainstone composed of abundant peloids (P), oncoids and lithoclasts (M) with micritic envelopes, fragments of the dasyclad green algae *Campbelliella "Bankia" Striata* (Carozzi) (B) and *Clypeina Jurassica* (Favre) (C), and mollusks (gastropods, G) (Fig. 16). Both samples are very porous ($\Phi^i = 13.0$–14.5%) and dominated by mesoporous interparticle pores between components and micropores within the micritic peloids and micritic envelopes of most particles. Oversized solution pores (vugs) up to 1 mm in size may occur but are rare. Pore sizes range from < 0.4 μm as micritic microporosity to a maximum of 1 mm for the rare vugs. Most of the dominating interparticle pores have sizes between 100 and 200 μm. For both samples the capillary pressure curves show a skewed and tailed distribution with a distinct peak at the highest frequency of occurring pore throat sizes (Fig. 17). The MIP curve of sample L2 shows pore throats with diameters of mainly 10–20 μm connecting the interparticle pores. The long tail with decreasing throat size of 10–0.01 μm indicates that the pore throats are increasingly constricted by thin isopachous microcrystalline calcite cement and represent micro-throats in micritic envelopes and peloids. The permeability measured for sample L1 is $k^i = 3.754$ mD (3.7×10^{-15} m^2).

Albeit both samples are very similar in their facies and pore inventory, the peak for sample L1 is in the range of micro-throats with positive skew and the peak for sample L2 is in the range of macro- to mega-throats with negative skew. Compared to the microphotograph of sample L1, the distribution of the pore throat sizes from the MIP examination is rather doubtful, since pore throats with a size of up to 10 μm are clearly visible between the interparticle pores. Furthermore, the measured permeability of $k^i = 4.574$ mD (4.5×10^{-15} m^2) and the relatively high effective porosity of $\Phi^i = 13.0\%$ support a rather interconnected pore network. Moreover, the effective porosity of

Fig. 16 Thin sections of the tested limestone and dolomitic limestone samples. The samples were impregnated by blue-dye resin to visualize the pore space and partially stained by Alizarin-S for identification of calcite minerals. See text for detailed description of the thin sections and the classification of porosity
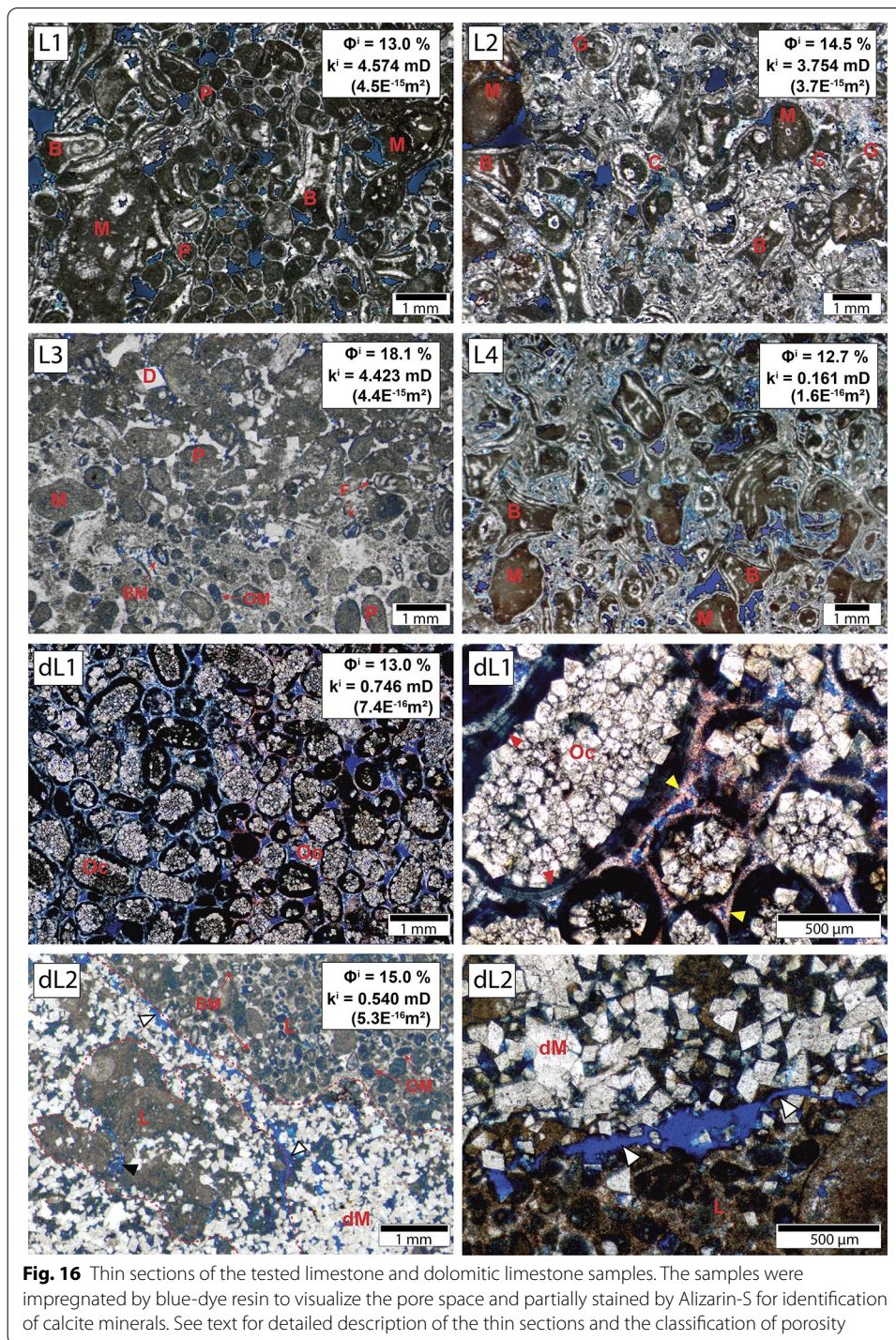
sample L1 measured during the MIP test yielded only $\Phi^{MIP} = 5.5\%$ calculated by the injected pore volume. It can, therefore, be assumed that the sampled volume (very small compared to the test specimens) is not representative of this heterogeneous facies and may have been composed predominantly of micritic particles with small pore volume

and pore size. The distribution of pore throat sizes for sample L1 will, therefore, be assumed to be more or less equivalent to the results of sample L2.

Sample L3

Porous ($\Phi^i = 18.1\%$) fossiliferous grainstone containing benthic foraminifera (F), micritic peloids (P), and oncoids (M) (Fig. 16). The pore space is mainly characterized by biomoldic porosity (dissolution of foraminifera, BM), intraparticle (intraskeletal) porosity, and some oomoldic porosity (dissolution of ooids/peloids, OM). The interparticle pore space is locally overgrown by sparitic cement, which was partially transformed into idiomorphic dolomite rhombs (D). The pore sizes vary from < 0.4 µm (micritic micropores) to 50–100 µm for intraparticle and biomoldic pores. The rare oomoldic pores range between 200 µm up to 1 mm. The pore throats are homogenously distributed in the lower range of capillary throat sizes (capillary throats, 0.6–1 µm) with a slightly negative skew (Fig. 17). Although the throat sizes are relatively small, the abundance of moldic porosity seems to be effectively connected by intercrystalline pores as permeability was measured at $k^i = 4.423$ mD (4.4×10^{-15} m^2).

Fig. 17 Results of mercury intrusion porosimetry (MIP). Cumulative mercury volume (black dashed line) and normalized frequency (blue solid line) are plotted as a function of the pore throat entry diameter. Limestone and dolomitic limestone samples generally tend to have a homogenous distribution of pore throats with sizes from micro- to meso-throats. Dolostone mostly shows distinctly larger pore throats in a rather heterogeneous distribution (skewed, polymodal), caused by large vug pores separated or connected only by very narrow pore throats. The permeability of dolostones is, therefore, often several orders of magnitude lower than that of limestone samples. The contribution of pore throats to permeability is shown as anormalized frequency for every sample (red lines)

Sample L4

Grain- to rudstone, dominated by large micritic peloids (M), lithoclasts (1–2 mm) and abundant fragments of dasyclad green algae (B) (Fig. 16). The pore space is mostly formed by interparticle mesopores and rare oversized solution pores (vugs) up to 1 mm in size. A porosity of $\Phi^i = 12.7\%$ was measured for this facies type. The pore sizes range from < 0.4 μm (micritic micropores) to small mesopores of 100–300 μm. The MIP curves show a perfectly homogenous unimodal distribution with its peak between 0.4 and 0.8 μm in the lowermost zone of the capillary throat sizes (Fig. 17). This implies that the oversized vug pores are all connected by a rather uniform throat size, that controls the flow through the connected pore network. However, the permeability was measured to be $k^i = 0.161$ mD (1.6×10^{-16} m^2) and is lower than expected when compared to the latter limestone facies. The limestone sample is pervaded by a conjugate set of low amplitude stylolites parallel and perpendicular to bedding, indicating pressure solution (see Fig. 3). The stylolites perpendicular to the core axis (direction of flow in the permeability test) are formed by insoluble residue, very fine-grained remnants of the dissolution process, and might act as an impermeable flow barrier. Permeability is, therefore, most likely reduced in the vertical direction.

Dolomitic limestone

Sample dL1

Dolomitized ooid–oncoid grainstone composed entirely of ooids (Oo) and oncoids (Oc) with concentric micritic cortices (red arrows) (Fig. 16dL1). The nuclei were completely dissolved and transformed into euhedral and subhedral dolomite crystals. The pore space consists mainly of interparticle pores between the ooids/oncoids and is partially reduced by circumgranular calcite cement rims (red stain by Alizarin-S, yellow arrows) and small intercrystalline pores between dolomite rhombs. Microporosity is present within the micritic cortices and is often enhanced by very small borings. The effective porosity of the sample was determined to be $\Phi^i = 13.0\%$ and the pore sizes range from 20 to 250 μm for the interparticle mesopores, < 5 μm for the intercrystalline pores, and < 0.4 μm for the micropores. The distribution of pore throat diameters is rather unimodal with a minor tailing towards the lower and upper size range (Fig. 17). The maximum peak indicates capillary pore throat sizes between 0.6 and 1.2 μm and most likely represents the pore throats of the intercrystalline pores between the dolomite crystals. The larger sized meso- to macro-throats (4–10.3 μm) probably correspond to connected interparticle pores not entirely lined by calcite cement rims. Pore throats sized < 4 μm denote constricted throats of cemented intercrystalline pores and possibly pores originated from boring organisms. Sub-capillary pore throats (< 0.4 μm) are allocated to micropores within micritic ooid/oncoid cortices or micritic envelopes of peloids. The flow through the porous network is, therefore, controlled by the pore throat size of the intercrystalline pores and was measured with a permeability of $k^i = 0.746$ mD (7.4×10^{-16} m^2).

Sample dL2

Lithoclastic breccia composed of several cm-large ooid–oncoid grainstone lithoclasts (L) embedded in a strongly dolomitized matrix of equigranular euhedral dolomite rhombs (dM) (Figs. 3, 16). Floating euhedral dolomite rhombs occur within the

lithoclasts near the contact to the dolomitic matrix and indicate the beginning of dolomitization. The pore space is mainly composed of intraparticle, biomoldic (BM), and commonly oomoldic (OM) pores within the grainstone lithoclasts and is isolated by blocky sparitic cement and micrite between particles. Intercrystalline pores are abundant in the dolomitic matrix within the framework of dolomite rhombs. Secondary fracture porosity is common within the lithoclasts (black arrows) and channel porosity has often formed at the contact to the dolomitic matrix (white arrows). The opening width of the fractures is up to 100 μm, while the elongated channel pores reach opening widths of up to 250 μm. The intercrystalline pores are between 20 and 150 μm, the intraparticle and moldic porosity show pore sizes from 20 to 120 μm, and the effective porosity was measured to be $\Phi^i = 15.0\%$. The capillary pressure curve of the MIP test shows a unimodal distribution of pore throat sizes (peak of 0.3–0.8 μm) with rather insignificant tails to smaller and larger throat sizes (Fig. 17). The main pore throat size presumably corresponds to the intercrystalline pores within the dolomitic matrix and, therefore, controls the flow through the interconnected pore network. The elongated channel pores may enhance flow, but are restricted to the smallest throat diameter within the channels (< 5–10 μm). Pore throat diameters < 0.3 μm might be associated with the pore entry diameter of moldic pores and intraskeletal pores through pore throats of the sparitic cement or micritic matrix within the lithoclasts. Permeability was measured at $k^i = 0.540$ mD (5.3×10^{-16} m^2).

Dolostone

Samples D1/D2

Fine-crystalline dolostone with an equigranular idiotopic fabric of mainly euhedral dolomite rhombs in a loosely packed framework (Fig. 18). The pore space consists entirely of intercrystalline pores of early to late diagenetic recrystallization (Flügel and Munnecke 2010). The porosity of sample D2 is reduced to $\Phi^i = 9.8\%$ by black opaque bitumen (B), which originated from fine laminae of the primary limestone facies (presumably mud- to wackestone). For sample D1, the porosity was measured at $\Phi^i = 14.9\%$. The pore sizes of the intercrystalline pores are in the range of < 1–25 μm. The distribution of the pore throats is unimodal for both samples in the meso-throats range, which represents homogenous capillary pore throats and porosity (Fig. 17). Sample D2 has smaller pore throats (2–4 μm) than sample D1 (5–10 μm), due to clogging of the pores by bituminous aggregates. The permeability depends mainly on the pore entry size and is also lower for sample D2 with $k^i = 0.962$ mD (9.5×10^{-16} m^2) and for D1 with $k^i = 1.287$ mD (1.3×10^{-15} m^2).

Samples D3/D4

Dolostone composed of medium-sized subhedral to euhedral dolomite crystals in an inequigranular hypidio- to idiotopic mosaic fabric (Fig. 18). The dolomite rhombs show a blurred zonation, possibly accentuated by ferric oxide ghosts (red arrows) pointing to burial dolomitization (Flügel and Munnecke 2010; Friedman 1965). The pore space

Fig. 18 Thin sections of the tested dolostone samples. The samples were impregnated by blue-dye resin to visualize the pore space and partially stained with Alizarin-S for identification of calcite. See text for a detailed description of the thin sections and the classification of porosity
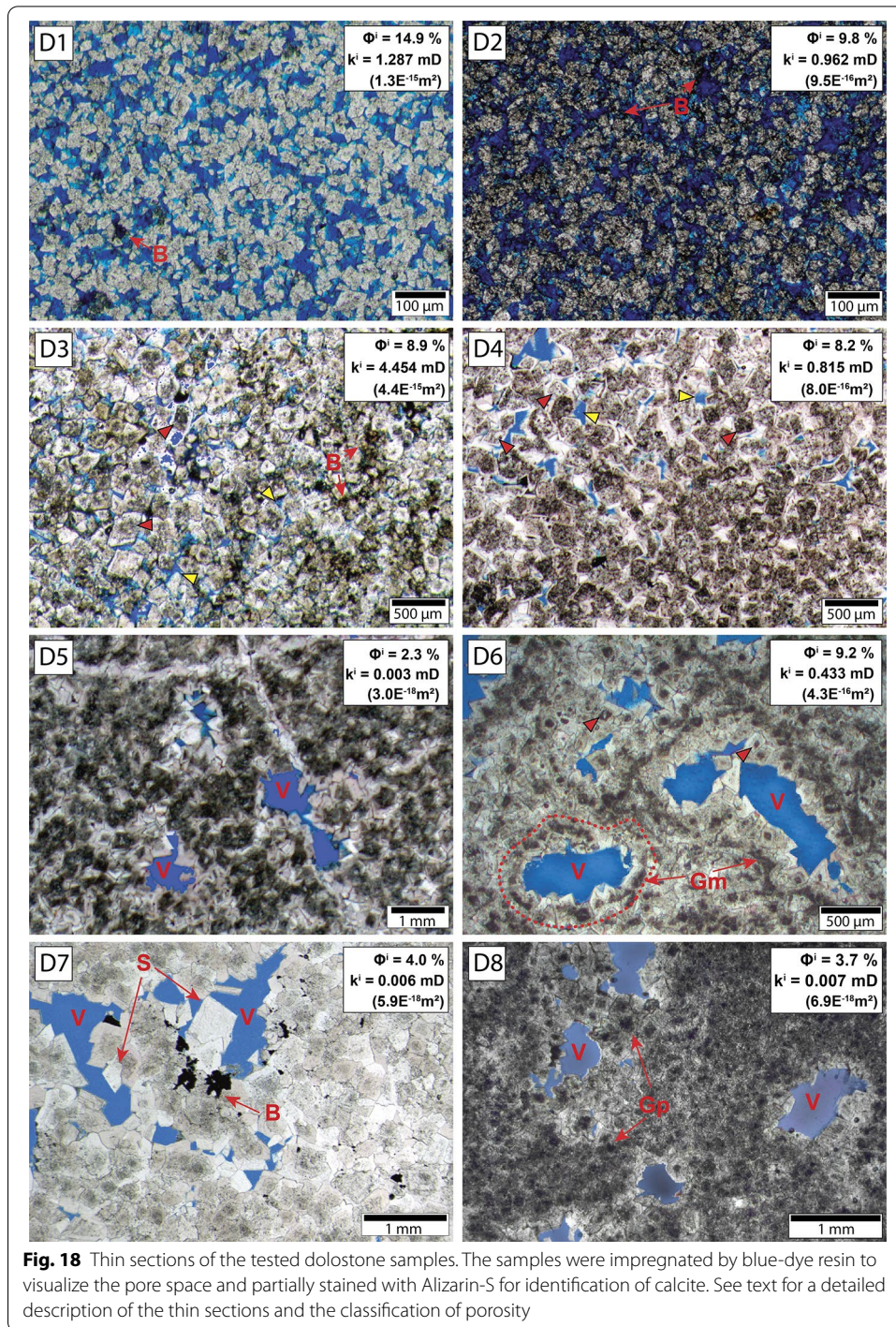
is formed by intercrystalline pores irregularly scattered between aggregated dolomite rhombs (yellow arrows). The primary limestone facies was presumably mud- to packstone with fine organic-rich lamination (indicated by bituminous remnants, sample D3) and peloids (peloid ghost structures, sample D4). The porosity is $\Phi^i = 8.9\%$ for sample D3 and $\Phi^i = 8.2\%$ for sample D4. The size of the intercrystalline pores is mainly between < 1–50 μm

and locally up to 500 μm for elongated pores between larger euhedral crystals. The pore throat sizes show a negatively skewed bimodal (D3) and polymodal distribution (D4) with smaller juxtaposed peaks in the sub-capillary and lower capillary range (Fig. 17). The median throat size is in the range of capillary to supra-capillary throats with 10–100 μm (connection of larger intercrystalline pores). Additional peaks between 1 and 3 μm and 0.07–0.1 μm (only D4) were found, indicating different throat sizes connecting the pore space. The permeability differs by almost one order of magnitude with $k^i = 4.454$ mD (4.4×10^{-15} m^2) for sample D3 and only $k^i = 0.815$ mD (8.0×10^{-16} m^2) for sample D4. The permeability of sample D3 is relatively high compared to its porosity and may have been favored by the microcracks observed in the sample (see Fig. 3). Sample D4, however, showed some locally occurring suture contacts between crystals with reduced intercrystalline porosity and narrow pore throats, which led to a lower permeability.

Sample D5/D6

Medium- to coarsely crystalline dolostone consisting of subhedral to anhedral dolomite crystals in an inequigranular and hypidio- to xenotopic fabric (Fig. 18). The dolomite crystals are tightly packed and partially sutured showing only little intercrystalline pores. The pore space consists mainly of small moldic vugs (V), which are not distinctly connected to the pore network and might be locally isolated. The zonation of the dolomite rhombs indicates burial dolomitization. Ghost structures of insoluble residues (micrite envelopes) might indicate fragments of allochems (Gm) and moldic vugs are presumably dissolved organisms of a primarily wacke- to packstone facies. Pore sizes of rare intercrystalline pores are < 25 μm, and moldic vugs range from 200 μm to 2 mm. The porosity of this rock type is rather low with $\Phi^i = 2.3\%$ (D5), but can increase with increasing number of vugs ($\Phi^i = 9.2\%$, D6). The capillary pressure curve of sample D5 shows a negatively skewed distribution with a peak in the capillary throat size range (meso- to macro-throats) and a tail toward sub-capillary pore throats (Fig. 17). According to Luo and Machel (1995), the curve represents a heterogeneous texture of oversized pores in a tight matrix with rare areas of intercrystalline pores, as observed in the thin sections. The permeability of sample D5 is very low ($k^i = 0.003$ mD, 3.0×10^{-18} m^2), which is due to the low porosity and sparse interconnection of the (vuggy) pore space by intercrystalline pores. In contrast, the permeability of sample D6 is much higher ($k^i = 0.433$ mD, 4.3×10^{-16} m^2), since a large number of vugs favor a possible interconnection by the rare intercrystalline pores.

Sample D7

Coarsely crystalline dolostone consisting of subhedral to anhedral dolomite crystals in an inequigranular xenotopic mosaic fabric (Fig. 18). The dolomite crystals are tightly packed with curved, lobate, and straight intercrystalline boundaries. Intercrystalline pores are rare and the pore space consists of typically separated moldic vugs (V). The mosaic fabric was formed by replacement of a primary fine-grained calcite matrix (mud- to wackestone), and the xenotopic texture and zonal dolomite crystals indicate recrystallization of burial dolomite (Flügel and Munnecke 2010). Large euhedral dolomite rhombs (up to 500 μm) with curved crystal faces (saddle dolomite, S) could grow undisturbed into the vuggy pore space, indicating late diagenetic cementation. Opaque black aggregates are presumably

bitumen as relicts of migrating hydrocarbons (B). The porosity of the sample is $\Phi^i = 4.0\%$ and the pore sizes of rare intercrystalline pores are < 30 μm, and moldic vugs range from 100 μm to 2 mm for large elongated vugs. The MIP curve shows a negatively skewed heterogeneous distribution with a prominent peak for supra-capillary pore throats of 100–200 μm, exceeding the resolution maximum of the MIP device (Fig. 17). The filling of the pore throats probably surpasses 200 μm in some of the larger vugs. The juxtaposed peaks of the capillary curve show a scattered macro-throat interval between 8 and 40 μm before the curve tails towards the sub-capillary zone, with several smaller peaks at 0.04 μm, 0.02 μm, and 0.005 μm. The macro-throat interval represents capillary intercrystalline pores, and sub-capillary micro-throats could be a second generation of intercrystalline pore throats that were almost completely closed by late burial replacement dolomitization. With $k^i = 0.006$ mD (5.9×10^{-18} m²), the permeability is very low due to the heterogeneous distribution of the pore throats and the separated vuggy pore space.

Sample D8
Medium- to coarsely crystalline dolostone consisting of subhedral to anhedral dolomite crystals in an inequigranular and hypidio- to xenotopic fabric (Fig. 18). Sample D8 is similar to samples D 5 and D 6 in being tightly packed, with mainly separated moldic vugs (V) characterizing the pore space. However, ghost structures of former peloids (Gp) indicate a primary limestone facies of a grainstone containing allochems that are dissolved and now represented by moldic vugs. Intercrystalline pores are not visible in the thin section (< 0.5 μm), moldic vugs are between 100 μm and 1 mm in size, and the effective porosity was measured to be $\Phi^i = 3.7\%$. The capillary pressure curve of the sample (Fig. 17) has a bimodal shape, with its maximum peak between 100 and 200 μm (supra-capillary) and the lower peak in the sub-capillary zone (0.03–0.2 μm). The pore throat distribution, therefore, indicates that the larger vug pores are only connected to the pore network by very narrow pore throats of intercrystalline pores. The permeability is, therefore, very low for this sample with $k^i = 0.007$ mD (6.9×10^{-18} m²).

Appendix 2

Diagenetic overprint and impact on hydraulic properties
Early diagenesis (cementation)
Limestone samples L1–L5 represent the original primary facies of shallow, open marine platform deposits and are not affected by dolomitization (except L3 with initial floating dolomite rhombs). The particles forming the grain- to rudstones experienced micritization during their deposition and the primary interparticle pores are mainly preserved. Calcite cement, formed in a marine-phreatic environment as the first generation of marine cements, lines the particles and slightly reduces porosity. The interparticle pores of sample L3 were almost completely closed by sparry calcite. Foraminifera shells and cortices of ooids were dissolved, resulting in the formation of secondary (moldic) porosity.

Initial porosity is relatively high (13–18%), permeability is moderate to low (0.1–4.6 mD, $9.9 \times 10^{-17} - 4.5 \times 10^{-15}$ m²) with contributing pore throat sizes in a range of 20–30 μm and dominant pore sizes of 100–320 μm. Rock strength (50–60 MPa) and

drained bulk modulus (3.2–8 GPa) are rather low. Stress sensitivity for porosity is relatively strong between 3.7 and 9.7×10^{-4} MPa^{-1} and between 1.3 and 3.7×10^{-2} MPa^{-1}for permeability.

Shallow to deep burial (selective dolomitization)

The dolomitic limestone samples are affected by selective dolomitization that originated with the onset of deep burial diagenesis. Sample dL1 is composed of ooids, oncoids, and peloids, coated by thick micritic envelopes/cortices. The former nuclei of the particles were completely replaced by idiomorphic dolomite rhombs. Interparticle pores are preserved and lined by thin calcite cements. Sample dL2 was primarily a lithoclastic limestone with large lithoclasts of an ooidal–oncoidal grainstone facies, showing sparry interparticle calcite cement and moldic porosity (similar facies to L3). The lithoclasts are embedded in a matrix of medium-crystalline idiomorphic dolomite rhombs, that replaced the primary micrite matrix.

Initial porosity is still relatively high (13–15%), permeability is moderately low (0.5–0.8 mD, 4.9×10^{-16}–7.9×10^{-16} m^2), with contributing pore throat sizes in the ranging from 0.6 to 4 μm and dominant pore sizes of 32–100 μm. Rock strength (50–59 MPa) and drained bulk modulus (7.0–8.5 GPa) are rather low. Stress sensitivity for porosity is relatively strong between 4.3 and 4.5×10^{-4} MPa^{-1} and between 1.0 and 3.0×10^{-2} MPa^{-1}for permeability.

Deep burial (complete dolomitization)

The primary limestone facies are completely replaced by dolomite. Remnants of micritic calcite were completely dissolved during deeper burial and the dolostones are formed of a dolomite crystal framework (Samples D1 and D2). Between the idiomorphic dolomite rhombs, a well-connected network of intercrystalline pores has developed, which is slightly clogged by finely dispersed bitumen.

Initial porosity is still high in D1 (14.9%) and reduced to 9.8% in sample D2. Permeability is moderately low (1.0–1.3 mD, 9.9×10^{-16}–1.3×10^{-15} m^2), with contributing pore throat sizes in the range of 0.8–5.0 μm and dominant pore sizes of 100–320 μm. The rock strength (87–95 MPa) and drained bulk modulus (12–17 GPa) are significantly increased by the rigid mineral framework. Stress sensitivity for porosity is moderately low between 1.8 and 2.9×10^{-4} MPa^{-1} and for permeability between 1.1 and 1.3×10^{-2} MPa^{-1}.

Deep burial (cement overgrowth)

A second generation of dolomitization has formed in samples D3 and D4 due to the circulation of oversaturated fluids through the well-connected porous network of the dolostones. The dolomite precipitated as cement in the intercrystalline pores and lines the dolomite rhombs. The pore space is, therefore, reduced. The dolomite rhombs show a zonation indicating a deep burial environment (Reinhold 1998).

Initial porosity is reduced to 8–9%, while permeability is moderately low (0.8 mD, 7.9×10^{-16} m^2) for sample D4 and increased to 4.5 mD (4.4×10^{-15} m^2) for sample D3 by brecciation. The contributing pore throat sizes are in the range of 3–7 μm and dominant pore sizes in the range of 100–320 μm. The rock strength is reduced for sample D3 (69 MPa) due to brecciation and relatively high for sample D4 (112 MPa). The drained

bulk modulus is 8.9 GPa for the brecciated sample and missing for D4 due to a failed test, but is expected to be distinctively stronger. Stress sensitivity for porosity is moderate at 2.9×10^{-4} MPa^{-1} and low for permeability between 0.9 and 1.0×10^{-2} MPa^{-1}.

Late burial (replacement dolomitization, compaction)

Samples D5–D8 show a hypidio- to xenotopic crystallization fabric which originated from replacement of former minerals. Euhedral and anhedral dolomite rhombs are closely packed and have sutured, lobate, and sometimes straight boundaries. The structures of the primary limestone facies are preserved by ghost structures: micritic envelopes around molds (D6) and peloids (D8). Intercrystalline porosity is almost completely reduced and porosity is dominated by relatively large vugs and molds. The pore space is only poorly connected by tiny and penny-shaped intercrystalline pores and pore throats as well as seldom occurring fissures (e.g., D5). The vugs are supposedly separated and barley contribute to the effective flow network.

The initial porosity is moderate between 2.3 and 9.2% and the permeability is very low to low (<0.01–0.4 mD, $<9.9 \times 10^{-18}$–3.9×10^{-16} m^2). Contributing pore throat sizes range from <0.2 to 1.0 μm and dominant pore sizes are 320–1000 μm. Rock strength is high and depends on the irregular occurrence of vugs and molds (77–126 MPa). The drained bulk modulus was only measured for sample D5 and is relatively high at 16 GPa, albeit the micro-fractures observed in the thin sections. The stress sensitivity for porosity is moderate at 3.4×10^{-4} MPa^{-1} (only D5) and varies between 1.5 and 2.3×10^{-2} MPa^{-1} for permeability. The relatively strong stress sensitivity for permeability indicated a restricted flow network with micro-fractures and elongated pores.

Abbreviations

Greek letters

α: Biot coefficient; β: Porosity sensitivity coefficient; γ: Interfacial tension (Erg cm^{-1}); γ_f: Unit weight of the fluid (kN m^{-3}); ε_a: Axial strain; $\Delta\varepsilon_a$: Differential axial strain; $\Delta\varepsilon_a^{el}$: Differential axial strain during linear elastic deformation; ε_c: Circumferential strain; $\Delta\varepsilon_c$: Differential circumferential strain; ε_v: Bulk volumetric strain; $\Delta\varepsilon_v$: Change in bulk volumetric strain; θ: Mercury contact angle; κ: Hydraulic conductivity (m s^{-1}); μ_f: Dynamic fluid viscosity (Pa s); ν: Poisson's ratio; ρ_b: Bulk density (g cm^{-3}); ρ_f: Fluid density (g cm^{-3}); ρ_m: Particle density (g cm^{-3}); σ_s: Uniaxial compressive strength (rock strength) (MPa); σ_s^c: Corrected uniaxial compressive strength (rock strength) (MPa); $\Delta\sigma$: Differential axial stress (MPa); $\sigma_1, \sigma_{2,3}$: Vertical and radial stresses (MPa); Φ^i: Initial porosity (WIP) (%); Φ^E: Eulerian porosity (%); Φ^{max}: Maximum effective porosity (HEP) (%); Φ_{MIP}: Mercury porosity (%); $\Delta\Phi$: Porosity change (%); $\Delta\Phi_{abs}$: Absolute porosity change (%); $\Delta\Phi_{rel}$: Relative porosity change (%).

Roman letters

A: Cross-sectional area (mm^2); a: Cross-sectional area (m^2); a_d: Cross-sectional area at deformed state (m^2); b: Stress sensitivity coefficient of permeability (MPa^{-1}); c: Stress sensitivity coefficient of porosity (MPa^{-1}); C: Circumference (m); ΔC: Difference in circumference (m); C_d: Drained bulk compressibility (GPa^{-1}); C_Φ: Pore volume compressibility (GPa^{-1}); d: Pore throat diameter (μm); d_{eff}: Effective pore throat diameter (μm); d_Φ^{min}: Minimum pore throat diameter (μm); d_Φ^{med}: Median pore throat diameter (μm); d_Φ^{max}: Maximum pore throat diameter (μm); D: Diameter (mm); **DGF-FB**: Dingolfing FB well; e: Exponent; E: Static Young's modulus (GPa); E^{dyn}: Dynamic Young's modulus (GPa); F_{max}: Sample failure load (N); g: Gravity acceleration (m s^{-2}); G^{dyn}: Dynamic shear modulus (GPa); G_s: Shear modulus of the solid constituent (GPa); HEP: Helium porosimetry; h: Piezometric head (m); k: Intrinsic permeability (mD, m^2); k^i: Initial permeability (mD, m^2); Δk_{abs}: Absolute permeability reduction (mD, m^2); Δk_{rel}: Relative permeability reduction (%); k_{rec}: Permeability recovery (%); K_d: Drained bulk modulus (GPa); K_s: Bulk modulus of solid phase (GPa); K^{dyn}: Dynamic bulk modulus (GPa); K_Φ: Porosity modulus (GPa^{-1}); LVDT: Linear variable differential transformer; L: Length (mm); l: Length (m); Δl: Difference in length (m); l_d: Length at deformed state (m); MIP: Mercury intrusion porosimetry; **MSC-4**: Moosburg SC4 well; pdf: Probability distribution function; p.u.: Porosity unit; P_c: Confining pressure (MPa); P_c^{Hg}: Capillary pressure (MPa); P_e: Terzaghi effective pressure (MPa); ΔP_e: Change of Terzaghi effective pressure (MPa); P_i: Reference effective pressure (MPa); P_p: Pore pressure (MPa); P_p^{down}: Pore pressure downstream (MPa); P_p^{up}: Pore pressure upstream (MPa); Q: Flow rate (m^3 s^{-1}); Q_{down}: Flow rate downstream (m^3 s^{-1}); Q_{up}: Flow rate upstream (m^3 s^{-1}); $\bar{q}$: Specific discharge vector (m s^{-1}); REV: Representative elementary volume; S_s^k: Stress sensitivity coefficient for permeability (MPa^{-1}); S_s^Φ: Stress sensitivity coefficient for porosity (MPa^{-1}); THM: Thermal–hydraulic–mechanical; UCS: Uniaxial compressive strength; UCT: Uniaxial compressive test; v_p: Compression wave velocity (m s^{-1}); v_s: Shear wave velocity (m s^{-1}); v_d: Dilatational wave velocity (m s^{-1}); V_b: Bulk volume at

deformed state (cm³); ΔV_b: Change in bulk volume (cm³); V_b^i: Initial bulk volume (cm³); V_f: Fluid volume (cm³); V_g^{He}: Helium grain volume (cm³); V^{Hg}: Intruded mercury volume (cm³); V_{max}^{Hg}: Maximum intruded mercury volume (cm³); V_Φ: Pore volume (cm³); ΔV_Φ: Change in pore volume (cm³); V_Φ^i: Initial pore volume (cm³); WIP: Water intrusion porosimetry; W_d: Dry mass (g); W_s^w: Saturated mass (g); z: Elevation (m).

Availability of data and materials
The data sets generated and analyzed during the current study are available from the corresponding author on reasonable request.

Declarations

Competing interests
The authors declare that they have no competing interests.

Author details
[1]Chair of Hydrogeology, Technical University of Munich, Arcisstr. 21, 80333 Munich, Germany. [2]Chair of Engineering Geology, Technical University of Munich, Arcisstr. 21, 80333 Munich, Germany. [3]Chair of Geology, Friedrich-Alexander University Erlangen-Nürnberg, Schlossgarten 5, 91054 Erlangen, Germany.

References
Agemar T, Weber J, Schulz R. Deep geothermal energy production in Germany. Energies. 2014;7(7):4397–416. https://doi.org/10.3390/en7074397.
Alyafei N, Mckay TJ, Solling TI. Characterization of petrophysical properties using pore-network and lattice-Boltzmann modelling: choice of method and image sub-volume size. J Petrol Sci Eng. 2016;145:256–65. https://doi.org/10.1016/j.petrol.2016.05.021.
Anovitz LM, Cole DR. Characterization and analysis of porosity and pore structures. Rev Mineral Geochem. 2015;80(1):61–164. https://doi.org/10.2138/rmg.2015.80.04.
Atapour H, Mortazavi A. The influence of mean grain size on unconfined compressive strength of weakly consolidated reservoir sandstones. J Petrol Sci Eng. 2018;171:63–70. https://doi.org/10.1016/j.petrol.2018.07.029.
Bachmann GH, Müller M, Weggen K. Evolution of the Molasse Basin (Germany, Switzerland). Tectonophysics. 1987;137(1–4):77–92. https://doi.org/10.1016/0040-1951(87)90315-5.
Bakhtiari HA, Moosavi A, Kazemzadeh E, Kamran G, Esfahani MR, Vali J. The effect of rock types on pore volume compressibility of limestone and dolomite samples. Geopersia. 2011;1(1):37–82. https://doi.org/10.22059/jgeope.2011.22163.
Baud P, Rolland A, Heap M, Xu T, Nicolé M, Ferrand T, et al. Impact of stylolites on the mechanical strength of limestone. Tectonophysics. 2016;690:4–20. https://doi.org/10.1016/j.tecto.2016.03.004.
BayStMivt. Bayerischer Geothermieatlas: Hydrothermale Energiegewinnung. München: Bayerisches Staatsministerium für Wirtschaft, Infrastruktur, Verkehr und Technologie; 2012.
Bear J. Dynamics of fluids in porous media. New York: Dover Publications; 1988.
Benson P, Schubnel A, Vinciguerra S, Trovato C, Meredith P, Young RP. Modeling the permeability evolution of microcracked rocks from elastic wave velocity inversion at elevated isostatic pressure. J Geophys Res. 2006. https://doi.org/10.1029/2005JB003710.
Bernabe Y, Brace WF, Evans B. Permeability, porosity and pore geometry of hot-pressed calcite. Mech Mater. 1982;1(3):173–83. https://doi.org/10.1016/0167-6636(82)90010-2.

Bernabe Y. The effective pressure law for permeability in Chelmsford granite and Barre granite. Int J Rock Mech Min Sci Geomech Abstracts. 1986;23(3):267–75. https://doi.org/10.1016/0148-9062(86)90972-1.

Biot MA. General theory of three dimensional consolidation. J Appl Phys. 1941;12:155–64.

Birner J. Hydrogeologisches Modell des Malmaquifers im Süddeutschen Molassebecken. Freie Universität Berlin: Freie Universität Berlin; 2013.

Blöcher G, Reinsch T, Hassanzadegan A, Milsch H, Zimmermann G. Direct and indirect laboratory measurements of poroelastic properties of two consolidated sandstones. Int J Rock Mech Min Sci. 2014;67:191–201. https://doi.org/10.1016/j.ijrmms.2013.08.033.

Blöcher GM. Pore space reconstruction of porous media: Coupling of microstructure, rock mechanics and ow properties depending Coupling of microstructure, rock mechanics and ow properties depending on effective pressure [Dissertation]. Berlin: Technische Universität Berlin; 2008.

Blöcher GM, Zimmermann G, Milsch H. Impact of poroelastic response of sandstones on geothermal power production. Pure Appl Geophys. 2009;166(5–7):1107–23. https://doi.org/10.1007/s00024-009-0475-4.

Böhm F. Die Lithofazies des Oberjura (Malm) im Großraum München und deren Einfluss auf die tiefengeothermische Nutzung [Dissertation]. FU Berlin: Freie Universität Berlin; 2012.

Böhm F, Birner J, Steiner U, Koch R, Sobott R, Schneider M, Wang A. Tafelbankiger Dolomit in der Kernbohrung Moosburg SC4: Ein Schlüssel zum Verständnis der Zuflussraten in Geothermiebohrungen (Östliches Molassebecken, Malm Delta-Zeta Süddeutschland). Z Geol Wiss. 2011;39:117–57.

Böhm F, Savvatis A, Steiner U, Schneider M, Koch R. Lithofazielle Reservoircharakterisierung zur geothermischen Nutzung des Malm im Großraum München. Grundwasser. 2013;18(1):3–13. https://doi.org/10.1007/s00767-012-0202-4.

Bohnsack D, Potten M, Käsling H, Thuro K, Zosseder K. Geomechanical investigation of a geothermal aquifer in the South German Molasse Basin. In: Da Fontoura SAB, Rocca RJ, Mendoza JP, editors. Rock mechanics for natural resources and infrastructure development: full papers. London: CRC Press; 2019. p. 3136–43.

Bohnsack D, Potten M, Pfrang D, Wolpert P, Zosseder K. Porosity–permeability relationship derived from Upper Jurassic carbonate rock cores to assess the regional hydraulic matrix properties of the Malm reservoir in the South German Molasse Basin. Geotherm Energy. 2020;8(1):61. https://doi.org/10.1186/s40517-020-00166-9.

Brantut N, Heap MJ, Baud P, Meredith PG. Mechanisms of time-dependent deformation in porous limestone. J Geophys Res Solid Earth. 2014;119(7):5444–63. https://doi.org/10.1002/2014JB011186.

Brehme M, Blöcher G, Cacace M, Kamah Y, Sauter M, Zimmermann G. Permeability distribution in the Lahendong geothermal field: a blind fault captured by thermal–hydraulic simulation. Environ Earth Sci. 2016;75(14):577. https://doi.org/10.1007/s12665-016-5878-9.

Büchi UP, Lemcke K, Wiener G, Zimdars J. Geologische Ergebnisse der Erdölexploration auf das Mesozoikum im Untergrund des schweizerischen Molassebeckens. Bull Ver Schweiz Petroleum-Geol u Ing. 1965;32(82):7–38.

Cacace M, Jacquey AB. Flexible parallel implicit modelling of coupled thermal–hydraulic–mechanical processes in fractured rocks. Solid Earth. 2017;8(5):921–41. https://doi.org/10.5194/se-8-921-2017.

Cacace M, Blöcher GM, Watanabe N, Moeck I, Börsing N, Scheck-Wenderoth M, et al. Modelling of fractured carbonate reservoirs: outline of a novel technique via a case study from the Molasse Basin, southern Bavaria, Germany. Environ Earth Sci. 2013;70(8):3585–602. https://doi.org/10.1007/s12665-013-2402-3.

Cant JL, Siratovich PA, Cole JW, Villeneuve MC, Kennedy BM. Matrix permeability of reservoir rocks, Ngatamariki geothermal field, Taupo Volcanic Zone, New Zealand. Geotherm Energy. 2018;6(1):225. https://doi.org/10.1186/s40517-017-0088-6.

Chang C, Zoback MD, Khaksar A. Empirical relations between rock strength and physical properties in sedimentary rocks. J Petrol Sci Eng. 2006;51(3–4):223–37. https://doi.org/10.1016/j.petrol.2006.01.003.

Cheng AH-D. Poroelasticity. Cham: Springer; 2016.

Choquette PW, Pray LC. Geologic nomenclature and classification of porosity in sedimentary carbonates. Bulletin. 1970;54. https://doi.org/10.1306/5d25c98b-16c1-11d7-8645000102c1865d.

Coelho LC, Soares AC, Ebecken NFF, Drummond Alves JL, Landau L. Modelling mechanical behaviour of limestone under reservoir conditions. Int J Numer Anal Meth Geomech. 2006;30(14):1477–500. https://doi.org/10.1002/nag.543.

Darcy H. Les fontaines publiques de la ville de Dijon. Paris: Victor Dalmont; 1856.

Dautriat J, Gland N, Dimanov A, Raphanel J. Hydromechanical behavior of heterogeneous carbonate rock under proportional triaxial loadings. J Geophys Res. 2011. https://doi.org/10.1029/2009JB000830.

David C, Wong T, Zhu W, Zhang J. Laboratory measurement of compaction-induced permeability change in porous rocks: Implications for the generation and maintenance of pore pressure excess in the crust. PAGEOPH. 1994;143(1–3):425–56. https://doi.org/10.1007/BF00874337.

David C, Menendez B, Zhu W, Wong T. Mechanical compaction, microstructures and permeability evolution in sandstones. Phys Chem Earth Part A. 2001;26(1–2):45–51. https://doi.org/10.1016/S1464-1895(01)00021-7.

David C, Dautriat J, Sarout J, Delle Piane C, Menéndez B, Macault R, Bertauld D. Mechanical instability induced by water weakening in laboratory fluid injection tests. J Geophys Res Solid Earth. 2015;120(6):4171–88. https://doi.org/10.1002/2015JB011894.

Delle Piane C, Burlini L, Kunze K. The influence of dolomite on the plastic flow of calcite. Tectonophysics. 2009;467(1–4):145–66. https://doi.org/10.1016/j.tecto.2008.12.022.

Detournay E, Cheng AH-D, editors. Fundamentals of poroelasticity. In: Comprehensive rock engineering: principles, practice and projects. Oxford: Pergamon Press; 1993.

DIN EN 14146. Natural stone test methods—Determination of the dynamic modulus of elasticity (by measuring the fundamental resonance frequency). Berlin: Beuth Verlag GmbH; 2004. https://doi.org/10.31030/9513598.

DIN EN 14579. Natural stone test methods—Determination of sound speed propagation. Berlin: Beuth Verlag GmbH; 2005. https://doi.org/10.31030/9562672.

Dong J-J, Hsu J-Y, Wu W-J, Shimamoto T, Hung J-H, Yeh E-C, et al. Stress-dependence of the permeability and porosity of sandstone and shale from TCDP Hole-A. Int J Rock Mech Min Sci. 2010;47(7):1141–57. https://doi.org/10.1016/j.ijrmms.2010.06.019.

Drews MC, Bauer W, Caracciolo L, Stollhofen H. Disequilibrium compaction overpressure in shales of the Bavarian Foreland Molasse Basin: results and geographical distribution from velocity-based analyses. Mar Pet Geol. 2018;92:37–50. https://doi.org/10.1016/j.marpetgeo.2018.02.017.

Drews MC, Hofstetter P, Zosseder K, Shipilin V, Stollhofen H. Predictability and controlling factors of overpressure in the North Alpine Foreland Basin, SE Germany: an interdisciplinary post-drill analysis of the Geretsried GEN-1 deep geothermal well: an interdisciplinary post-drill analysis of the Geretsried GEN-1 deep geothermal well. Geotherm Energy. 2020;8(1):1. https://doi.org/10.1186/s40517-020-00175-8.

Dunham RJ. Classification of carbonate rocks according to depositional texture. In: Ham WE, ed. Classification of carbonate rocks: a symposium. 6th ed. Tulsa, Okla.: American Association of Petroleum Geologists; 1978. pp. 108–121.

Egert R, Seithel R, Kohl T, Stober I. Triaxial testing and hydraulic–mechanical modeling of sandstone reservoir rock in the Upper Rhine Graben. Geotherm Energy. 2018;6(1):49. https://doi.org/10.1186/s40517-018-0109-0.

Ehrenberg SN, Nadeau PH (2005) Sandstone vs. carbonate petroleum reservoirs: a global perspective on porosity-depth and porosity-permeability relationships. Bulletin. 89(4):435–45. https://doi.org/10.1306/11230404071

Ehrenberg SN, Nadeau PH, Steen Ø. Petroleum reservoir porosity versus depth: Influence of geological age. Bulletin. 2009;93(10):1281–96. https://doi.org/10.1306/06120908163.

Fabre D, Gustkiewicz J. Poroelastic properties of limestones and sandstones under hydrostatic conditions. Int J Rock Mech Min Sci. 1997;34(1):127–34. https://doi.org/10.1016/S1365-1609(97)80038-X.

Farqad AH. Geomechanical characterizations and correlations to reduce uncertainties of carbonate reservoir analysis [Doctoral dissertation]. Missouri: Missouri University of Science and Technology; 2018.

Farquharson N, Schubert A, Steiner U. Geothermal energy in Munich (and beyond): a geothermal city case study. GRC Trans. 2016;40:189–96.

Fatt I, Davis DH. Reduction in permeability with overburden pressure. J Petrol Technol. 1952;4(12):16. https://doi.org/10.2118/952329-G.

Flügel E, Munnecke A. Microfacies of carbonate rocks: analysis, interpretation and application. 2nd ed. Berlin, Heidelberg: Springer; 2010.

Folk RL. Petrology of sedimentary rocks. Austin, Texas: Hemphill Pub Co; 1974.

Friedman GM. Terminology of crystallization textures and fabrics in sedimentary rocks. SEPM JSR. 1965. https://doi.org/10.1306/74d7131b-2b21-11d7-8648000102c1865d.

Fritzer T. Bayerischer Geothermieatlas - Hydrothermale Energiegewinnung: Technik, wirtschaftliche Aspekte, Risiken; hydrothermale Grundwasserleiter in Bayern; Untergrundtemperaturen in Bayern. München: StMWIVT; 2012.

Ghabezloo S, Sulem J, Guédon S, Martineau F. Effective stress law for the permeability of a limestone. Int J Rock Mech Min Sci. 2009a;46(2):297–306. https://doi.org/10.1016/j.ijrmms.2008.05.006.

Ghabezloo S, Sulem J, Saint-Marc J. Evaluation of a permeability–porosity relationship in a low-permeability creeping material using a single transient test. Int J Rock Mech Min Sci. 2009b;46(4):761–8. https://doi.org/10.1016/j.ijrmms.2008.10.003.

Gobran BD, Brigham WE, Ramey HJ. Absolute permeability as a function of confining pressure, pore pressure, and temperature. SPE Form Eval. 1987;2(01):77–84. https://doi.org/10.2118/10156-PA.

Goldbrunner JE, Vasvári V. Hydrogeology and geothermic simulation of the geothermal doublet at Waldkraiburg (Bavaria). AJES. 2016. https://doi.org/10.17738/ajes.2016.0007.

Hart DJ, Wang HF. Laboratory measurements of a complete set of poroelastic moduli for Berea sandstone and Indiana limestone. J Geophys Res. 1995;100(B9):17741–51. https://doi.org/10.1029/95JB01242.

Hassanzadegan A. Thermomechanical and poromechanical behavior of Flechtinger sandstone [Doctoral Thesis]. Berlin: Technische Universität Berlin, Fakultät VI - Planen Bauen Umwelt; 2013.

Hassanzadegan A, Zimmermann G. A poroelastic description of permeability evolution. Pure Appl Geophys. 2014;171(7):1187–201. https://doi.org/10.1007/s00024-013-0714-6.

Hassanzadegan A, Blöcher G, Zimmermann G, Milsch H. Thermoporoelastic properties of Flechtinger sandstone. Int J Rock Mech Min Sci. 2012;49:94–104. https://doi.org/10.1016/j.ijrmms.2011.11.002.

Hassanzadegan A, Blöcher GM, Milsch H, Urpi L, Zimmermann G. The effects of temperature and pressure on the porosity evolution of flechtinger sandstone. Rock Mech Rock Eng. 2014;47(2):421–34. https://doi.org/10.1007/s00603-013-0401-z.

Hassanzadegan A, Guérizec R, Reinsch T, Blöcher G, Zimmermann G, Milsch H. Static and dynamic moduli of malm carbonate: a poroelastic correlation. Pure Appl Geophys. 2016;173(8):2841–55. https://doi.org/10.1007/s00024-016-1327-7.

Heap M, Reuschlé T, Baud P, Renard F, Iezzi G. The permeability of stylolite-bearing limestone. J Struct Geol. 2018;116:81–93. https://doi.org/10.1016/j.jsg.2018.08.007.

Heap MJ, Lavallée Y, Petrakova L, Baud P, Reuschlé T, Varley NR, Dingwell DB. Microstructural controls on the physical and mechanical properties of edifice-forming andesites at Volcán de Colima. Mexico J Geophys Res Solid Earth. 2014;119(4):2925–63. https://doi.org/10.1002/2013JB010521.

Heap MJ, Kushnir ARL, Gilg HA, Wadsworth FB, Reuschlé T, Baud P. Microstructural and petrophysical properties of the Permo-Triassic sandstones (Buntsandstein) from the Soultz-sous-Forêts geothermal site (France). Geotherm Energy. 2017. https://doi.org/10.1186/s40517-017-0085-9.

Heap MJ, Kushnir ARL, Gilg HA, Violay MES, Harlé P, Baud P. Petrophysical properties of the Muschelkalk from the Soultz-sous-Forêts geothermal site (France), an important lithostratigraphic unit for geothermal exploitation in the Upper Rhine Graben. Geotherm Energy. 2019a. https://doi.org/10.1186/s40517-019-0145-4.

Heap MJ, Villeneuve M, Kushnir AR, Farquharson JI, Baud P, Reuschlé T. Rock mass strength and elastic modulus of the Buntsandstein: an important lithostratigraphic unit for geothermal exploitation in the Upper Rhine Graben. Geothermics. 2019b;77:236–56. https://doi.org/10.1016/j.geothermics.2018.10.003.

Heiland J. Permeability of triaxially compressed sandstone: influence of deformation and strain-rate on permeability. Pure Appl Geophys. 2003;160(5):889–908. https://doi.org/10.1007/PL00012571.

Heine F, Zosseder K, Einsiedl F (2021) Hydrochemical zoning and chemical evolution of the deep upper jurassic thermal groundwater reservoir using water chemical and environmental isotope data. Water. 13(9):1162. https://doi.org/10.3390/w13091162

Hofmann H, Blöcher G, Börsing N, Maronde N, Pastrik N, Zimmermann G. Potential for enhanced geothermal systems in low permeability limestones—stimulation strategies for the Western Malm karst (Bavaria). Geothermics. 2014;51:351–67. https://doi.org/10.1016/j.geothermics.2014.03.003.

Holt RM, Brignoli M, Kenter CJ, Meij R, Schutjens P. From core compaction to reservoir compaction: correction for core damage effects. In: Paper presented at the SPE/ISRM rock mechanics in petroleum engineering, Trondheim, Norway, July 1998. 1998. https://doi.org/10.2118/47263-MS.

Homuth S. Aufschlussanalogstudie zur Charakterisierung oberjurassischer Geothermischer Karbonatreservoire im Molassebecken [Dissertation]. Darmstadt: Technische Universität Darmstadt; 2014.

Homuth S, Sass I. Outcrop analogue vs. reservoir data: characteristics and controlling factors of physical properties of the upper jurassic geothermal carbonate reservoirs of the Molasse Basin, Germany. In: Thirty-Eighth Workshop on Geothermal Reservoir Engineering; 26–26 Februaray 2014; Stanford, California; 2014.

Homuth S, Götz AE, Sass I. Lithofacies and depth dependency of thermo- and petrophysical rock parameters of the Upper Jurassic geothermal carbonate reservoirs of the Molasse Basin. Zeitschrift Der Deutschen Gesellschaft Für Geowissenschaften. 2014;165(3):469–86. https://doi.org/10.1127/1860-1804/2014/0074.

Homuth S, Götz AE, Sass I. Physical properties of the geothermal carbonate reservoirs of the Molasse Basin, Germany—outcrop analogue vs. reservoir data. In: Proceedings World Geothermal Congress, Melbourne, Australia, 19–25 April 2015. 2015.

Howarth DF. The effect of pre-existing microcavities on mechanical rock performance in sedimentary and crystalline rocks. Int J Rock Mech Min Sci Geomech Abstracts. 1987;24(4):223–33. https://doi.org/10.1016/0148-9062(87)90177-X.

Jaeger JC, Cook NGW, Zimmerman RW. Fundamentals of rock mechanics: lectures held at the department for mechanics of deformable bodies September 1969. 4th ed. Malden: Blackwell Publ; 2011.

Jones FO, Owens WW. A laboratory study of low-permeability gas sands. J Petrol Technol. 1980;32(09):1631–40. https://doi.org/10.2118/7551-pa.

Kashif M, Cao Y, Yuan G, Asif M, Javed K, Mendez JN, et al. Pore size distribution, their geometry and connectivity in deeply buried Paleogene Es1 sandstone reservoir, Nanpu Sag, East China. Pet Sci. 2019;16(5):981–1000. https://doi.org/10.1007/s12182-019-00375-3.

Kennedy BM, Farquhar A, Hilderman R, Villeneuve MC, Heap MJ, Mordensky S, et al. Pressure controlled permeability in a conduit filled with fractured hydrothermal breccia reconstructed from ballistics from Whakaari (White Island), New Zealand. Geosciences. 2020;10(4):138. https://doi.org/10.3390/geosciences10040138.

Keupp H, Koch R, Schweigert G, Viohl G. Geological history of the Southern Franconian Alb—the area of the Solnhofen Lithographic Limestone. N J Geol Palaontol . 2007;245(1):3–21. https://doi.org/10.1127/0077-7749/2007/0245-0003.

Kluge C, Blöcher G, Barnhoorn A, Schmittbuhl J, Bruhn D. Permeability evolution during shear zone initiation in low-porosity rocks. Rock Mech Rock Eng. 2021. https://doi.org/10.1007/s00603-020-02356-0.

Koch R. Daten zur Fazies und Diagenese von Massenkalken und ihre Extrapolation nach Süden bis unter die Nördlichen Kalkalpen. Geologische Blätter Für Nordost-Bayern. 1997;47(1–4):117–50.

Koch R, Munnecke A. Fazielle Entwicklung und Korrelation des Oberjura in den Bohrungen Bad Waldsee GB2 und Altensteig 1 (Süddeutschland; Molasse-Becken; Impressamergel- bis hangende Bankkalk-Formation). Geologische Blätter Für Nordost-Bayern. 2016;66:165–203.

Koch R, Senowbari-Daryan B, Strauss H. The late jurassic 'Massenkalk fazies' of Southern Germany: calcareous sand piles rather than organic reefs. Facies. 1994;31(1):179–208. https://doi.org/10.1007/BF02536939.

Konrad F, Savvatis A, Wellmann F, Zosseder K. Hydraulic behavior of fault zones in pump tests of geothermal wells: a parametric analysis using numerical simulations for the Upper Jurassic aquifer of the North Alpine Foreland Basin. Geotherm Energy. 2019;7(1):129. https://doi.org/10.1186/s40517-019-0137-4.

Kowalski WC. The interdependence between the strength and voids ratio of limestones and marbles in connection with their water saturating and anisotropy. In: Proc. 1st Congr. ISRM, Lissbon. 1966(1):143–4.

Kushnir ARL, Heap MJ, Baud P, Gilg HA, Reuschlé T, Lerouge C, et al. Characterizing the physical properties of rocks from the Paleozoic to Permo-Triassic transition in the Upper Rhine Graben. Geotherm Energy. 2018. https://doi.org/10.1186/s40517-018-0103-6.

Kushnir AR, Kennedy LA, Misra S, Benson P, White JC. The mechanical and microstructural behaviour of calcite-dolomite composites: an experimental investigation. J Struct Geol. 2015;70:200–16. https://doi.org/10.1016/j.jsg.2014.12.006.

Lemcke K. Übertiefe Grundwässer im süddeutschen Alpenvorland. Bulletin der Vereinigung Schweiz. Petroleum-Geologen und -Ingenieure. 1976;42(103):9–18.

Lemcke K. Das bayerische Alpenvorland vor der Eiszeit: Erdgeschichte - Bau - Bodenschätze. Stuttgart: Schweizerbart; 1988.

Lucia FJ. Origin and petrophysics of dolostone pore space. Geol Soc Lond Special Publ. 2004;235(1):141–55. https://doi.org/10.1144/GSL.SP.2004.235.01.06.

Lucia FJ. Carbonate reservoir characterization: an integrated approach. Berlin, Heidelberg: Springer; 2007.

Luo P, Machel HG. Pore size and pore throat types in a heterogeneous dolostone reservoir, devonian grosmont formation, Western Canada Sedimentary Basin. Bulletin. 1995. https://doi.org/10.1306/7834de5e-1721-11d7-8645000102c1865d.

Lüschen E, Wolfgramm M, Fritzer T, Dussel M, Thomas R, Schulz R. 3D seismic survey explores geothermal targets for reservoir characterization at Unterhaching, Munich, Germany. Geothermics. 2014;50:167–79. https://doi.org/10.1016/j.geothermics.2013.09.007.

Machel HG, editor. Sedimentology. Berlin: Springer; 1978.

Machel HG. Concepts and models of dolomitization: a critical reappraisal. Geol Soc Lond Special Publ. 2004;235(1):7–63. https://doi.org/10.1144/GSL.SP.2004.235.01.02.

Mackenzie JK. The elastic constants of a solid containing spherical holes. Proc Phys Soc B. 1950;63(1):2–11. https://doi.org/10.1088/0370-1301/63/1/302.

McPhee C, Reed J, Zubizarreta I. Core analysis: a best practice guide. Amsterdam: Elsevier; 2015.

Meng F, Baud P, Ge H, Wong T. The effect of stress on limestone permeability and effective stress behavior of damaged samples. J Geophys Res Solid Earth. 2019;124(1):376–99. https://doi.org/10.1029/2018JB016526.

Meng F, Li X, Baud P, Wong T. Bedding anisotropy and effective stress law for the permeability and deformation of clayey sandstones. Rock Mech Rock Eng. 2020. https://doi.org/10.1007/s00603-020-02306-w.

Menke HP, Maes J, Geiger S. Upscaling the porosity-permeability relationship of a microporous carbonate for Darcy-scale flow with machine learning. Sci Rep. 2021;11(1):2625. https://doi.org/10.1038/s41598-021-82029-2.

Meyer RKF, Schmidt-Kaler H. Paläogeographie und Schwammriffentwicklung des süddeutschen Malm—ein Überblick. Facies. 1990a;23(1):175–84.

Meyer RKF, Schmidt-Kaler H. Paläogeographischer Atlas des süddeutschen Oberjura (Malm). Stuttgart, Germany: Schweizerbart Science Publishers; 1990b.

Meyer RKF. "Moosburg 4", die erste Kernbohrung durch den Malm unter der bayerischen Molasse. Erlanger Geol Abh. 1994;123:51–81.

Meyer RKF, Schmidt-Kaler H. Jura. In: Bay GLA, editor. Erläuterungen zur Geologischen Karte von Bayern 1:500.000. 4th edn. München: Bayerisches Geologisches Landesamt; 1996.

Moosavi SA, Goshtasbi K, Kazemzadeh E, Bakhtiari HA, Esfahani MR, Vali J. Relationship between porosity and permeability with stress using pore volume compressibility characteristic of reservoir rocks. Arab J Geosci. 2014;7(1):231–9. https://doi.org/10.1007/s12517-012-0760-x.

Mraz E. Reservoir characterization to improve exploration concepts of the upper jurassic in the Southern Bavarian Molasse Basin [Dissertation]. Munich: Technical University of Munich; 2018.

Mraz E, Moeck I, Bissmann S, Hild S. Multiphase fossil normal faults as geothermal exploration targets in the Western Bavarian Molasse Basin: Case study Mauerstetten. Zeitschrift Der Deutschen Gesellschaft Für Geowissenschaften. 2018;169(3):389–411. https://doi.org/10.1127/zdgg/2018/0166.

Mraz E, Wolfgramm M, Moeck I, Thuro K. Diagenesis of the upper jurassic carbonate rocks within deep geothermal boreholes of the north alpine foreland Basin in Germany. In: Shakoor A, Cato K (eds) IAEG/AEG Annual Meeting Proceedings, San Francisco, Claifornia, 2018. Cham: Springer International Publishing; 2019. https://doi.org/10.1007/978-3-319-93133-3_9.

Mutschler T. Einaxiale Druckversuche an zylindrischen Gesteinsprüfkörpern: Neufassung der Empfehlung Nr. 1 des Arbeitskreises „Versuchstechnik Fels" der Deutschen Gesellschaft für Geotechnik e. V. Bautechnik. 2004;81(10):825–34. https://doi.org/10.1002/bate.200490194.

Nabawy BS, Géraud Y, Rochette P, Bur N. Pore-throat characterization in highly porous and permeable sandstones. Bulletin. 2009;93(6):719–39. https://doi.org/10.1306/03160908131.

Nedjar B. Formulation of a nonlinear porosity law for fully saturated porous media at finite strains. J Mech Phys Solids. 2013;61(2):537–56. https://doi.org/10.1016/j.jmps.2012.09.010.

Nicolas A, Fortin J, Regnet JB, Verberne BA, Plümper O, Dimanov A, et al. Brittle and semibrittle creep of Tavel limestone deformed at room temperature. J Geophys Res Solid Earth. 2017;122(6):4436–59. https://doi.org/10.1002/2016JB013557.

Niebuhr B. Lithostratigraphie der Weißjura-Gruppe der Frankenalb (außeralpiner Oberjura) und der mittel- bis oberjurassischen Reliktvorkommen zwischen Straubing und Passau (Bayern): Beitrag zur Stratigraphie von Deutschland. Hannover: Dt. Ges. für Geowiss; 2014.

Obert L, Duvall WI. Rock mechanics and the design of structures in rock. New York: Wiley; 1967.

Oliveira GLd, Ceia MA, Missagia RM, Archilha NL, Figueiredo L, Santos VH, Lima Neto I. Pore volume compressibilities of sandstones and carbonates from Helium porosimetry measurements. J Petrol Sci Eng. 2016;137:185–201. https://doi.org/10.1016/j.petrol.2015.11.022.

Pei L, Rühaak W, Stegner J, Bär K, Homuth S, Mielk P, Sass I. Thermo-Triax: an apparatus for testing petrophysical properties of rocks under simulated geothermal reservoir conditions. Geotech Test J. 2014;38(1):20140056. https://doi.org/10.1520/GTJ20140056.

Pei L, Blöcher G, Milsch H, Zimmermann G, Sass I, Huenges E. Thermo-mechanical properties of upper jurassic (Malm) carbonate rock under drained conditions. Rock Mech Rock Eng. 2018;51(1):23–45. https://doi.org/10.1007/s00603-017-1313-0.

Potten M. Geomechanical characterization of sedimentary and crystalline geothermal reservoirs [Dissertation]. Munich, Germany: Technical University of Munich; 2020.

Przybycin AM, Scheck-Wenderoth M, Schneider M. The origin of deep geothermal anomalies in the German Molasse Basin: results from 3D numerical models of coupled fluid flow and heat transport. Geotherm Energy. 2017. https://doi.org/10.1186/s40517-016-0059-3.

Randazzo AF, Zachos LG. Classification and description of dolomitic fabrics of rocks from the Floridan aquifer, U.S.A. Sed Geol. 1984;37(3):151–62. https://doi.org/10.1016/0037-0738(84)90005-8.

Regnet JB, David C, Robion P, Menéndez B. Microstructures and physical properties in carbonate rocks: a comprehensive review. Mar Pet Geol. 2019;103:366–76. https://doi.org/10.1016/j.marpetgeo.2019.02.022.

Reinhold C. Multiple episodes of dolomitization and dolomite recrystallization during shallow burial in Upper Jurassic shelf carbonates: Eastern Swabian Alb, southern Germany. Sed Geol. 1998;121(1–2):71–95. https://doi.org/10.1016/S0037-0738(98)00077-3.

Rentsch W, Krompholz G. Bestimmung elastischer Konstanten durch Schallgeschwindigkeitsmessungen. Zeitschrift Für Bergbau, Hüttenwesen Und Verwandte Wissenschaften. 1961;13(7–8):492–504.

Rioseco EM, Ziesch J, Wawerzinek H, Hartmann H von, Thomas R, Buness H. 3-D geothermal reservoir modeling of the upper jurassic carbonate aquifer in the City of Munich (Germany) under the thermal-hydraulic influence of optimized geothermal multi-well patterns—Project GeoParaMoL. In: Simmons S, Kirby S, Verplanck P, Kelley K, editors. In: Proceedings 43rd Stanford Geothermal Workshop. Stanford, California; 2018.

Sammis CG, Ashby MF. The failure of brittle porous solids under compressive stress states. Acta Metall. 1986;34(3):511–26. https://doi.org/10.1016/0001-6160(86)90087-8.

Schellschmidt R, Sanner B, Pester S, Schulz R. Geothermal energy use in Germany. In: Proceedings World Geothermal Congress 2010, Bali, Indonesia, 25–29 April 2010; 2010.

Schön J. Physical properties of rocks: fundamentals and principles of petrophysics. Amsterdam, Netherlands: Elsevier; 2015.

Seithel R, Gaucher E, Mueller B, Steiner U, Kohl T. Probability of fault reactivation in the Bavarian Molasse Basin. Geothermics. 2019;82:81–90. https://doi.org/10.1016/j.geothermics.2019.06.004.

Selvadurai APS, Głowacki A. Permeability hysterisis of limestone during isotropic compression. Ground Water. 2008;46(1):113–9. https://doi.org/10.1111/j.1745-6584.2007.00390.x.

Settari A, Al-Ruwaili K, Sen V. Upscaling of geomechanics in heterogeneous compacting reservoirs. In: SPE reservoir simulation symposium. Society of Petroleum Engineers; 2013. https://doi.org/10.2118/163641-MS.

Shi L, Zeng Z, Fang Z, Li X. Investigation of the effect of confining pressure on the mechanics-permeability behavior of mudstone under triaxial compression. Geofluids. 2019;2019:1–14. https://doi.org/10.1155/2019/1796380.

Sibley DF, Gregg J. Classification of dolomite rock textures. J Sediment Petrol. 1987;57:967–75.

Sibley DF, Gregg JM, Brown RG, Laudon PR. Dolomite crystal size distribution. In: Rezak R, Lavoie DL, editors. Carbonate microfabrics. New York: Springer; 1993. pp. 195–204. https://doi.org/10.1007/978-1-4684-9421-1_15.

Siratovich PA, Heap MJ, Villenueve MC, Cole JW, Reuschlé T. Physical property relationships of the Rotokawa Andesite, a significant geothermal reservoir rock in the Taupo Volcanic Zone, New Zealand. Geotherm Energy. 2014;2(1):313. https://doi.org/10.1186/s40517-014-0010-4.

Smordinov M, Motovilov EA, Volkov V. Determination of correlation relationships between strength and some physical characteristics of rocks. In: Proc. 2nd Congr. ISRM, Belgrade. 1970(2):35–7.

Steiner U, Savvatis A, Böhm F, Schubert A. Explorationsstrategie tiefer geothermischer Ressourcen am Beispiel des süddeutschen Oberjuras (Malm). 2014:429–61. https://doi.org/10.1007/978-3-642-54511-5_13.

Teklu TW, Li X, Zhou Z, Abass H. Experimental investigation on permeability and porosity hysteresis of tight formations. SPE J. 2018;23(03):672–90. https://doi.org/10.2118/180226-PA.

Terzaghi K. Die Berechnung der Durchlassigkeitsziffer des Tones aus dem Verlauf der hydrodynamischen Spannungserscheinungen. Sitzungsberichte der Akadamie der Wissenchaften in Wien, Mathematisch-Naturwissenschaftliche Klasse, Abteihing, IIa. 1923(132):105–24.

Ulusay R. The ISRM suggested methods for rock characterization, testing and monitoring: 2007–2014. Cham: Springer; 2015.

Walder J, Nur A. Porosity reduction and crustal pore pressure development. J Geophys Res. 1984;89(B13):11539–48. https://doi.org/10.1029/JB089iB13p11539.

Walsh JB. Effect of pore pressure and confining pressure on fracture permeability. Int J Rock Mech Min Sci Geomech Abstracts. 1981;18(5):429–35. https://doi.org/10.1016/0148-9062(81)90006-1.

Wang G, Li P, Hao F, Zou H, Yu X (2015) Dolomitization process and its implications for porosity development in dolostones: A case study from the Lower Triassic Feixianguan Formation, Jiannan area, Eastern Sichuan Basin. China. J Petrol Sci Eng. 131:184–99. https://doi.org/10.1016/j.petrol.2015.04.011

Wang Y, Meng F, Wang X, Baud P, Wong T. Effective stress law for the permeability and deformation of four porous limestones. J Geophys Res Solid Earth. 2018;123(6):4707–29. https://doi.org/10.1029/2018JB015539.

Washburn EW. The dynamics of capillary flow. Phys Rev. 1921;17(3):273–83. https://doi.org/10.1103/PhysRev.17.273.

Webb PA. An introduction to the physical characterization of materials by mercury intrusion porosimetry with emphasis on reduction and presentation of experimental data. 2001. https://www.micromeritics.com/pdf/app_articles/mercury_paper.pdf. Accessed 20 Aug 2020.

Weber J, Moeck I. Deep geothermal energy: principles and application possibilities in Germany. 2017th edn. Hannover, Germany: Leibniz Institute for Applied Geophysics; 2017.

Wu Y, Tahmasebi P, Lin C, Zahid MA, Dong C, Golab AN, Ren L. A comprehensive study on geometric, topological and fractal characterizations of pore systems in low-permeability reservoirs based on SEM, MICP, NMR, and X-ray CT experiments. Mar Pet Geol. 2019;103:12–28. https://doi.org/10.1016/j.marpetgeo.2019.02.003.

Wyllie M, Gregory A, Gardner L. Elastic wave velocities in heterogeneous and porous media. Geophysics. 1965;21(1):41–70.

Xu C, Lin C, Kang Y, You L. An experimental study on porosity and permeability stress-sensitive behavior of sandstone under hydrostatic compression: characteristics, mechanisms and controlling factors. Rock Mech Rock Eng. 2018;51(8):2321–38. https://doi.org/10.1007/s00603-018-1481-6.

Yale DP. Network modeling of flow, storage and deformation in porous rocks. [Dissertation]. Stanford, California: Standford University; 1984.

Zhu W, Baud P, Wong T. Micromechanics of cataclastic pore collapse in limestone. J Geophys Res. 2010. https://doi.org/10.1029/2009JB006610.

Zimmerman RW, Somerton WH, King MS. Compressibility of porous rocks. J Geophys Res. 1986;91(B12):12765–77. https://doi.org/10.1029/JB091iB12p12765.

Zoback MD, Byerlee JD. The effect of microcrack dilatancy on the permeability of westerly granite. J Geophys Res. 1975;80(5):752–5. https://doi.org/10.1029/JB080i005p00752.

Publisher's Note